Title
A NEW LASER COOLING METHOD FOR LITHIUM ATOM INTERFEROMETRY

Author
Kim, Geena

Publication Date
2014

Peer reviewed|Thesis/dissertation

A NEW LASER COOLING METHOD FOR LITHIUM ATOM INTERFEROMETRY

by

Geena Kim

A dissertation submitted in partial satisfaction of the
requirements for the degree of
Doctor of Philosophy

in

Physics

in the

Graduate Division

of the

University of California, Berkeley

Committee in charge:

Professor Holger Müller, Chair
Professor Dmitry Budker
Professor Eli Yablonovitch

Fall 2014

A NEW LASER COOLING METHOD FOR LITHIUM ATOM INTERFEROMETRY

Abstract

A NEW LASER COOLING METHOD FOR LITHIUM ATOM INTERFEROMETRY

by

Geena Kim

Doctor of Philosophy in Physics

University of California, Berkeley

Professor Holger Müller, Chair

An atom interferometer offers means to measure physical constants and physical quantities with a high precision, with relatively low cost and convenience as a table-top experiment. A precision measurement of a gravitational acceleration can test fundamental physics concepts such as Einstein equivalence principle (EEP). We identified that the two lithium isotopes (^{7}Li and ^{6}Li) have an advantage for the test of EEP, according to the standard model extension (SME). We aim to build the world's first lithium atom interferometer and test the Einstein equivalence principle.

We demonstrate a new laser cooling method suitable for a lithium atom interferometer. Although lithium is often used in ultra-cold atom experiments for its interesting physical properties and measurement feasibility, it is more difficult to laser cool lithium than other alkali atoms due to its unresolved hyperfine states, light mass (large recoil velocity) and high temperature from the oven. Typically, standard laser cooling techniques such as Zeeman slowers and magneto-optical traps are used to cool lithium atoms to about 1 mK, and the evaporative cooling method is used to cool lithium atoms to a few μK for Bose-Einstein condensate (BEC) experiments. However, for the atom interferometry purpose, the evaporative cooling method is not ideal for several reasons: First, its cooling efficiency is so low (0.01 % or less) that typically only $10^4 - 10^5$ atoms are left after cooling when one begins with 10^9 atoms. More atoms in an atom interferometer are needed to have a better signal to noise ratio. Second, an evaporative cooling is used to make a BEC, but we do not need a BEC to make an atom interferometer. In an atom interferometer, a high density of atoms as in a BEC should be avoided since it causes a phase shift due to atom interactions. Third, a setup for an evaporative cooling requires intricate RF generating coils or a high power laser.

With a simple optical lattice and a moderate laser power (100 mW), we achieved a sub-Doppler cooling of lithium by a new laser cooling method despite the fact that lithium has un-resolved hyperfine structure. We identified that the Sisyphus cooling and the adiabatic cooling mechanisms cooperate and give both lower temperature and higher cooling efficiency

than the result that can be achieved by each alone. We cooled ^{7}Li atoms to $\sim$ 50 μK (about 8 times the recoil temperature) in a one dimensional lattice with cooling efficiency of 50%. In three dimensions the cooling temperature was limited to 90 μK due to instability of our 3D lattice, however the same principle applies and potentially a lower temperature can be achieved in 3D as well.

To my family

Contents

List of Figures

List of Tables

Acknowledgments

I should acknowledge that doing a Ph.D. was harder than I had imagined and being a Ph.D. feels better than I had imagined. Probably many will agree that it is hard not just because we have to solve difficult problems and overcome obstacles, but especially because we have to fight with our fear and an emotional drag from self-doubt and uncertainties. I would have not accomplished my Ph.D. without the guidance and support from my advisor Holger Mueller, who has been always cheerful and insightful.

I was lucky to join the Mueller group when he just started the lab. It was a really exciting and rewarding experience to be the first runner of a project which gave me a great opportunity to plan and build from the start. Although at times it was difficult to cope with the long debugging time and be patient to reach the frontier, I was able to overcome those and contribute to a new discovery. It is worth to note that those achievements were possible not only due to the personal effort but also thanks to the help and support from my colleagues and my adviser. I would like to thank Paul Hamilton who has worked for the longest time with me, for his help and contributions on my project. I would like to thank Biswaroop Mukherjee, Daniel Tiarks, Dennis Schlippert, and Marcus Ossiander who helped the project for some period, for their help and contributions to the project. I also thank to Michael Hohensee and Brian Estey for helpful discussions. It was great to be with other nice lab mates- Shau-Yu Lan, Pei-Chen Kuan, Michelle Xu, Justin Brown, Francisco Monsalve, and Erin Sohr who had good humor and scientific insights and gave me good help and support. It was also my great pleasure to work with many talented students- Kayleigh Cassella, Matt Jaffe, Chenghui Yu and Trinity Josh.

I thank my adviser and other committee member professors Dima Budker and Eli Yablonovitch for their feedback and encouragement. I thank Holger and other faculty members especially Prof. Marjorie Shapiro, Mike Dewesee, and Ori Ganor for mentoring my graduate life. Finally I would like to thank my parents, Shai, and my friends who gave me a great emotional support.

Chapter 1

Introduction

1.1 Motivation

1.1.1 The Einstein Equivalence Principle

Although the gravitational force was discovered earliest among the four fundamental forces, gravity is least understood. Gravity has not been successfully unified with other forces yet; while other forces can be described in quantum mechanics, theory of gravity (general relativity) is not compatible with quantum mechanics in a strong gravity. Also exchange particles for non-gravitational interactions (photon for electromagnetism, W and Z-bosons for weak interaction, pions and gluons for strong interaction) have been discovered while the exchange particle for gravity (graviton) has not been discovered yet.

The current standard theory of gravity-Einstein's general relativity- is a generalization of special relativity and Newtonian gravity. It has an important underlying assumption called the Einstein equivalence principle (EEP), and describes gravity as a geometric property of spacetime. The EEP states that the acceleration is indistinguishable from the gravitational field. In detail, EEP is usually divide into three statements-

· Universality of free fall (UFF)
· Local position invariance (LPI)
· Local Lorentz invariance (LLI)

Universality free fall means that all objects fall with same acceleration in a local gravitational field regardless of their mass or composition. Local position invariance (LPI) means that the outcome of any non-gravitational experiment is independent of where and when in the universe it is performed, which implies universality of the gravitational redshift (UGR) and time invariance in physical constants such as fine structure constant α. Local Lorentz invariance (LLI) means that the outcome of any local non-gravitational experiment is independent of the velocity of the freely-falling reference frame in which it is performed. The term "local" means that the experiment is performed within the small spacetime region that

the experimental apparatus cannot detect tidal effect or perturbation of gravitational field.

Testing EEP plays an important role for searching new theories. There have been several approaches for the new theory of gravity that can unify gravity with quantum mechanics (quantum gravity). Quantum gravity models violate some of basic principles underlying general relativity or current quantum theory; as a result, whole or part of EEP are violated[1] [46]. Similarly, not only Quantum Gravity theories, but other theories beyond Standard Model also predict violation of EEP. Therefore test of EEP is very important for searching and validating those new theories as well as testing accuracy of general relativity.

Among the three components of EEP, the universality of free fall (UFF) takes the core and is also known as weak equivalence principle (WEP). Therefore it suggests that testing UFF (or WEP) is of primary importance to test EEP in regards to gravity experiments.

1.1.2 Test of Universality of Free Fall

Universality of free fall, as the name suggests, states that all massive objects fall with the same acceleration in a gravitational field regardless of their properties. This concept seems to be also implied in Newtonian mechanics in that the proportionality of any force to the resulting acceleration is the mass of the object, and the gravitational force is also proportional to the mass.

$$\begin{aligned} F &= ma \\ F_g &= mg \end{aligned} \tag{1.1}$$

In fact there is no reason why inertial mass should be the same as gravitational mass (weight), however Einstein took the opposite reasoning for the assumption- there is no reason why they should be different. In summary, UFF can be stated in three ways.

· Gravitational field is the same as acceleration ($g = a$)
· Gravitational mass is the same as inertial mass ($m_g = m_I$)
· With the same initial conditions, all object fall at the same rate in gravitational field regardless of their mass, internal structure or composition.

The measure of UFF violation can be defined as a dimensionless parameter η called Eötvös parameter

$$\eta \equiv \frac{\Delta a}{\bar{a}} \tag{1.2}$$

where Δa is a difference in gravitational acceleration of two free-falling objects, and $\bar{a}$ is the average acceleration of the two objects.

[1]For example, Loop quantum gravity theory can predict violations of Lorentz invariance (LI) and UFF, String theory can violate LI, LPI, and UFF (all EEP conditions), and non-commutative geometry theory can violate LI and UFF [46]

The first accurate Eötvös parameter measurement ($\eta = 10^{-8} \sim 10^{-9}$) was achieved in 20th century by Eötvös himself using a torsion balance and taking the Earth as a source mass [53]. Later the torsion balance test achieved better precision ($\eta = 10^{-11} \sim 10^{-12}$) by using the Sun's gravity instead of the Earth gravity [53, 54]. Current best bound on Eötvös ratio ($\eta < 1.8 \times 10^{-13}$) has been set by a torsion balance with beryllium and titanium test bodies with the same mass on a pendulum hanging on a turn table [55].

Similar precision ($\eta < 1.4 \times 10^{-13}$) has been achieved from Lunar Laser Ranging (LLR) method [56]. LLR measures differential acceleration of the Moon and the Earth in the Sun's gravitational field, by measuring the distance between the Moon and the Earth.

So far the best bound on Eötvös parameter ($\eta \sim 10^{-13}$) was obtained by torsion balance and LLR methods using macroscopic objects. As a microscopic and quantum object, an atom is an interesting candidate for a test of UFF. Quantum gravity models suggest space-time fluctuation in quantum scale- therefore violation of UFF in microscopic object may be different from that of macroscopic object [47]. Also, a UFF test using atoms is usually a Galileo-type experiment (dropping objects in the Earth gravity $g = 9.8\,\mathrm{m/s^2}$) which in principle is more sensitive to the differential acceleration Δg than in the Sun's gravitational field on Earth $g_s = 0.006\mathrm{m/s^2}$ (the current best measurement by torsion balance and LLR is based on g_s). Furthermore, atoms provide rich high-precision measurement methods such as interferometry and clocks.

An accurate measurement of the gravitational acceleration of atoms can be done by using atom interferometry (AI). An atom interferometer uses the wave property of an atom. In an atom interferometer, an atom matterwave is the coherent wave that can interfere with itself, and light pulses act as beam splitters and mirrors for the atom matterwave. By the light beam splitters, atoms are split into two different momentum states and move along the two separated paths. After the separation time, these two paths overlap through another beam splitter to form a interference fringe. From the interference fringe, a phase difference between the two paths can be measured. From the phase difference, depending on the atom interferometer geometry, gravity acceleration, gravity gradient, and recoil frequency (a frequency equivalent quantity to the atom's kinetic energy by a photon recoil)[2] can be measured.

Although its Eötvös parameter bound has not reached yet to the current best limit (10^{-13}), atom interferometry has been used to test UFF. A comparison between uncertainty of local gravity measurement by cesium fountain atom interferometer (3×10^{-9}) and by conventional laser gravimeter FG5 (1×10^{-9}) confirmed UFF on 7×10^{-9} level [74]. As the first microscopic-only test of UFF, a dual atom interferometer using ^{85}Rb and ^{87}Rb demonstrated 10^{-7} precision by alternating operation of each isotope AI [75], and later by a simultaneous

[2]The kind of measurable quantities depends on the AI geometry/configuration. For example recoil frequency can be measured in Ramsey-Bordè configuration but not in Mach-Zehnder configuration.

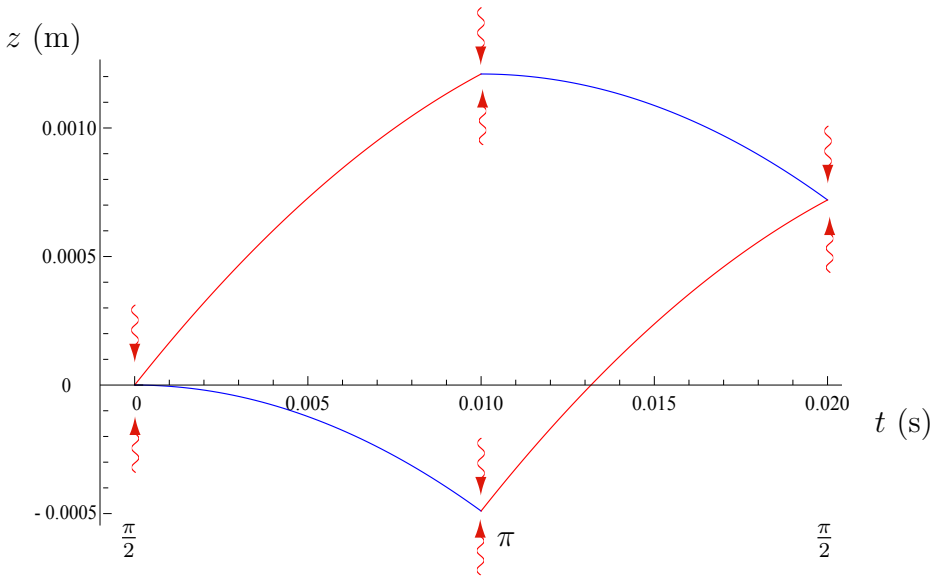

Figure 1.1: Mach-Zehnder atom interferometer. ^{7}Li parameters with the momentum transfer $p = 2\hbar k$ are used in the calculation. Red arrows are the $\pi/2$ and π pulses corresponding to light beam splitter and mirror. Red and blue trajectories show that atoms are in the different states in the case of Raman-beam. For Bragg beam splitter the atom's internal state does not change.

dual atom interferometer using two rubidium isotopes [76].

1.1.3 Potential of Atom Interferometry for the test of UFF

For acceleration measurement, Mach-Zehnder type atom interferometers (Fig. 1.1) are used, and the phase difference between two arms is derived as

$$\Delta\phi = k_{\text{eff}} T^2 a = (2nk) T^2 a, \tag{1.3}$$

where T is the free evolution time (the time between adjacent pulses), k is the momentum of a single photon, n is the diffraction order from the light pulse grating, and k_{eff} is the effective wavenumber. The effective momentum transfer ($\hbar k_{\text{eff}}$) by the beam splitter is an integer multiple of $2\hbar k$. Sensitivity of a measurement to acceleration is proportional to the ratio of acceleration to the phase difference in an atom interferometer. The shot-noise-limited sensitivity of an acceleration measurement by an AI for a single cycle is

$$\sigma_{a,1} = \frac{a}{\Delta\phi} \frac{1}{\sqrt{N}}, \tag{1.4}$$

where N is the number of atoms contributed in the interference. The smaller the value of σ, the better the sensitivity. When the measurement is integrated which means many cycles are taken into account, the shot-noise-limited sensitivity on acceleration is

$$\sigma_a = \frac{a}{\Delta\phi}\frac{1}{\sqrt{N}}\sqrt{\frac{T_\mathrm{c}}{T_\mathrm{int}}}, \tag{1.5}$$

where T_c is the cycle time and T_int is the integration time. Effectively $\frac{T_\mathrm{int}}{T_\mathrm{c}}$ represents the number of shots during the integration. When two species or isotopes are used for simultaneous acceleration measurement, sensitivity on the differential gravitational acceleration is $\sigma_{\Delta g} = \sqrt{2}\sigma_g$, and the resulting Eötvös parameter becomes

$$\eta_{A,B} = \frac{\sigma_{\Delta g}}{g} = \frac{\sqrt{2}}{\Delta\phi}\frac{1}{\sqrt{N}}\sqrt{\frac{T_\mathrm{c}}{T_\mathrm{int}}}. \tag{1.6}$$

For example, a simple Mach-Zehnder(MZ) AI with Raman beam splitter ($n = 1$) with separation time $T = 0.3$ s (z=0.5 m launch height of the fountain) and 10^6 Rb atoms (each isotope) contributing to the fringe, integrated for 1 day with 2 s of cycle time gives Eötvös parameter on the order of 10^{-12}. Atom numbers and integration time are square-rooted therefore increasing those values is not as effective as increasing phase difference. Also the potential room to increase for phase difference is bigger than others such as atom number and integration time. Phase difference, as shown in Eq. 1.3, is proportional to the diffraction order n and the free evolution time squared T^2. Recent advances in beam splitter technique achieved 24 $\hbar k$ large momentum transfer (LMT) in MZ and Ramsey-Bordé (RB) configuration using Bragg beam [77]. While increasing diffraction order in an AI using Bragg beam splitters only can be painfully difficult because of the power requirement, it has been shown that the enclosed area (thus the diffraction order) in a MZ atom interferometer is scalable with combination of Bragg beam and Bloch oscillation; as a result, large momentum transfer as much as 100 $\hbar k$ was projected [78], and 102 $\hbar k$ beam splitter has been demonstrated by using sequential Bragg beams [79]. In regards to the free evolution time between pulses T, there has been effort to increase T in fountain type atom interferometer. However, since the spatial separation (the hight) required increases quadratically as the time increases, it makes difficult to avoid increased systematic effect due to atom cloud spread. While 10 m fountain which allows more than 1 s free evolution time has been developed [80, 81], a different approach than fountain type interferometer such as lattice AI [82] or double-diamond (or multi-diamond) AI [83] may achieve longer T without increasing the AI size too much. Finally, to perform ideally as shot-noise-limited, an AI needs to eliminate its various systematic effects. Common-mode-rejection by symmetric MZ interferometer configuration can get rid of systematic effects from common-mode. Gouy phase also can decrease the visibility of fringe signal and add uncertainty of the phase difference. The Gouy effect can be minimized in the cavity-based atom interferometer [84].

Model/scenario	To support/search for	η	Ref.
· Dilaton scenario	Graviton	10^{-13}	[48]
· Holographic noise scenario	Spatetime fluctuation	$10^{-12} \sim 10^{-17}$	[49]
· Quintessence model	Dark energy	10^{-14}	[50]
· Berkenstein theory variation	Time varying e, dark matter	10^{-13}	[51]
· 4D field theory	Time varying α, 5th force, quintessence	10^{-14}	[52]

Table 1.1: Theoretical estimation for Eötvös parameter

1.1.4 Future of the UFF test

In Table 1.1, various models and scenarios in quantum gravity theories, some field theories and cosmology theories estimates the violation of UFF between $10^{-12} \sim 10^{-14}$ level. Therefore achieving $\eta \leq 10^{-14}$ is meaningful and can validate those theories and models.

Currently various proposed experiments are targeting Eötvös parameter in $\eta = 10^{-9} \sim 10^{-18}$ range. Examples of atom interferometer based UFF test are: A ground based ^{87}Rb−^{39}K AI at LUH Germany targets 10^{-9} level [57, 58]. A 8.8 m -long-fountain AI tower at Stanford uses ^{87}Rb−^{85}Rb and expects 10^{-14} level [59]. ICE (Interférométrie Cohérente pour l'Espace) project propose a ^{87}Rb−^{39}K AI in aircraft and targets 10^{-11} level [60]. QUANTUS (Quantum gases in microgravity) project proposes to use ^{87}Rb−^{40}K on-chip-BEC AI in Bremen ZARM drop tower (110 m) and on a sounding rocket and targets $10^{-10} \sim 10^{-11}$ level [61]. STE-QUEST (Space-Time Explorer and Quantum Equivalence Principle Space Test) project proposes to use ^{87}Rb−^{85}Rb AI on a satellite orbiting around the Earth, and targets 10^{-15} level [62], and NASA also launched its atom interferometry project in space station QTEST(Quantum Test of Equivalence and Space Time) which aims $\eta \sim 10^{-15}$. On the other hand, there are also proposed UFF tests using macroscopic objects. MICROSCOPE (Micro-Satellite á traînée Compensée pour l'Observation du Principe d'Equivalence) project proposes to measure acceleration of macroscopic masses using electrostatic sensors in a satellite orbiting the Earth [63, 64], and is targeting 10^{-15} level. STEP project has similar scheme (measuring acceleration of masses in satellite) as MICROSCOPE except uses SQUID sensors to measure acceleration and targets 10^{-18} level [65, 66]. GG (Galileo Galilei) project, which uses two 10 kg test masses on a vertically rotating mechanical suspension, proposes 10^{-17} level in space [67].

1.2 Our Goal

As mentioned earlier in section 1.1.3, atom interferometry is a great tool for precise measurement and testing the universality of free fall. In a UFF test with atom interferometer, two atomic species are used as test masses and their accelerations are measured. Not only for technical feasibility, but also for a scientific reason we choose two lithium isotopes ^{7}Li

and ^{6}Li as test masses. We use the minimal Standard Model Extension (mSME) model to find out a pair of atomic species with better sensitivity to the violation of UFF [89]. In the mSME framework, additional terms that violate Lorentz and CPT invariance (meaning also violating EEP) are added to standard model formulation. Using the model, the isotropic EEP violation terms up to $O(c^{-2})$ are described with six coefficients $\alpha(\bar{a}^w_{\rm eff})_0$ and $(\bar{c}^w)_{00}$, where superscript w can be n, p, or e representing contribution from neutron, proton or electron fields. For a test body consisting of numbers of protons, electrons and neutrons, the composite SME coefficients are linear combination of SME coefficients for those elementary particles.

$$\begin{aligned}(\bar{a}^T_{\rm eff})_0 &= \sum_w N^w (\bar{a}^w_{\rm eff})_0 \\ (\bar{c}^T)_{00} &= \sum_w \frac{N^w m^w}{m^T} (\bar{c}^w)_{00},\end{aligned} \tag{1.7}$$

where N^w is the number of elementary particle w. When such a test body with mass m^T falls in a gravitational field g, the acceleration g^T of the test mass under EEP violation is described as

$$\begin{aligned}g^T &= g(1+\beta^T), \\ \beta^T &\equiv \frac{2\alpha}{m^T}(\bar{a}^T_{\rm eff})_0 - \frac{2}{3}(\bar{c}^T)_{00}.\end{aligned} \tag{1.8}$$

An EEP-violating observable is the difference of the two βs of the two test masses A and B ($\beta^{\rm A} - \beta^{\rm B}$). The resulting expression is a linear combination of basis β^{e+p+n}, β^{e+p-n}, and their anti-matter counterpart $\beta^{\bar{e}+\bar{p}+\bar{n}}$ and $\beta^{\bar{e}+\bar{p}-\bar{n}}$, with weights proportional to differences in atoms' effective neutron excess, effective mass defect, and kinetic energy of nucleons (the full calculation and numbers can be found in [90]). Figure 1.2 shows a plot of relative sensitivity to EEP-violation for stable isotopes of atoms. Highlighted points depict atomic species that can be used for EEP tests. Roughly speaking, the farther the distance between the two points in the chart, the more sensitive to the EEP-violation. As shown in the plot, ^{7}Li and ^{6}Li are more distant compared to other atoms used in prior experiments (e.g., Ti-Be, and ^{85}Rb-^{87}Rb), thus the ^{7}Li-^{6}Li pair can be a good candidate for an EEP test.

Moreover, lithium atoms are laser-coolable, make it feasible to build an atom interferometer. An atom interferometer using ultra-cold lithium atoms has not been demonstrated to date, which makes it a meaningful goal to demonstrate the first lithium atom interferometer. Nevertheless ^{7}Li and ^{6}Li choice has a good property in terms of sensitivity to the EEP-violation observable and feasibility with building an atom interferometer, there are technical difficulties to overcome. Lithium atoms are harder to cool with a laser due to their light masses (therefore higher recoil temperatures compared to other alkali atomic species) and un-resolved hyperfine states of the D2 transition. For the same reason it is harder to build an atom interferometer with lithium atoms than other alkali atoms- especially for the fountain-type atom interferometry due to fast cloud expansion. This technical difficulty motivates us to design a novel atom interferometer without a fountain (launch and free-fall) method.

Finally, our goal includes developing a new cooling method for lithium. Although lithium atoms can be cooled to sub-μK temperature by evaporative cooling, which slowly reduces the trap potential such that the hot atoms in the new thermal equilibrium take the heat away as they leave the trap, typically only less than ten thousands atoms are left after evaporative cooling a hundred millions of lithium atoms. For an atom interferometer, increased number of atoms is advantageous for better signal-to-noise. To avoid significant atom loss from evaporative cooling, a new laser cooling method that can cool lithium atoms to a sufficiently low temperature for an interferometry purpose (e.g. 10's - 100 μK) is needed. The cooling of lithium atoms by laser molasses or magneto-optical trap (MOT) alone had been considered to be not possible to get below the Doppler temperature (142 μK for ^{7}Li), due to a difficulty to get Sisyphus cooling to work because of un-resolved hyperfine states of D2 transition. Our disruptive discovery on a new laser cooling result using an optical lattice shows that a cooling temperature about 40 - 100 μK can be reached in one-dimensional cooling for ^{7}Li atoms with up to 50% cooling efficiency.

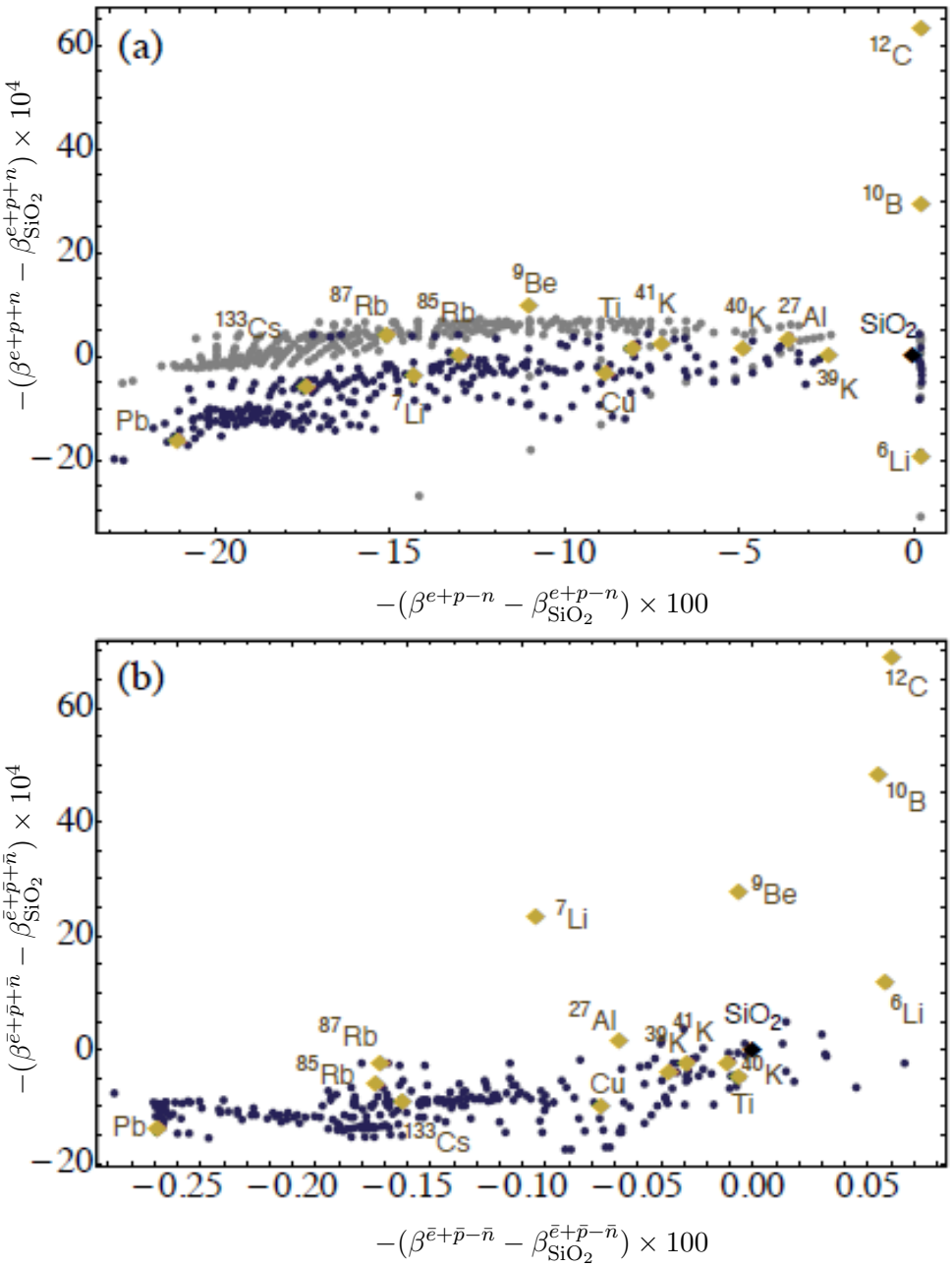

Figure 1.2: Relative sensitivity to EEP-violation in matter sector (a) and anti-matter sector (b), with respect to SiO_2. The graph is adopted from [90] with a kind permission from M. Hohensee.

Chapter 2

Properties of lithium

Understanding the properties of lithium helps to build experimental apparatus and to perform our experiment. In this section, the physical, nuclear and optical properties, and the energy level structure of ^{7}Li and ^{6}Li are discussed.

2.1 General properties of lithium

A lithium atom consists of three protons, three electrons and a number of neutrons. The number of neutrons vary depending on lithium isotopes. Lithium has two stable isotopes ^{7}Li and ^{6}Li in the nature. Other isotopes such as ^{8}Li and ^{9}Li have life time shorter than 1 s. In the nature, ^{7}Li is the most abundant form (92.4 %), and the rest is ^{6}Li (7.6 %). A ^{7}Li atom has four neutrons, thus is a boson, and has a nuclear spin of 3/2. A ^{6}Li atom has three neutrons, forms a fermion, and has nuclear spin of 1. Both isotopes have unexpectedly low binding energy compared to other atomic species (Fig. 2.1).

A lithium atom has two electrons in the core electron shell ($n = 1$) and one electron in the outmost electron shell ($n = 2$), which classifies lithium as an alkali metal. Like other alkali

Property	Symbol	^{7}Li	^{6}Li	Ref
Atomic Number	Z	3	3	
Nucleons	Z+N	7	6	
Natural Abundance	η	92.4 %	7.6 %	[30]
Nuclear Lifetime	τ_n	stable	stable	[30]
Mass	m	7.016 004 amu	6.015 121 4 amu	[32],[31]
		1.165035×10^{-26} kg	9.988341×10^{-27} kg	
Nuclear Spin	I	3/2	1	

Table 2.1: General atomic properties of lithium

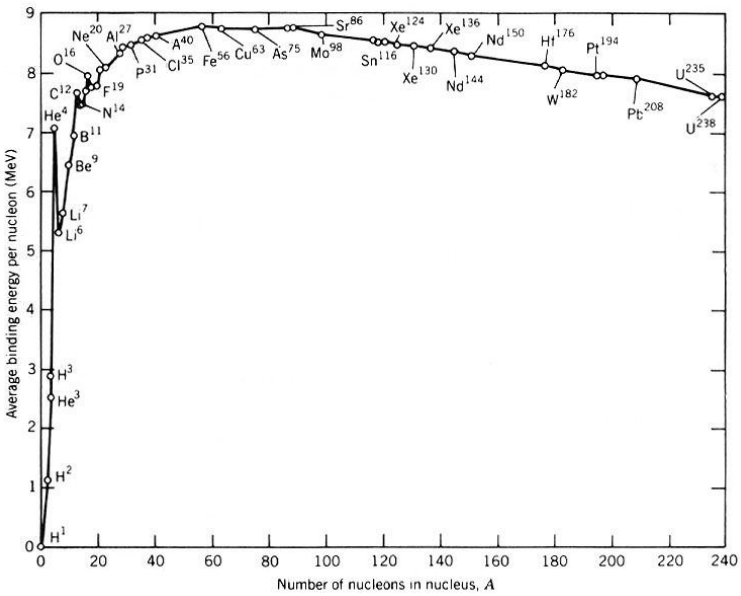

Figure 2.1: Binding energy of atoms. The image is taken from Wikimedia Commons which original data is from [44].

metal atoms, lithium forms a solid in room temperature, which color is shiny silver color in a pure form. As soon as lithium is exposed in an atmosphere, it reacts with moisture and nitrogen, and forms a dark colored layer of lithium hydroxide (LiOH) and lithium nitride (Li_3N) on the surface. Because of its reactivity in an atmosphere, usually it is packaged in either mineral oil or in an ampule. For the same reason, when building an experimental setup with lithium, it should be handled in an inert gas environment using glove box or glove bag with argon flush. For the safety, it is important to note that lithium reacts violently in an aqueous solution, yet it does not explode as other heavier alkali atoms do. When lithium is soaked with water or solutions which can produce water by secondary reaction (e.g., methanol) it reacts quickly to leave white powder of lithium hydride with bubbles and heat. The lithium hydroxide powder fume, which can be made easily during the lithium sample preparation, is hazardous and irritates skin, eyes and respiratory system thus careful treatment is needed.

Lithium is the lightest among alkali atoms[1] and among all metals. Lithium's density is as low as 0.534 $\mathrm{g\,cm^{-3}}$ and its melting point is about 180°C and boiling point is 1330°C, which results in a low vapor pressure. Vapor pressure of lithium is calculated using Antoine

[1]Hydrogen has only one electron, however is not considered as an alkali atom since many of physical properties of hydrogen are dissimilar to those of alkali metals- Alkali atoms are in a solid phase in a room temperature, has high reactivity with water and oxygen, has shiny silver color in a pure form and is soft. Both hydrogen and alkali atoms are group 1 elements. In terms of optical transition and energy level structure, hydrogen is similar to other alkali atoms.

Temperature (K)	A	B	C	Ref
298.14 - 1599.99	4.98831	7918.984	-9.52	[33]

Table 2.2: Lithium Antoine parameters

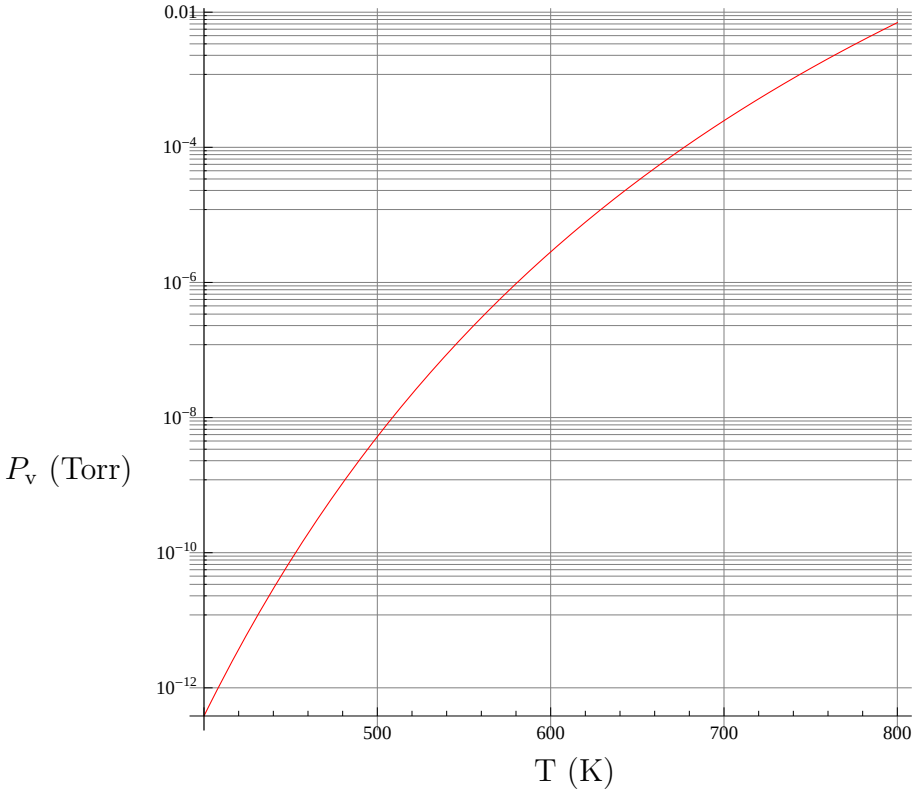

Figure 2.2: Vapor pressure of lithium

equation

$$\mathrm{Log}_{10}(P_\mathrm{v}) = A - \frac{B}{T+C}, \tag{2.1}$$

where P_v is the vapor pressure in bar, T is the temperature in K. A, B, and C are Antoine coefficients which include information about atmosphere pressure, heat of vaporization, and connection between Antoine equation and Clausius-Clapeyron equation respectively. Figure 2.2 shows the vapor pressure (Torr) of lithium as a function of temperature (K). At room temperature, the vapor pressure is very low for a cold atom experiment, therefore the lithium source has to be heated to about 400°C in order to get enough vapor pressure (about 0.1 mTorr).

2.2 Energy level structure of lithium

A lithium atom has a single valence electron and its electron configuration is $1s^2\,2s$ in the ground state and $1s^2\,2p$ in the first excited state. The energy level structure of a lithium atom resembles that of a hydrogen atom, but has different values of the energy shift due to interactions of spins and angular momentum of constituent particles. In this section, we focus on fine and hyperfine structures of lithium since we take advantage of those structures in our experiment.

2.2.1 Fine structure

Electron orbital L is an angular momentum quantity, and electron spin S is also an angular momentum quantity thus they can interact to give the total angular momentum J. A splitting of an energy level due to this electron spin-orbit interaction is called fine structure. The electron spin-orbit interaction Hamiltonian comes from the interaction between the electron's magnetic moment (spin) and the effective magnetic field from the electron's orbital motion

$$H = -\boldsymbol{\mu} \cdot \mathbf{B} \tag{2.2}$$

With a relativistic correction (Thomas precession), the resulting spin-orbit hamiltonian becomes

$$H_{SO} = (g_s - 1)\,\frac{\hbar^2}{2{m_e}^2c^2}\left(\frac{1}{r}\frac{\partial V_{\text{eff}}(r)}{\partial r}\right)\mathbf{S}\cdot\mathbf{L}, \tag{2.3}$$

where $V_{\text{eff}}(r)$ is the potential due to effective charge by nucleus and inner shell electrons. Total angular momentum by electron is $\mathbf{J} = \mathbf{L} + \mathbf{S}$ therefore the operator $\mathbf{S}\cdot\mathbf{L}$ can be replaced by $\frac{1}{2}(\mathbf{J}^2 - \mathbf{L}^2 - \mathbf{S}^2)$, where the operators $\mathbf{L}^2$, $\mathbf{S}^2$, $\mathbf{J}^2$, along with $\mathbf{J}_z$ form a complete set of operators that commute each other and the corresponding quantum numbers L, S, J, and M_J become good quantum numbers. Quantum number J takes values

$$|L - S| \le J \le L + S. \tag{2.4}$$

An alkali atom's excited state (P orbital) has angular momentum of $L = 1$ and electron spin is $S = 1/2$, therefore it has two fine structure states $P_{1/2}$ and $P_{3/2}$ corresponding to total orbital angular momentum of $J = 1/2$ and $J = 3/2$. The optical transitions from the ground state $S_{1/2}$ to the excited states $P_{1/2}$ and $P_{3/2}$ are called D_1 and D_2 transition, which the letter 'D' is from the sodium 'D'oublet in Fraunhofer lines. ^{7}Li has D_1 transition at λ = 670.976 nm, and D_2 transition at λ = 670.961 nm, while ^{6}Li has D_1 transition at λ = 670.992 nm, and D_2 transition at λ = 670.977 nm.

2.2.2 Hyperfine structure

Each D-line has substructures due to hyperfine interaction. Hyperfine structure comes from the interaction between the nucleus and the effective magnetic field from atomic elec-

trons. The Hamiltonian includes the nuclear magnetic dipole interaction and nuclear electric quadrupole interaction. While the first term contributes on $S_{1/2}$, $P_{1/2}$ and $P_{3/2}$ energy levels, the second term contributes only on $P_{3/2}$ state. Nuclear magnetic octupole also contributes on $P_{3/2}$ state, however is much smaller (in kHz scale) than nuclear electric dipole moment interaction (in MHz scale) therefore it is omitted in Eq. 2.5.

$$H_{HF} = \boldsymbol{\mu}_I \cdot \mathbf{B}_e + \frac{1}{6} e\, \mathbf{Q}_{ij} \cdot \boldsymbol{\nabla}^2_{ij} \boldsymbol{\Phi} \tag{2.5}$$

Introducing a new quantum number F and the total atomic angular momentum operator $\mathbf{F} = \mathbf{I} + \mathbf{J}$, the energy shift by the hyperfine interaction becomes

$$\Delta E_{HF} = \frac{1}{2} hAK + hB \frac{\frac{3}{2}K(K+1) - 2I(I+1)J(J+1)}{2I(2I-1)2J(2J-1)}, \tag{2.6}$$

where $K = 2\langle \mathbf{I} \cdot \mathbf{J} \rangle = F(F+1) - I(I+1) - J(J+1)$, A is the magnetic dipole constant and B is the electric quadrupole constant [35].

$$\begin{aligned} A &= -\frac{{\mu_B}^2}{h} \frac{\mu_0}{4\pi} \frac{2L(L+1)}{J(J+1)} g_I \left\langle r^{-3} \right\rangle_{nL} \\ B &= \frac{Q}{h} \frac{e^2}{4\pi\epsilon_0} \frac{2J-1}{2J+2} \left\langle r^{-3} \right\rangle_{nL} \end{aligned}$$

Experimental measurement values for constants A and B for S and P states of ^{7}Li and ^{6}Li are listed in Table 2.3. The resulting energy level diagrams for ^{7}Li and ^{6}Li are shown in Figure 2.3. Both ^{7}Li and ^{6}Li have unresolved hyperfine splitting in $P_{3/2}$ states since the splitting is comparable to the line width 5.9 MHz. Also ^{7}Li and ^{6}Li $P_{3/2}$ states are inverted (i.e., energy of lower F state is higher) due to negative values of magnetic dipole and electric quadruploe hyperfine constants for their $P_{3/2}$ states. ^{7}Li D1 transition and ^{6}Li D2 transition are close to each other and the two frequencies differ by only 500 MHz which is smaller than the Doppler broadening of thermal lithium ($\sim$ 2 GHz at $T = 400^{\circ}$C), thus it gives an unresolved signal in the absorption spectrum of thermal lithium.

Property	Symbol	^{7}Li	^{6}Li
$2S_{1/2}$ Magnetic Dipole Constant	$A_{2S_{1/2}}$	401.75 MHZ [36]	152.14 MHz [36]
$2P_{1/2}$ Magnetic Dipole Constant	$A_{2P_{1/2}}$	45.914 MHZ [38]	17.375 MHz [39]
$2P_{3/2}$ Magnetic Dipole Constant	$A_{2P_{3/2}}$	-3.055 MHZ [38]	-1.155 MHz [39]
$2P_{1/2}$ Electric Quadrupole Constant	$B_{2P_{3/2}}$	-0.222 MHZ [38]	-0.010 MHz [39]

Table 2.3: Hyperfine constants for $2S$ and $2P$ levels of lithium.

Property	Symbol	Value	Ref
Total nuclear g-factor	g_I (^{7}Li)	-0.001 182 213	[40] [35]
	g_I (^{6}Li)	-0.000 447 654	[40] [35]
Total electronic g-factor	g_J ($2S_{1/2}$)	2.002301	[35]
	g_J ($2P_{1/2}$)	0.6668	[35]
	g_J ($2P_{3/2}$)	1.335	[35]

Table 2.4: Gyromagnetic ratios of lithium

Transition	λ (nm)	$\Delta\nu$ (GHz)
^{7}Li D_2, $2S_{1/2} - 2P_{3/2}$	670.961	20.590
^{7}Li D_1, $2S_{1/2} - 2P_{1/2}$	670.976	10.534
^{6}Li D_2, $2S_{1/2} - 2P_{3/2}$	670.977	10.050
^{6}Li D_1, $2S_{1/2} - 2P_{1/2}$	670.992	0

Table 2.5: Lithium transitions [41]

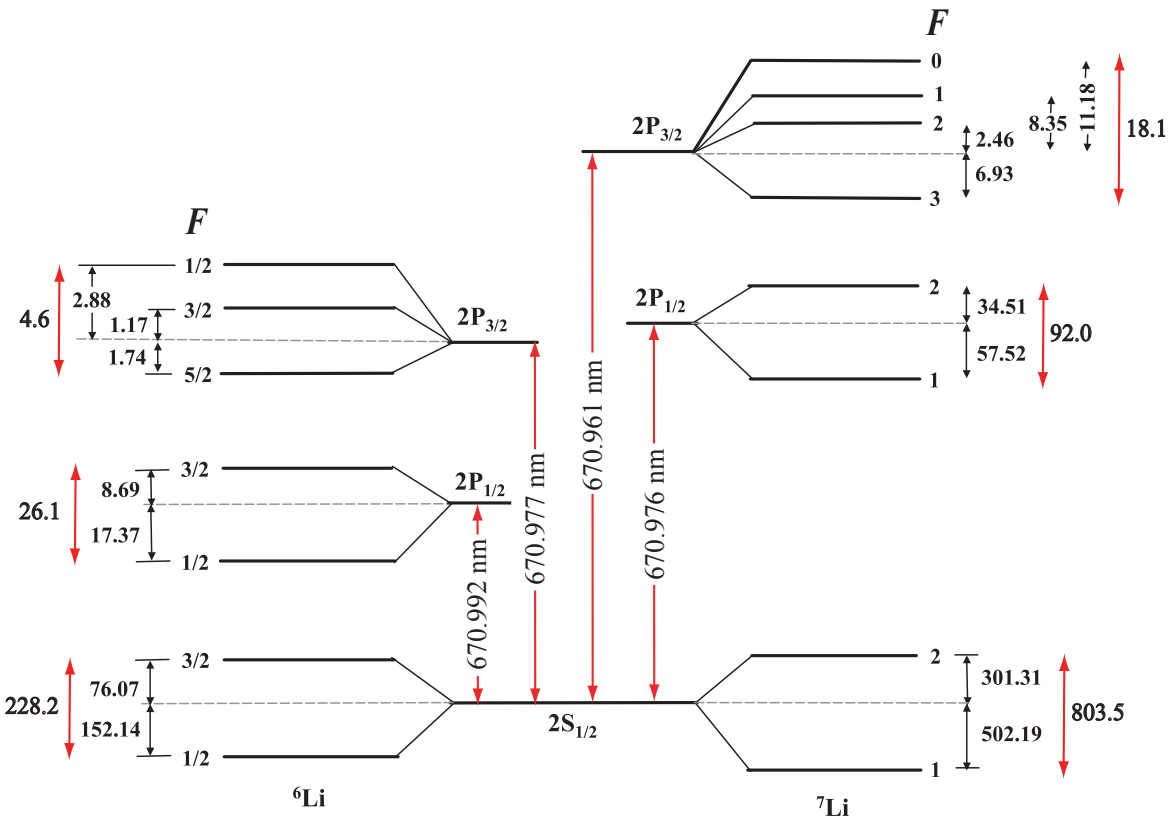

Figure 2.3: Energy levels of lithium. Frequencies in MHz.

2.3 Transition matrix elements

In a near-resonance optical transition, the strength of the transition is proportional to the square of the electric dipole matrix element. An electric dipole matrix element for a transition $|F, m_F\rangle \rightarrow |F', m_{F'}\rangle$ is

$$\langle F', m_{F'}| \boldsymbol{\mu} |F, m_F\rangle , \tag{2.7}$$

where $\boldsymbol{\mu}$ is the electric dipole operator. $\boldsymbol{\mu}$ can be described by irreducible spherical tensor operator μ_q, where q is related to the light polarization and has values -1, 0, $+1$. Using Wigner-Eckart theorem, a dipole matrix element can be factored out to a reduced matrix element and Clebsch-Gordan coefficient which can be expressed in terms of Wigner 3-j symbol[2].

$$\langle J', I, F', m'_F| \mu_q |J, I, F, m_F\rangle = \langle J', I, F'||\boldsymbol{\mu}||J, I, F\rangle (-1)^{F'-m_{F'}} \begin{pmatrix} F' & 1 & F \\ -m_{F'} & q & m_F \end{pmatrix} \tag{2.8}$$

The first term in the bracket is the reduced matrix element which is reduced such that it does not include magnetic quantum numbers m_F and $m_{F'}$ any more. The term with parenthesis is called Wigner 3-j symbol and has non-zero values when the conditions (Eq. 2.9) are satisfied.

$$\begin{aligned} &1)\, m'_F = m_F + q \\ &2)\, \Delta F = \pm 1,\ q = 0, \pm 1, \text{or}\, \Delta F = 0,\ q = \pm 1. \end{aligned} \tag{2.9}$$

The reduced matrix element$\langle J', I, F'||\boldsymbol{\mu}||J, I, F\rangle$ which contains quantum numbers $J\, I\, F$ can be further reduced. Since a transition changing F arises from change of J and no change in I, a part with J can be factored out using Wigner 6-j symbol.

$$\langle J', I, F'||\boldsymbol{\mu}||J, I, F\rangle = \langle J'||\boldsymbol{\mu}||J\rangle (-1)^{J'+I+F+1} \sqrt{(2F+1)(2F'+1)} \begin{Bmatrix} J' & I & F' \\ F & 1 & J \end{Bmatrix}. \tag{2.10}$$

Then the reduced matrix element $\langle J'||\boldsymbol{\mu}||J\rangle$ which is based on J, L, S can be further reduced using the same method.

$$\langle L', S, J'||\boldsymbol{\mu}||L, S, J\rangle = \langle L'||\boldsymbol{\mu}||L\rangle (-1)^{L'+S+J+1} \sqrt{(2J+1)(2J'+1)} \begin{Bmatrix} L' & S & J' \\ J & 1 & L \end{Bmatrix}. \tag{2.11}$$

The term $\langle L'||\boldsymbol{\mu}||L\rangle$ can be calculated by radial part integration,

$$\langle L'||\boldsymbol{\mu}||L\rangle = \langle e\mathbf{r}\rangle_{nS}^{nP} . \tag{2.12}$$

The calculation results of transition matrix elements in terms of $\langle J'||\boldsymbol{\mu}||J\rangle$ are shown in Figure. A.1 −A.5 in Appendix A.

[2]Formulas for Wigner 3-j and 6-j symbols follow definitions in [45]

2.4 Optical properties

As shown in Fig.2.3 and Table.2.5, the D1 and D2 transition wavelengths of ^{7}Li and ^{6}Li atoms are close to each other compared to other alkali atom isotopes, thus have similar values for many of optical properties. For example, the lifetime of D1 and D2 transitions of ^{7}Li and ^{6}Li are the same (27.1 ns) within the uncertainty limit [42]. Useful set of optical properties of ^{7}Li and ^{6}Li D1 and D2 lines are shown in Table.2.6. Γ is the natural linewidth of a transition, and is defined as $1/(2\pi\tau)$. Saturation intensity of D2 transition in the tables are calculated for the maximally stretched states (e.g., $|F = 2, m_F = \pm 2\rangle \rightarrow |F = 3, m_F = \pm 3\rangle$ in ^{7}Li case) using Eqn.2.13. Since lithium D2 hyperfine states are unresolved, in reality it requires bigger intensity to saturate.

$$I_{sat}(D2, \text{maximally stretched}) = \frac{\pi\hbar c}{3\lambda^3\tau} \tag{2.13}$$

An atom's recoil velocity is defined as the velocity corresponding to one photon recoil momentum; $v_{rec} = \frac{\hbar k}{m}$, thus recoil energy is $E_{rec} = \frac{\hbar^2 k^2}{2m}$, and the recoil temperature is $T_{rec} = 2E_{rec}/k_B = \frac{\hbar^2 k^2}{m\, k_B}$. Doppler temperature T_D is a theoretical minimum temperature obtained by Dopper cooling mechanism which will be discussed in section 3.2, and is defined as $T_D = \frac{\hbar\Gamma}{2}$.

Property	Symbol	^{7}Li	^{6}Li	Reference
Wavelength D_1	λ	670.976 nm	670.992 nm	[41]
Wavenumber D_1	k	$9.36425 \times 10^6\,\mathrm{m}^{-1}$	$9.36402 \times 10^6\,\mathrm{m}^{-1}$	
Transition frequency D_1	ω_o	$2\pi \times 446.801$ THz	$2\pi \times 446.79$ THz	
Wavelength D_2	λ	670.961 nm	670.977 nm	[41]
Wavenumber D_2	k	$9.36446 \times 10^6\,\mathrm{m}^{-1}$	$9.36423 \times 10^6\,\mathrm{m}^{-1}$	
Transition frequency D_2	ω_o	$2\pi \times 446.811$ THz	$2\pi \times 446.68$ THz	
Lifetime D_1, D_2	τ	27.1 ns	27.1 ns	[42]
Natural linewidth D_1, D_2	Γ	$2\pi \times 5.87$ MHz	$2\pi \times 5.87$ MHz	
Saturation intensity D_1	I_{sat}	7.59 mW/cm^2	7.59 mW/cm^2	[43]
Saturation intensity D_2	I_{sat}	2.54 mW/cm^2	2.54 mW/cm^2	
Recoil velocity	v_{rec}	8.476 cm/s	9.887 cm/s	
Recoil frequency	ω_{rec}	$2\pi \times 396.87$ kHz	$2\pi \times 462.9$ kHz	
Recoil temperature	T_{rec}	6.06 μK	7.07 μK	
Doppler temperature	T_D	142 μK	142 μK	

Table 2.6: ^{7}Li and ^{6}Li optical properties

Chapter 3

Laser cooling theory

3.1 Atom-photon interaction

Laser cooling is a technique that slows down flying atoms using laser beams. A momentum carried by a photon is transferred to an atom when there is absorption or emission by an atom. Through the repeating atom-photon scattering process an atom loses its kinetic energy and eventually get cooled. Any atoms, molecules, or ions can absorb and emit photons, but not all of them are laser cool-able. Laser cooling requires an optical transition with which an absorption-emission cycle repeats without atoms being lost to the different energy state and not interact with the laser beam.

Alkali atoms have only one electron in the outer shell thus have relatively simple energy level structure. The ground state of an alkali atom is $nS_{1/2}$ ($L = 0, J = 1/2$), and it can be excited to nP ($L = 1, J = 1/2$ or $3/2$) states through an electron dipole transition. Depending on the electron spin state the total orbital angular momentum is either $J = 1/2$ or $J = 3/2$ and the transitions are called D1 or D2 transition respectively. Each P fine structure state has hyperfine substructures ($F = |J-I|, \cdots, |J+I|$, where F is positive integer). The number F represents the total angular momentum which includes the nuclear spin I. By the selection rule ($\Delta L = \pm 1, \Delta F = 0, \pm 1$), which states that only the transitions satisfying the condition are allowed to happen, a D2 transition ($S_{1/2} \rightarrow P_{3/2}$) has nearly ideal condition to be used as a cooling beam since atoms can repeat the photon absorption-emission cycle without being lost to a different state.

In an ideal condition, a cooling transitions can be modeled as a two-level system where only a ground state and one excited state exist. In a two-level system atom, when a photon is absorbed an electron in the ground state is excited to the upper state and after a short time (typically on the order of tens of nano seconds for alkalis) the excited atom spontaneously emits a photon and the electron is back to the ground state. The decay is exponential and the characteristic time is called *life time* τ and its inverse is called *natural line width* $\Gamma(= 1/\tau)$.

The momentum of each incoming photon being absorbed $\hbar\vec{k}$ where as the momentum of an outgoing photon by spontaneous emission is in a random direction thus the average is zero. As a result an atom is effectively pushed against the laser beam- this force is called *scattering force*, and it is proportional to the photon momentum and the scattering rate.

$$F_{scat} = \hbar k \, R_{scat} \tag{3.1}$$

In the steady-state where the rate of absorption and spontaneous emission are in an equilibrium, the scattering rate can be expressed as the product of the excited state decay rate Γ and the excited state population ρ_{ee}. Optical Bloch equation, which treats the decay rate of the excited state Γ as a damping parameter, gives the steady-state solution

$$\rho_{ee} = \frac{s}{2(s+1)} = \frac{s_0/2}{1 + s_0 + (2\delta/\Gamma)^2}, \tag{3.2}$$

where s_0 is the *on-resonance saturation parameter*

$$s_0 \equiv \frac{I}{I_{sat}} = \frac{2\Omega^2}{\Gamma^2}, \tag{3.3}$$

where I is the intensity of the laser and I_s is the saturation intensity. Saturation intensity can differ depending on various conditions such as the transition type (D1 or D2), polarization of the laser beam, and the resonance conditions (on-resonance or far-off-resonance). Taking into account a detuning $\delta = \omega - \omega_0$, where ω is the laser frequency and ω_0 is the atomic resonance frequency, the saturation parameter s becomes

$$s = \frac{s_0}{1 + (2\delta/\Gamma)^2}. \tag{3.4}$$

Ω is the *on-resonance Rabi frequency* and represents the dipole-light coupling strength on resonance.

$$\Omega \equiv -\frac{e}{\hbar} E_0 \langle e | \, \hat{\epsilon} \cdot \mathrm{r} \, | g \rangle \,, \tag{3.5}$$

where E_0 is the magnitude of the electric field of the light. The bigger the Rabi frequency the faster the population oscillates between the two levels.

In an ideal two-level system, there is no other ground state which atoms can decay onto. However, in a real-life, an alkali atom has two hyperfine sub-states in the ground level ($\mathrm{n}S_{1/2}$) thus a photon in an excited state can decay onto another ground states (called dark state as an atom in this state cannot see the cooling beam any more) as long as it satisfies the selection rule ($\Delta L = \pm 1, \Delta F = 0, \pm 1$). If atoms in an excited state can fall into multiple hyperfine states of the ground state the transition can be seen as "leaky". Most of alkali atoms can have a *cycling transition* in their D2 transition which can serve effectively as a two-level system, and is normally between the maximum F states of the $S_{1/2}$ and $P_{3/2}$ levels. In reality, due to the finite linewidth and the probabilistic nature of the quantum system an

atom does not infinitely cycle between the the two states but can slowly leak into a dark state- an atom with clearly resolved hyperfine states can cycle more than millions of times before it leaks to a dark state while an atom with unresolved hyperfine states such as lithium can leak faster. Therefore in a laser cooling, a repump beam is used to pump atoms in a dark state back to the cycling transition. With a fast repumper ($\Omega >> \Gamma$) atoms stay virtually in the two-level cycling transition.

3.2 Doppler cooling

Doppler cooling mechanism uses a simple picture in a two-level system where a moving atom absorbs a photon by the Doppler effect and spontaneously emit a photon in a random direction therefore loses its kinetic energy. The scattering rate is a product of the excited state population ρ_{ee} and the decay rate Γ of the excited state.

$$R_{scat} = \Gamma \rho_{ee} \tag{3.6}$$

Using the steady-state solution for the optical Bloch equation (Eq.3.2), the scattering(radiation) force in a two-level system becomes

$$F_{scat} = \hbar k \frac{\Gamma}{2} \frac{I/I_{sat}}{1 + I/I_{sat} + (2\delta/\Gamma)^2} \tag{3.7}$$

This Doppler cooling mechanism has been used in various laser cooling apparatus and techniques such as Zeeman slower, chirp cooling, optical molasses, and magneto optical traps (MOT). Especially optical molasses technique [17, 18] is the key element of laser cooling in a MOT which is a basic and essential cooling step in a ultra-cold atom experiment. Optical molasses uses two counter propagating beam in each axis(6 beams in 3D) with red-detuned frequency such that an atom moving toward to a beam gets close to the resonance and feels the force against its motion stronger than the force toward the motion. In the low velocity limit where $kv \ll \Gamma$, the net force by 1D molasses becomes

$$F_{mol} = F_{scat}(\omega - \omega_0 - kv) - F_{scat}(\omega - \omega_0 + kv) \sim -2\frac{\partial F}{\partial \omega} kv = -\alpha v, \tag{3.8}$$

The damping coefficient α is

$$\alpha = -4\hbar k^2 \frac{I}{I_{sat}} \frac{2\delta/\Gamma}{\left(1 + (2\delta/\Gamma)^2\right)^2} \tag{3.9}$$

As shown in Eq.3.8, the cooling force by molasses is like a friction force in viscous medium. The rate of energy removed by cooling is F $\cdot$ v, therefore is proportional to v^2(or kinetic energy) whereas the heating rate is proportional to the scattering rate which is independent of kinetic energy at low velocity limit. The rate of losing kinetic energy by cooling is

$$\left(\frac{dE}{dt}\right)_{cool} = F\, v = -\alpha v^2, \tag{3.10}$$

and the rate is gaining kinetic energy by heating(scattering) is

$$\left(\frac{dE}{dt}\right)_{heat} = \frac{\hbar^2 k^2}{2m} 2R. \tag{3.11}$$

The reason for the factor 2 with the scattering rate R is because photon absorption and emission happen always in pair. In the limit of low intensity $I/I_{sat} \ll 1$, the one-photon scattering rate R becomes

$$R = \frac{\Gamma}{2} \frac{I/I_{sat}}{1 + (2\delta/\Gamma)^2}. \tag{3.12}$$

Using Eq.3.9 and Eq.3.12 the kinetic energy loss rate and gain rate become

$$\left(\frac{dE}{dt}\right)_{cool} = 4\hbar k^2 \frac{I}{I_{sat}} \frac{2\delta/\Gamma}{\left(1 + (2\delta/\Gamma)^2\right)^2} v^2, \tag{3.13a}$$

$$\left(\frac{dE}{dt}\right)_{heat} = \frac{\hbar^2 k^2}{m} \Gamma \frac{I/I_{sat}}{1 + (2\delta/\Gamma)^2}. \tag{3.13b}$$

At the equilibrium of cooling and the heating, and using $\frac{1}{2} k_B T = \frac{1}{2} m v^2$ the final temperature in a 3D molasses becomes

$$k_B T = \frac{\hbar\Gamma}{4} \left(\frac{\Gamma}{2\delta} + \frac{2\delta}{\Gamma}\right) \tag{3.14}$$

With a proper choice of δ, the temperature has its minimum, known as the Doppler temperature[1].

$$k_B T_D = \frac{\hbar\Gamma}{2} \tag{3.15}$$

3.3 Sisyphus cooling

In 1985, the Chu group at Bell labs measured the temperature of sodium cooled in an optical molasses using release and recapture technique. The result was about at 240μK [17] which is the Doppler temperature[2] for sodium at 589 nm transition with 10 MHz line width. Shortly after, in 1987 the Phillips group at NBS (National Bureau of Standards, now NIST) observed much lower temperature (about 40 μK[21] measured by time of flight method) than Doppler temperature, and it ignited searching the explanation for the sub-Doppler cooling mechanism. After they observed the first sub-Doppler temperature, Philips group confirmed sub-Doppler temperature by different methods and confirmed other experiment result disagreeing with Doppler cooling theory, such as temperature dependency on laser frequency detuning and high sensitivity of temperature on stray magnetic field. Soon, Chu group at Stanford and Cohen-Tannoudji in France also confirmed sub-Doppler temperature.

[1] Rigorous derivations can be found in [19, 20]

[2] Later they found that this temperature was due to stray magnetic field from their equipment and they could have much lower temperature.

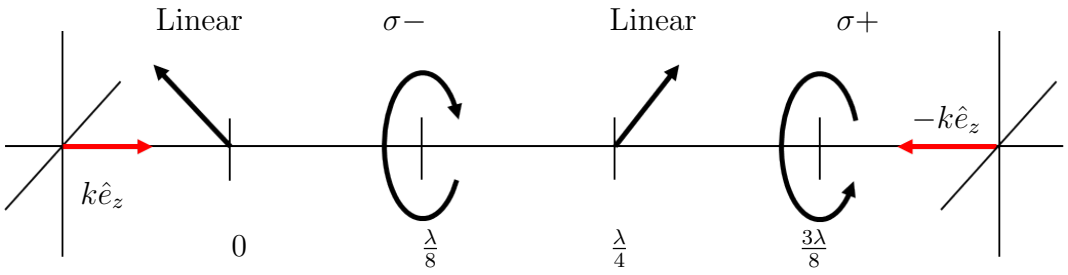

Figure 3.1: Polarization gradient in a standing wave formed by two counter-propagating orthogonal linearly polarized beams

Since the Doppler limit was rigorously derived for two-level system, people approached a multi-level system[3].

3.3.1 Sisyphus mechanism

Dalibard and Cohen-Tannoudji developed a cooling theory by combination of polarization gradient, multilevel structure, light shift and optical pumping, known as Sisyphus cooling [22]. Chu group also developed a theory explaining sub-Doppler cooling independently [23]. Although the key factors for two theories are the same (multilevel atom and population transfer between those sublevels), Dalibard and Cohen-Tannoudji's Sisyphus picture is visually easier to understand and is widely known, therefore will be discussed in this section.

In a standing wave formed by two counter-propagating laser beams with orthogonal linear polarizations, the resulting polarization becomes spatially modulated as shown in Fig. 3.1. In a standing wave, the periodicity doubles compared to the original wavelength λ of one beam, therefore the polarization repeats in every half-wavelength. Now, we can consider a multilevel atom D2 transition (the transition used for laser cooling of alkali atoms) where ground state has an angular momentum of $J = 1/2$ and the excited state lies at $J = 3/2$. Fig. 3.2 shows the magnetic sublevels (degenerate under no magnetic field and no light shift) for $J' = 3/2$ and $J = 1/2$ states and transition strengths between sublevels. As always, the transitions between maximally stretched states (meaning bigger absolute value of M_J) are strongest. Fig. 3.3 shows that those magnetic sublevels break degeneracy due to light shift. The energy of ground state magnetic sublevels are spatially modulated due to the polarization gradient. When an atom is at the position where the standing wave has a circular polarization (e.g. $z = \lambda/8, 3\lambda/8, \cdots$), it drives transitions with $\Delta M_J = \pm 1$ (the value +1 is for σ^+ and -1 is for σ^-). Here, the optical pumping rate is sufficiently slow (i.e., low Rabi frequency) compared to the excited state decay rate such that atoms don't pile up onto dark state instantly and it allows enough time to decay spontaneously and lose energy. In the case of atoms traveling near $z = \lambda/8$ where polarization is $\sigma-$, only those atoms

[3]The review is from [26]. Steven Chu, Claude Cohen-Tannoudji, and William D. Phillips awarded Nobel prize in 1997 for their contribution to the laser cooling.

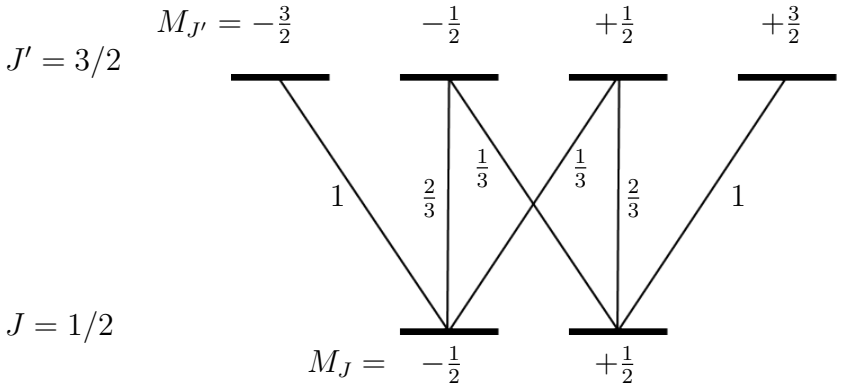

Figure 3.2: Simplified energy levels for electric dipole transition with the ground state J=1/2 to the excited state J'=3/2, and the transition strengths(Clebsch-Gordan coefficient squared).

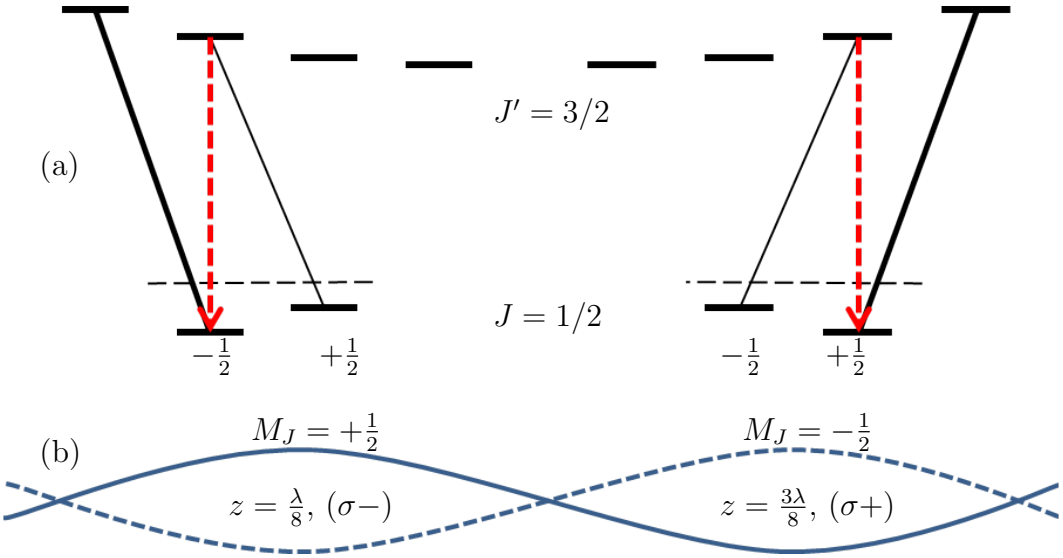

Figure 3.3: Light shift of sublevels (a) and energy level spatial dependence (b). Red dotted arrows are spontaneous decay which contribute to cooling. Left: at $z = \lambda/8$,where the polarization is $\sigma-$, Right: at $z = 3\lambda/8$,where the polarization is $\sigma+$. Light shift is bigger for the transition with bigger transition probability.

being pumped from the $M_J = +\frac{1}{2}$ ground state to a excited state and decaying to $M_J = -\frac{1}{2}$ ground state (lowest energy) can contribute to cooling. The cooling is most efficient at the position where the polarization is purely circular; when an atom moves away from it the efficiency drops. In the energy level picture of ground states, the cooling is most efficient where the energy difference of two ground states $M_J = \pm\frac{1}{2}$ is the biggest. Therefore as shown in Fig.3.4, an atom in a state with the lowest energy climbs up the hill (simply because the potential energy increases) as the atom moves away from the position and then at the top

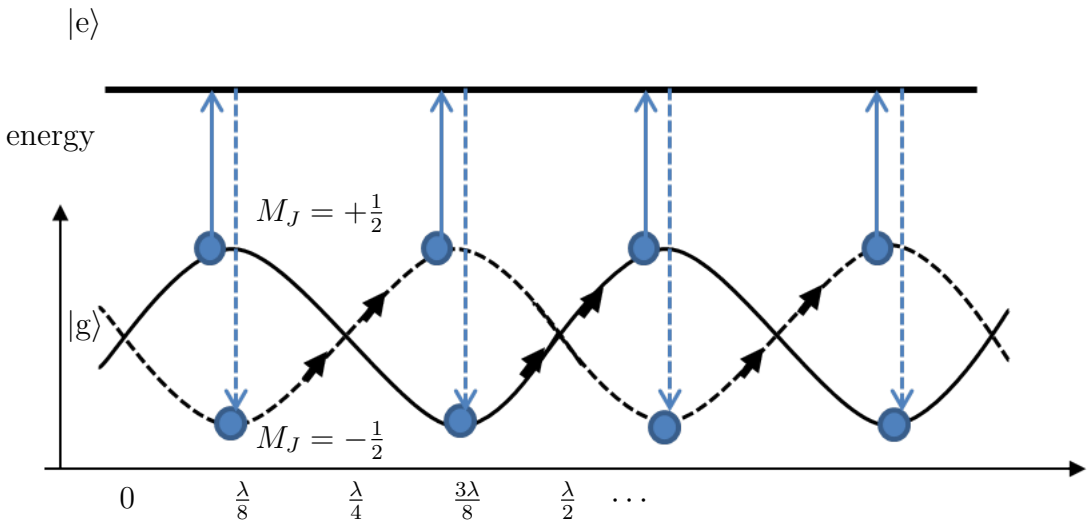

Figure 3.4: Cartoon picture of Sisyphus cooling mechanism. Dotted blue arrows represent spontaneous emission.

the spontaneous decay occurs most strongly so the atom falls to the other magnetic sublevel which now has the lowest energy, and then the cycle repeats as the atom moves along. Since the atom climbs up the potential energy hill and falls back down from the top again and again, this mechanism got the name "Sisyphus cooling" named after Sisyphus from Greek mythology. From this picture, one can easily see that the origin of cooling is converting the kinetic energy of an atom to its potential energy. Therefore, intuitively, the limit of the equilibrium temperature is on the order of the potential energy difference between two ground states due to light shifts. The light shift difference is on the order of standing wave potential energy U_0.

$$k_B T_{eq} \simeq U_0 \propto \frac{I}{|\delta|} \tag{3.16}$$

However, the equilibrium temperature does not continue to go down as the light potential energy decreases. The velocity capture range is narrower (therefore the cooling works less) for smaller intensity (or smaller potential) since capture velocity for Sisyphus cooling is roughly determined by that the distance an atom travel during the optical pumping time scale is less than a half wavelength ((3.3.1)).

$$v\tau_{pump} \leq \lambda/2, \tag{3.17}$$

where $1/\tau_{pump}$ is the optical pumping rate, summing up the pumping rates $\gamma_+(|g_{+\frac{1}{2}}\rangle \rightarrow |g_{-\frac{1}{2}}\rangle)$ and $\gamma_-(|g_{-\frac{1}{2}}\rangle \rightarrow |g_{+\frac{1}{2}}\rangle)$ at the top of the hills:

$$\frac{1}{\tau_{pump}} = \gamma_+ + \gamma_- = \frac{2}{9}\gamma s_0, \tag{3.18}$$

where $\gamma = \Gamma/2\pi = 1/\tau$ is the inverse of the excited state lifetime. The capture velocity becomes

$$v_c = \frac{p_c}{m} = \frac{\Gamma s_0}{9k}, \tag{3.19}$$

thus the Sisyphus cooling becomes inefficient when the light potential becomes too small. Another important fundamental limit of temperature obtainable by sisyphus cooling is the recoil limit, since the energy loss is due to spontaneous emission which still gives the recoil energy to the atom. Anyways, however, in reality the resulting temperature by only Sisyphus cooling is much higher than the recoil temperature, $T_r = \frac{\hbar^2 k^2}{m}$.

An analytic expression of an equilibrium temperature by Sisyphus cooling can be obtained by a semi-classical approach [25]. In steady state, the momentum distribution is determined by the equilibrium of the cooling due to Sisyphus effect and the heating due to momentum diffusion. The Sisyphus cooling force is expressed as

$$f(p) = -\frac{\alpha p}{1 + (p/p_c)^2}, \tag{3.20}$$

where

$$\alpha = \frac{kU_0}{2p_c} = -3\hbar k^2 \frac{\delta}{\Gamma}, \tag{3.21}$$

and the diffusion coefficient is expressed as

$$D(p) = \frac{D_1}{1 + (p/p_c)^2} + D_0, \tag{3.22}$$

where

$$D_1 = \frac{k{U_0}^2}{4p_c} = \hbar^2 k^2 \Gamma s_0 \frac{\delta^2}{\Gamma^2}. \tag{3.23}$$

In steady state and assuming atoms are not localized in the potential, the momentum distribution becomes

$$\psi(p) = \psi(0) \exp\left(\int_0^p \frac{f(p')}{D(p')} dp' \right). \tag{3.24}$$

In the case of large U_0 where D_0 is negligible compared to the first term in $D(p)$, the momentum distribution becomes Gaussian and the equilibrium temperature becomes

$$k_B T = \frac{D_1}{\alpha} = \frac{U_0}{2}. \tag{3.25}$$

When D_0 is not neglected, the momentum distribution becomes

$$\psi(p) = \frac{\psi(0)}{(1 + (p/\bar{p_c})^2)^A}, \tag{3.26}$$

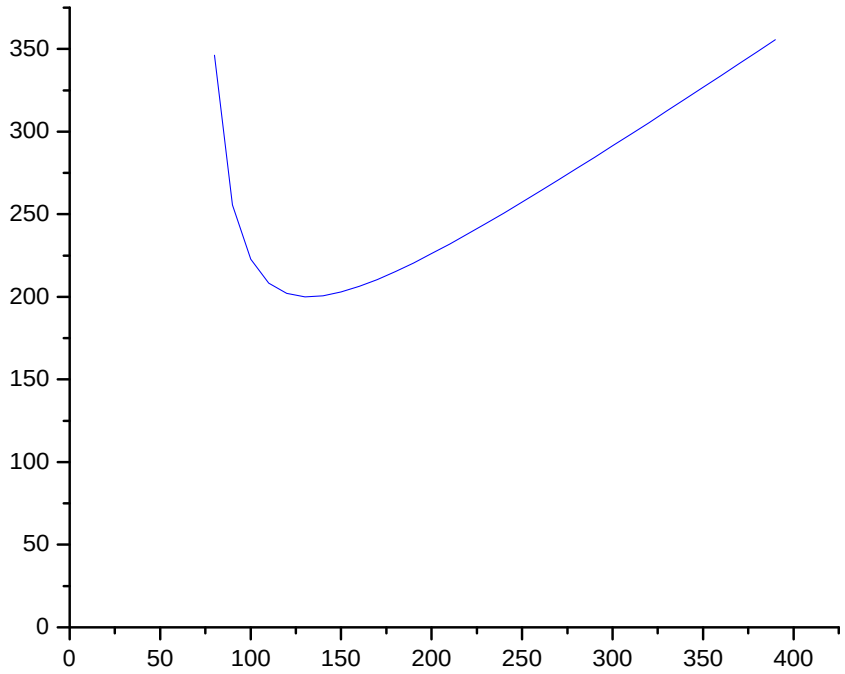

Figure 3.5: Plot of equilibrium temperature as a function of U_0 as the result from semi-classical approach without localization.

where

$$\begin{aligned} \bar{p_c} &= p_c\sqrt{1+D_1/D_0} \approx \frac{\hbar k}{\sqrt{88}}\frac{U_0}{E_r} \text{ for } \delta \gg \Gamma \\ A &= \frac{U_0}{44E_r}. \end{aligned} \tag{3.27}$$

Expectation value of kinetic energy gives the Sisyphus cooling temperature as a function of U_0:

$$\bar{E_k} = \frac{{U_0}^2}{4(U_0 - 66E_r)}. \tag{3.28}$$

Figure 3.5 shows the plot of equation (3.3.1), the equilibrium temperature by the Sisyphus cooling is proportional to the potential depth U_0 for large U_0, but the temperature also increases as U_0 becomes too small that the Sisyphus cooling becomes inefficient. The lowest cooling temperature occurs at $U_0 = 132E_r$ with $T = 33T_r$ which is approximately 200 μK for ^{7}Li.

Although this analytic expression captures important intuition- equilibrium between the cooling force and the heating due to momentum diffusion, it ignores the quantum effect such as localization of atoms in the light potential. With this correction the minimum cooling temperature lowers than that of the analytical expression, but the over all behavior is the same- i.e., the temperature is minimum at around $U_0 \sim 100\,E_r$ and increases as U_0 gets either smaller or bigger. The full quantum treatment is described in detail in [25] for the Sisyphus cooling in D2 transition. As the result, the minimum kinetic energy is about $40\,E_r$ ($T \approx 20\,T_r$) which is about 60% of the semi-classical result without localization. So far, we have discussed the Sisyphus cooling in D2 transition which is more commonly used for laser cooling than D1 because D2 transition has a cycling transition.

3.3.2 Sisyphus cooling in D1 and D2 transitions

It is less well-known that Sisyphus cooling also works for blue detuning. While Sisyphus cooling works only for red detuning near D2 transition ($J' = 3/2$), it works for only blue detuning near D1 transition ($J' = 1/2$). This is because the minimum and maximum position for a light shift is reversed for $J' = 1/2$ compared to $J' = 3/2$ case[4]. In a standing wave formed by two counter-propagating linear polarized beams which an angle θ between their polarizations, the light shift potential for D1 and D2 transitions ($J' = 1/2$ and $J' = 3/2$) becomes

$$U_{\pm}{}^{J'=1/2} = U_0^{J'} \cos^2(k\,z \pm \theta/2), \tag{3.29a}$$

$$U_{\pm}{}^{J'=3/2} = U_0^{J'} \left(\cos^2(k\,z \mp \theta/2) + \frac{1}{3}\cos^2(k\,z \pm \theta/2) \right), \tag{3.29b}$$

$$\text{with } U_0^{J'} = \frac{\hbar\Omega^2}{2(-\delta_{J'})} \left(\frac{\hat{\mathrm{D}} \cdot \hat{\mathrm{D}}^\dagger}{3} \right) \tag{3.29c}$$

The $\pm$sign in $U_\pm$ means the sign of ground state M_J value($M_J = \pm 1/2$). The expression for the potential depth U_0 assumes $\delta \gg \Gamma$, and the peak intensity is used for Rabi frequency Ω, which is defined as

$$\Omega = \Gamma \sqrt{(\frac{2P_0}{\pi {w_0}^2})/I_s}, \tag{3.30}$$

where P_0 is a single beam power. The factor $\frac{\hat{\mathrm{D}}\cdot\hat{\mathrm{D}}^\dagger}{3}$ is the scalar component of dimensionless atomic polarizability tensor $\hat{\mathrm{D}}\hat{\mathrm{D}}^\dagger$, and can be expressed as

$$\frac{\hat{\mathrm{D}} \cdot \hat{\mathrm{D}}^\dagger}{3} = \frac{1}{3}\left(\left|\mathrm{C}^{1/2,J'}_{m,m-1}\right| + \left|\mathrm{C}^{1/2,J'}_{m,m}\right| + \left|\mathrm{C}^{1/2,J'}_{m,m+1}\right| \right) = \begin{cases} \frac{2}{3}, & J' = 3/2 \\ \frac{1}{3}, & J' = 1/2. \end{cases} \tag{3.31}$$

[4]This is true only when the standing wave has orthogonally polarized. In arbitrary angled linear polarized beams, the resulting potential has some phase shift to each other.

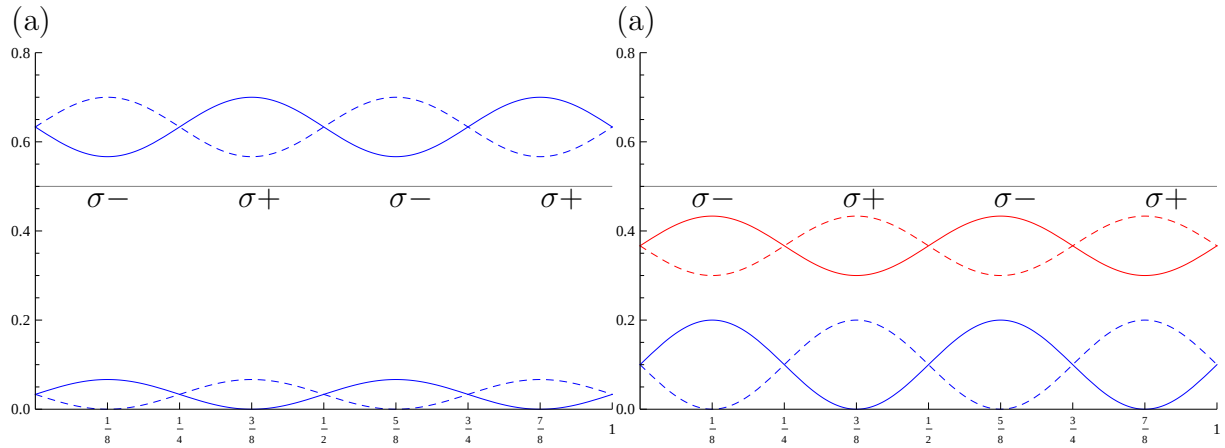

Figure 3.6: Light shift potential for D1 and D2 transitions in ^{7}Li with the same light intensity. The x-axis is z/λ, and the y-axis is energy in an arbitrary scale. The upper curves represent potential of the ground states due to D2 transition ($J' = 3/2$), and the lower curves represent those from D1 transition ($J' = 1/2$). An arbitrary constant is added to the $U_{\pm}^{J'=3/2}$ (upper curves) for display purpose. Detunings for (a) +5 GHz to D2 (+15 GHz to D1), and (b) for -5 GHz to D2 (+5 GHz to D1). The blue color represent the detuning is positive to the corresponding transition resonance while the red color means negative detuning to the corresponding resonance. Solid line: U_+ ground state $M_J = 1/2$, Dashed line: U_- ground state $M_J = -1/2$.

A real-space component (with an index μ) of the operator $\hat{\mathrm{D}}^\dagger$ is defined as

$$\begin{aligned} \hat{D_\mu}^\dagger &= \sum_{m'} |J', m\rangle \langle J', m'| \hat{\mathbf{e}}_\mu |\frac{1}{2}, m\rangle \langle \frac{1}{2}, m| \\ &= \sum_q \hat{\mathbf{e}}_\mu \cdot \epsilon_q \mathrm{C}^{J,J'}_{m,m+q} |J', m+q\rangle \langle \frac{1}{2}, m| , \end{aligned} \tag{3.32}$$

where $\hat{\mathbf{e}}_\mu$ is a unit vector along direction of μ, ϵ_q is a unit polarization vector.

The potential depth is defined such that the red detuning in the D2 transition potential is positive (3.29c). The ground states potentials $U_\pm(z)$ for the D1 and D2 transitions are shown in Fig. 3.6. In the standing wave which polarizations are orthogonal, ground states for the D1 and D2 are out of phase for the same detuning polarity as shown in Fig. 3.6 (a). Note that at $z = \lambda/8$ the standing wave polarization is $\sigma-$. To make the cooling happen in the $\sigma-$ light, $M_{J=+1/2}$ ground state light potential should be higher than $M_{J=-1/2}$ ground state light potential. Therefore blue detuned D1 transition can have Sisyphus cooling whereas the Sisyphus cooling works for red detuning in D2. Fig. 3.6 (b) shows that the ground states potential for D1 and D2 are in phase and the Sisyphus cooling works for both. On the other hand, when detunings are both blue to D1 and D2 as in (a), a heating occurs in D2

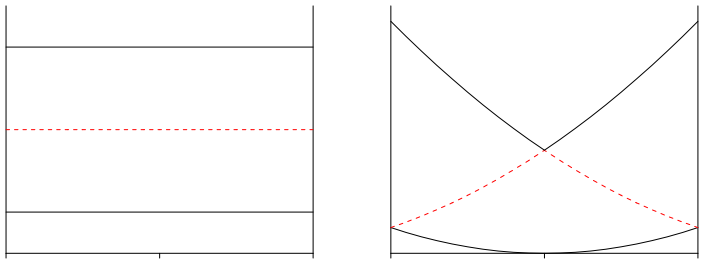

(a) Tight binding band (b) Free particle band

Figure 3.7: Band structures

while cooling in D1 thus the over all Sisyphus cooling becomes inefficient in the case where detunings are both blue to D1 and D2; for the similar reason, Sisyphus cooling does not work well in the case where detunings are both blue to D1 and D2.
For both ^{7}Li and ^{6}Li, the energy level structure has 10 GHz separation between D1 and D2 transitions which are close enough that one laser frequency can drive both D1 and D2 transitions with a moderate laser power. Our experimental observation of the Sisyphus cooling in both D1 and D2 transition is discussed in section 5.2.1.

3.4 Adiabatic cooling

Another cooling mechanism by a standing wave comes from an adiabatic turn-off of a lattice [24]. When atoms are trapped in the light potential they can be modeled as tight-binding model of band theory, and one potential well can be modeled as a harmonic potential. As the potential is gradually decreased, the harmonic potential gradually transforms to the free particle band structure, and the atoms that are originally in the tight-binding bands are adiabatically transferred into the corresponding free-particle bands, therefore ideally the population stays the same as in the tight-binding model. A probability distribution of a n^{th} state in a harmonic potential is described by Maxwell-Boltzmann distribution

$$\mathrm{P}_n = e^{-\frac{n\hbar\omega}{k_B T}}, \tag{3.33}$$

where $\omega = 2E_r/\hbar\sqrt{U_0/E_r}$. The resulting initial population of a n^{th} state becomes

$$\pi_n = (1 - e^{-\frac{\hbar\omega}{k_B T}})e^{-\frac{n\hbar\omega}{k_B T}}. \tag{3.34}$$

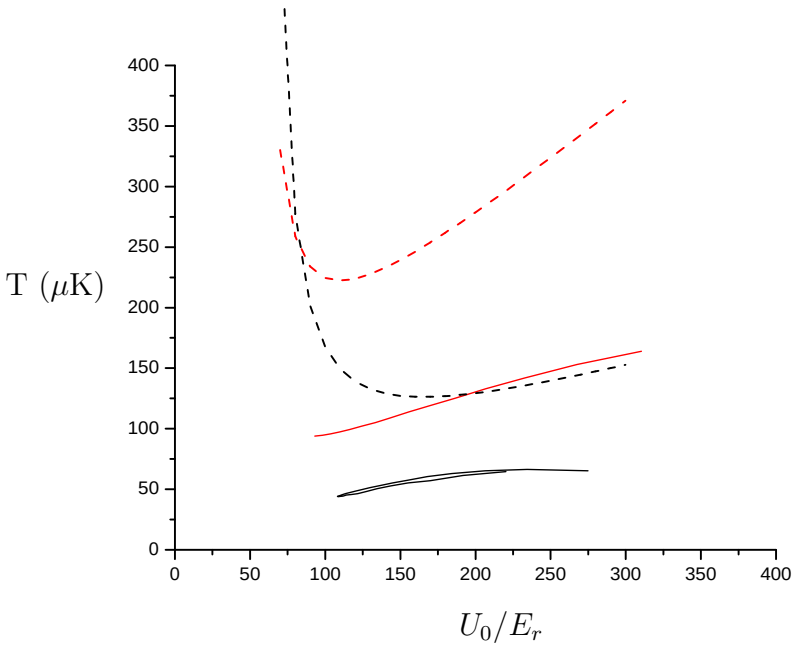

Figure 3.8: Simulation results. Dashed lines are semi-classical calculations and solid lines are calculations using quantum treatment. Red color indicates that only Sisyphus cooling is considered whereas black color indicates that both Sisyphus and adiabatic cooling are included. The same simulation result of the cooling temperature as a function of detunings has been presented in our published paper [29]

The temperature of the system can be obtained by averaging kinetic energy over all the bands.

$$\frac{1}{2}k_B T_f = \sum_n \frac{\pi_n}{\hbar G} \int_{n^{th}BZ} \frac{p^2}{2m} dp \tag{3.35}$$

$$= \frac{\hbar^2 G^2}{3m} \frac{6 + a(3+a)}{8a^3}(1 - e^{-a}), \tag{3.36}$$

where $a \equiv \frac{\hbar\omega}{k_B T}$.

Figure 3.8 shows the simulation results for 1) Sisyphus cooling without adiabatic cooling and 2) Sisyphus cooling with adiabatic cooling in semiclassical and quantum calculations. For calculation of adiabatic cooling, it was assumed that the adiabatic cooling begins after Sisyphus cooling reaches an equilibrium temperature. $T_r = 6.06\,\mu$K is used for ^{7}Li recoil temperature and $I_s = 3.8$ mW is used for effective saturation intensity.

Chapter 4

Apparatus

4.1 Designing and building lasers

In this section, as the key parts in our experimental setup, our home-build lasers (external cavity diode laser, slave laser, tapered amplifier), home-build spectroscopy setup and phase lock setup will be discussed. Our home-built lasers are stable and perform as good as commercial lasers yet the cost is far cheaper.

4.1.1 External Cavity Diode Laser

In cold-atom physics and precision measurement experiments the most essential piece in the setup is a stable laser that can produce a reference frequency. Required qualities of a good reference laser are 1) well-defined frequency (i.e., single-frequency mode operation and narrow frequency linewidth), 2) long-term stability of the frequency, and 3) wide wavelength tunability.

Types of tunable diode lasers

A semiconductor laser diode is an economic option for building a stable and tunable laser. The simplest laser diode that has a gain medium waveguide with two parallel surface ends acting as an internal cavity is called a Fabry-Perot (FP) laser diode. A FP laser diode alone may operate at single frequency mode under certain conditions, however it is usually neither stable nor tunable. In this reason, an optical feedback is needed to operate at single frequency mode or to tune the laser frequency.

The optical feedback element can be either internal or external. Examples of a diode laser with an internal feedback element are a distributed feedback (DFB) laser and a distributed Bragg reflector (DBR) laser. Both DFB and DBR have an internal micro grating structure called Bragg reflector. In a Bragg reflector, a small amount of light is reflected over each

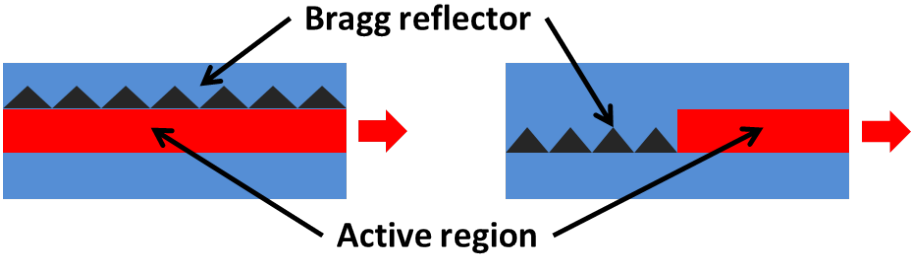

Figure 4.1: Diode lasers with internal grating structures. DFB laser(left) and DBR laser(right).

period of the grating and acts as an optical feedback. The difference is that a DFB has the micro grating structure inside its active region while a DBR has the grating outside the active region (Fig.4.1). In DBR, one of the Fabry-Perot facets of the active region is replaced by the Bragg reflector. A DFB laser has a large (typically a few nm) continuous wavelength tuning range without a sudden jump between multiple frequencies (called a "mode-hop"). A DBR laser gives a higher continuous-wave (cw) power than a DFB at the expense of its tuning range.

In contrast to DFB and DBR, an external cavity diode laser (ECDL) uses an external element for feedback. An ECDL consists of a simple FP laser diode and an external feedback element such as a grating or an interference filter. An ECDL offers a wider coarse tuning range than a DFB although it is not mode-hop-free as in a DFB. The linewidth of an ECDL is typically narrower (< 1 MHz) than that of a DFB laser (1-10 MHz). Since an ECDL has a feedback element not built inside the diode, it has more design flexibility. In our experiment we build an ECDL for its wide tuning range and design flexibility. We choose a grating over an interference filter because a grating is significantly cheaper than an interference filter.

How a grating laser works

A simple grating laser consists of a laser diode, a collimation lens, a grating on a mirror mount, a piezoelectric actuator, and electronics for current and temperature control. As shown in Fig.4.2, the laser light emitted from a diode is collimated by a short focal length lens and is diffracted by a grating. The beam directly reflected by the grating surface is called zeroth order, and becomes the output light. The first-order diffracted beam goes back into the diode as an optical feedback. Since the feedback light frequency and strength depend on the grating angle, the laser frequency can be tuned by changing the grating angle. A piezoelectric actuator helps the fine tuning of the grating angle. Temperature and current control units help frequency tuning as well as stabilization.

The two major configurations for ECDL lasers are Littman-Mefcalf [7] configuration and

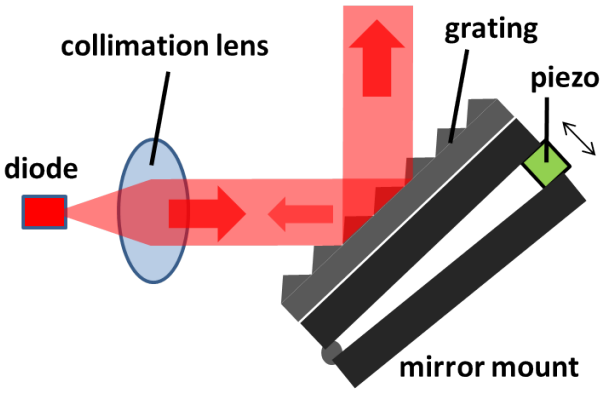

Figure 4.2: Schematic of an ECDL

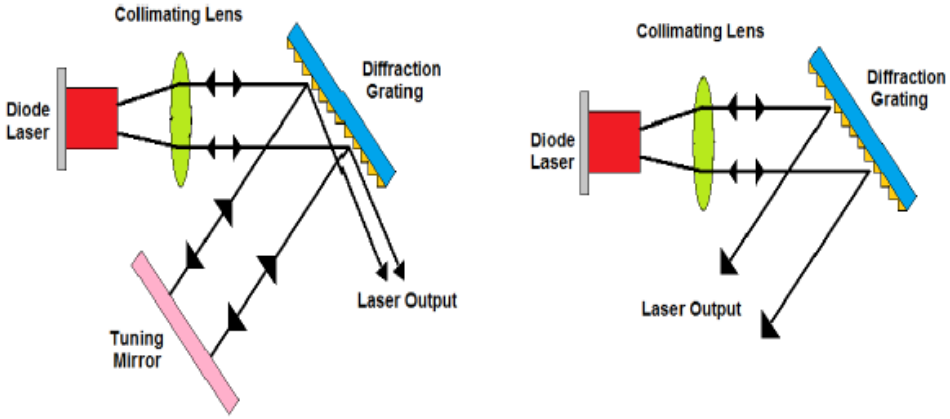

(a) (b)

Figure 4.3: Major configurations of ECDL. (a) Littman-Metcalf, (b) Littrow configuration. Figures are from [8].

Littrow configuration (Fig. 4.3). Littman-Metcalf configuration has advantage that beam does not move position when tuned, however its output power is lower. Littrow configuration is simple and has good output efficiency ($\sim 50\%$), however the beam position changes when the grating is tuned. Our homemade grating laser uses Littrow configuration since it is simple and gives higher power. Beam position change due to grating tilting is not very important for us since we keep grating angle fixed for our application.

Figure 4.4 shows various factors contributing to the final gain spectrum of a grating laser. A broad gain spectrum is determined by the laser diode gain medium whose spectrum width can be as large as 10 nm. The Fabry-Perot cavity modes by the diode internal cavity have a periodic shape gain spectrum with peaks separated by the cavity's free spectral range (FSR). The overall gain spectrum of a free-running (no feedback) FP laser diode is determined by

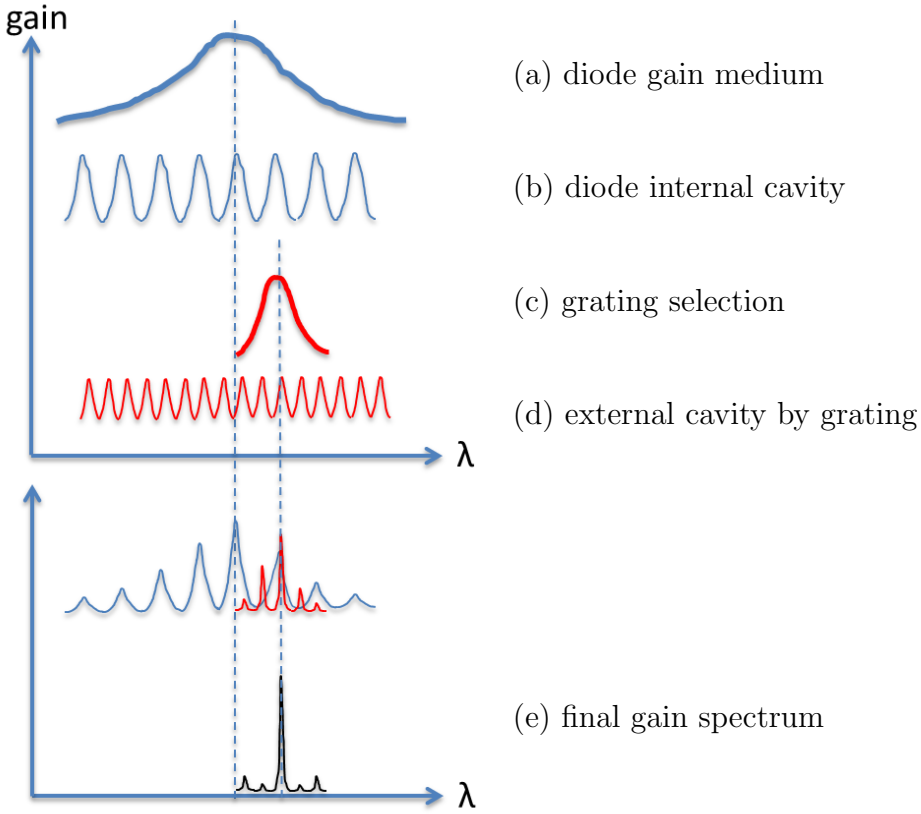

Figure 4.4: An example illustration of a gain spectrum of a grating laser and contributing factors. Plots not in scale.

the product of the medium gain spectrum and the internal cavity gain spectrum. As a result a free-running FP laser lases at a frequency (or multiple frequencies) where the biggest peaks are in the overall FP diode gain spectrum.

The laser light from a diode is dispersed by the grating diffraction and only a small range of frequency component can return to the diode; therefore a grating acts as a frequency filter. Grating also acts as an external cavity which length is the distance between the laser diode and the grating. Since the external cavity length (a few cm) is much larger than the cavity length of the diode (hundreds μm) it forms a periodic gain spectrum with much finer combs. The final lasing frequency of an ECDL is determined by the final gain spectrum (product of these four factors) from which one of the frequency modes is amplified in the system.

Temperature and diode current also can affect the lasing frequency. A change in ambient temperature affects the band gap of the Fabry-Perot laser diode. An increase in temperature increases the lasing wavelength in a stair case form, where the gaps represent mode-hops

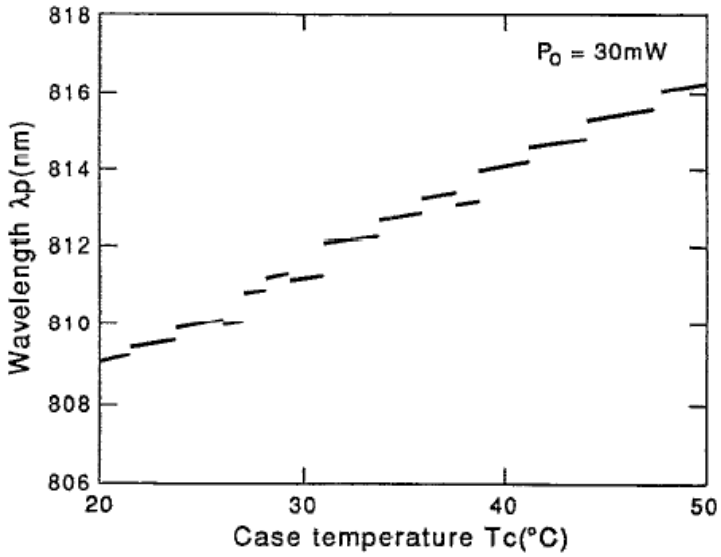

Figure 4.5: Example of temperature dependence on lasing wavelength. Figure is adapted from[9]

(Fig.4.5). An increase in diode current heats the active layer of the diode resulting in an increase of the wavelength. Tuning the wavelength of a laser diode by diode temperature and current does not cover the entire range of wavelengths. Optical feedback by a grating can improve stability and cover the regions not accessible by FP diode alone.

ECDL design

A laser diode and a grating are the major components of an ECDL. The choice of a laser diode should be determined by requirements such as laser wavelength, power, and beam profile. For example, in our experiment we use ^{7}Li atoms with an optical transition at 670.962 nm. Therefore the required laser wavelength is around 670 nm. The laser should have enough power for spectroscopy and other optics setups which require about 15-20 mW in our experiment. The required beam profile for a frequency reference laser is the TEM00 mode, also called single-spatial-mode. However there is no commercially available 670 nm single-spatial-mode laser diode with a power stronger than 15 mW. Considering that a grating reflection efficiency is typically about 50%, a 15 mW 670 nm laser diode does not satisfy our laser power requirement. Therefore we choose to use a 60 mW 664 nm single-mode laser diode (Hitachi HL6555G) and pull the wavelength using a grating and heating the diode.

A reflection grating is typically used for a grating laser. There are two major types of reflection gratings: ruled grating and holographic grating. A ruled grating (also called blazed grating) has asymmetric faces and gives more design degrees of freedom. It is made of metal

and has higher diffraction efficiency (more than 50%). This type of grating , however, can have undesired non-diffracted stray light spots due to periodic error of the blaze (called a "ghost effect"). A holographic grating has symmetric, sinusoidal faces made of photoresist. It gives less diffraction efficiency than a blazed metal grating, yet it can be as good as 50% or more at certain wavelengths. A holographic grating does not suffer a ghost effect, and is recommended for use when the grating groove density (number of grooves per milimeter) is more than 1200/mm, since the ghost effect becomes more severe with higher groove density. On the other hand, a ruled grating is recommended for wavelength longer than 1.2 μm, or when the groove density is less than 600/mm. It is also important to choose a wavelength band (such as UV, VIS, or IR) with good efficiency at the desired wavelength (e.g. VIS for our setup).

To determine the required groove density (number of grooves per milimeter) of a grating, one can use the grating equation (Eqn.4.1), where d is the distance between the grating teeth, and m is the diffraction order.

$$d(\sin(\theta_i) + \sin(\theta_m)) = m\,\lambda \tag{4.1}$$

By conservation of energy $E_{in} = \sum_{m=-\infty}^{\infty} E_m$, where E_m is the energy of the diffracted light with m-th order, the energy is distributed among diffracted beams including the 0th order beam. It is desirable to choose the incident angle large enough such that diffraction orders other than the zeroth and the first order do not appear ($E_m = 0$ for $m \geq 2$). The feedback light overlaps with incident light ($\theta_i = \theta_{m=1}$), then the grating equation becomes

$$2d\,\sin(\theta_1) = \lambda \tag{4.2}$$

Putting Eqn.4.2 into Eqn.4.1, for an m-th order beam it becomes

$$\sin(\theta_m) = \frac{\lambda}{d}\left(m - \frac{1}{2}\right) \tag{4.3}$$

At λ= 671 nm, m=2, $\theta_2 = 90^\circ$ we find that the minimum groove density occurs at about 994/mm, therefore any grating with more than 1000/mm gives only the zeroth and the first order diffraction. For design purposes it is convenient to set $\theta_1 = 45^\circ$, so that the output beam(0th) comes out at 90°. Putting this condition into the equation, the groove density becomes about 2100/mm. Since a 2100/mm grating is not commercially available, we use a 2400/mm grating. Our test shows that both 1800/mm and 2400/mm work well.

When using a grating, the beam polarization orientation is important since there is a strong polarization dependance in diffraction efficiency as groove density gets larger. The diffraction efficiency is higher for polarization perpendicular to the grating lines and lower for polarization parallel to the grating lines. At 670 nm the diffraction efficiency for the two gratings is about 20 % for parallel polarization. We use parallel polarization such that the major power

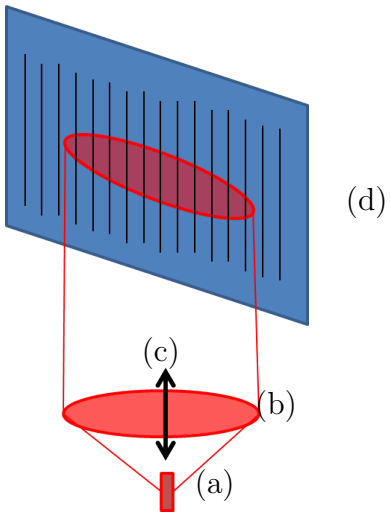

Figure 4.6: Laser beam polarization and beam orientation. (a) diode facet, (b) beam shape at the far field, (c) polarization, and (d) grating. A laser beam with parallel polarization and perpendicular long-axis to the grating grooves yields higher power output and higher resolution.

is in the output beam (0th order) and a small amount of power is in the 1st order beam for optical feedback. The polarization coming out of a diode is usually along the short axis of the far field beam profile (Fig.4.6). The beam shape in which the long axis is perpendicular to the groove lines is advantageous since it gives higher diffraction resolution. Some diodes can have special internal geometry such that the polarization is along the long axis of the far field beam. Then one can use a half wave plate to rotate the polarization in order to have both higher output power and higher resolution.

Laser housing and assembly

Our laser housing has a double-box structure to enhance temperature stability. The double box consists of an inner box containing the optics elements, an outer box which serves as a heat sink, and a thermoelectric cooler/heater (TEC) between the inner box and the outer box (Fig.4.7). In our ECDL the laser diode should be heated to produce a longer wavelength than its center wavelength. The entire inner box is heated by a TEC. The hot face of the TEC is under the inner box base and the cold face is placed on the outer base. To increase thermal conductivity between base plates and the TEC, a thermal paste is applied on the TEC surfaces. Instead of metal screws, nylon screws are used for connecting the inner base, TEC and the outer base, to avoid heat transfer between the hot inner base and the cold outer base heat sink. The inner box enclosure minimizes the air circulation between hot inner optics and the cold outer enclosure. The laser beam exits through the anti-reflection (AR) coated windows on both the inner and outer boxes. These enclosures, along with window sealing, provide improved thermal stability and better laser performance.

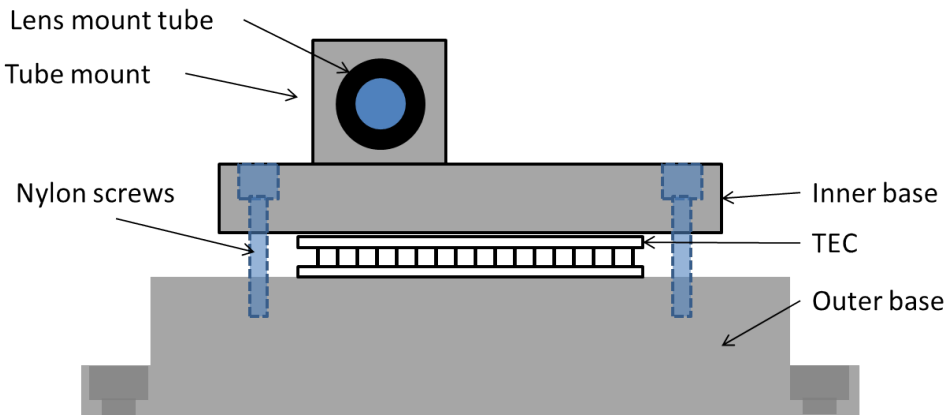

Figure 4.7: Grating laser side view. Box walls are omitted in the drawing.

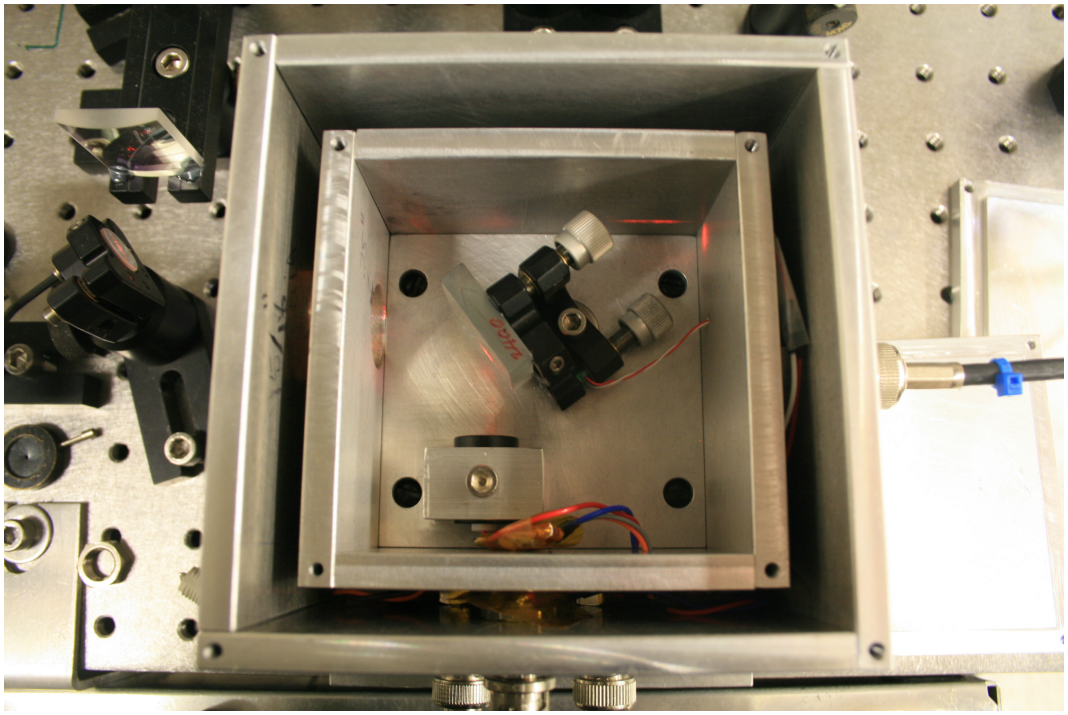

Figure 4.8: Grating laser housing

Mechanical stability is also very important for improving the performance of a laser. Our design is kept simple and compact to reduce vibration and to enhance mechanical stability. A lens mount holder is made as a one-body with the inner base. On the inner base there is a threaded hole to accommodate a simple mirror mount. A 5 mm long piezo-electric actuator is placed between the mount face and the horizontal knob to modulate fine angle of the grating. A grating is glued onto a compact mirror mount, and the mirror mount is firmly bolted and glued onto the inner base. On the laser diode socket, a protection circuit made of series of diodes to limit the maximum forward and any reverse voltage. A laser diode sits on the socket and is placed in the lens tube with a f=4.5 mm aspheric collimation lens. When the collimation is optimized by fine adjusting the lens position, the lens tube is placed in the tube mount on the inner box plate, and is rotated so that the long axis is perpendicular to the grating groove lines. The lens tube is tightly mounted on the tube mount[1]. The distance between the laser diode and the grating is about 2 cm; this short length makes the cavity less sensitive to mechanical bending or vibration of the base plate. AR-coated (670 nm) windows are glued[2], walls and lids are assembled and electric connections are soldered.

ECDL operation and test

We use a home-built current controller for the laser current control and a home-built temperature controller for temperature stabilization. The current controller design follows Hall design [9] with some modification to output up to 200 mA. The typical operation current is between 100 and 110 mA. The temperature controller is a home-built one using PID control and Whitstone bridge similar to the generic design [9], and additional filters. We obtained a wavelength close to 670 nm when the temperature setting is around 50°C.

When operating an ECDL the three most important things are 1)operating at the right wavelength 2) operating at single frequency mode (no mode-hop) and 3) staying frequency-locked. To find conditions where the laser is at the right wavelength without mode-hopping, there are four variables: 1) grating angle adjustment by a mirror mount knobs, 2) ambient temperature set by TEC, 3) laser current, and 4)a voltage applied to a piezoelectric actuator. There is no simple formula but the optimal parameters can be found by iterative adjustment of above parameters. To begin with, it helps when the wavelength and power are measured as a rough function of temperature when there is no grating feedback, then one can start with a temperature where about 2 nm or less lower than the desired wavelength; this can benefit in a several way. The free-running laser power output sharply decreases at high temperature, so operating at lower temperature can increase the output power and also it makes lifetime of the diode longer. The remaining difference in wavelength can be easily

[1]When designing a tube mount, the hole is tight on the tube for better thermal transfer and mechanical stability.

[2]It is desirable to make the angled window insertion to avoid a window-reflected beam going back into the diode.

covered by the grating feedback. If one starts at the room temperature and try to pull the wavelength by more than 5 nm only by grating alignment, it might not be easy to reach the desired wavelength. When temperature is close enough, by aligning grating one can get close to the desired wavelength (in our case 670.962 nm for ^{7}Li D2 transition). To make sure the feedback is going back to the diode one can use vertical mirror knob and see a flash when feedback is working. The flash-sensitivity of vertical knob is higher than horizontal knob because of diffraction geometry. When vertical degree of freedom is roughly aligned[3], horizontal knob is adjusted to get close to 670.962 nm; by adjusting knobs by hand one can reach to the wavelength with 1/1000 nm accuracy. Lasing wavelength is not a smooth function of grating angle, but rather a stair shape function due to mode-hops. When the wavelength jumps far from around the desired value, one can test with different diode current and piezo voltage or fine-tuning of ambient temperature. The step size and dynamic range of observed wavelength in single-mode operation[4] are smallest for current adjustment (e.g. For 110 mA operating current, 20 mA change in current can change at best 1/1000 nm or smaller), then piezo voltage (e.g. several 1/1000 nm can be changed within the mode-hop-free range), and then temperature fine-tuning can address several nm to several 1/1000 nm. When the wavelength is close to the target transition (D2 line, ground hyperfine levels), a spectroscopy setup is needed to find a signal to lock the frequency.

4.1.2 Frequency locking with Modulation Transfer Spectroscopy

A stable frequency source can be obtained by locking the laser frequency to a stable reference. An atomic transition is a reliable frequency reference, and thus can be used to lock a laser frequency. Spectroscopy is done in a gaseous sample of atoms by shining a laser beam and scanning its frequency to obtain an absorption profile. In a gas at temperature of 350°C, lithium atoms fly as fast as a few kilometers per second, thus give spectral line broadening by the Doppler effect, which line broadening (a few GHz) is much bigger than lithium ground hyperfine splitting (803 MHz)- therefore, a Doppler-free spectroscopy is necessary. There are numerous techniques for Doppler-free spectroscopy, but basinally they share a common principle called pump-and-probe scheme, in which the two beams interact with the atoms such that the absorption of a probe beam happens only at the sharp resonance for atoms at rest (or at a velocity if the frequencies of pump and probe beams are different). The usual procedure involves a heterodyne detection: mixing a radio frequency with an optical frequency by using frequency modulator such as Acoustic-optic modulator (AOM) or Electro-optic modulator (EOM), detecting the probe beam after passing the gas sample, and demodulating the signal.

We use the modulation transfer spectroscopy technique (MTS, [10, 11, 12]) to generate an error signal to lock the frequency. The biggest advantage of MTS is that it has a background-free dispersive error signal therefore it is in principle immune to the drift of a locking fre-

[3]Note that vertical alignment also affects the wavelength.

[4]A 9 $\sim$ 10 cm long confocal cavity with piezo scanning was built and used to check single-mode operation.

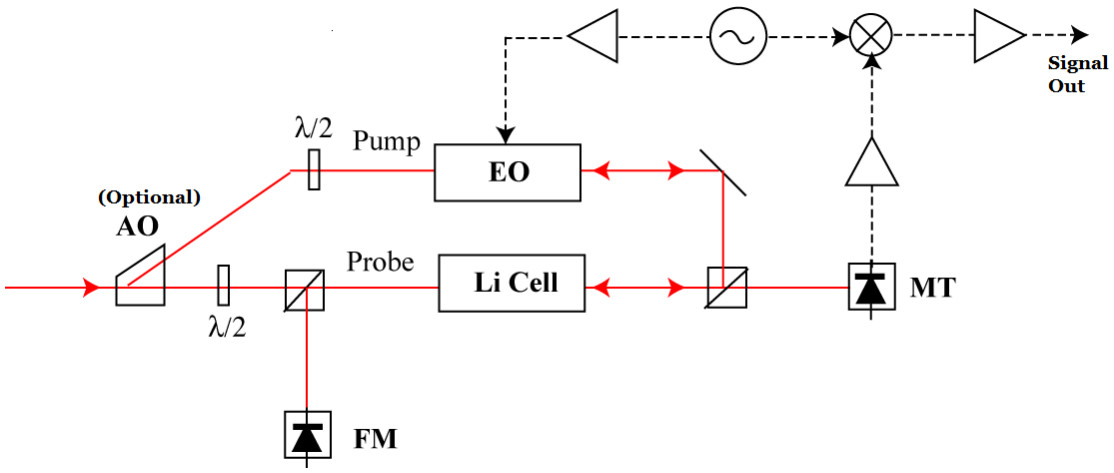

Figure 4.9: Schematics of spectroscopy setup. Modulation transfer (MT) spectroscopy works with modulated pump beam and unmodulated probe beam while frequency modulation (FM) spectroscopy has the opposite configuration. MTS has zero background while FMS doesn't.

quency due to the background (reference level) fluctuation. Figure 4.9 shows a schematic of the modulation transfer spectroscopy setup. A laser beam is split into two, the pump beam passes through an electro-optic modulator (EOM), and then passes through vapor cell. The probe beam, passes through the vapor cell directly, and interact with atoms which also interact with the pump beam. Pump beam, after the EO has a carrier ($n = 0$), the first-order sidebands ($n = \pm 1$), whose frequencies are higher and lower, respectively, by the EO modulation frequency ($\sim$13 MHz in our setup) from the carrier frequency, and other higher-order sidebands ($|n| \geq 2$). The amplitude of a n-th order sideband electric field is proportional to the Bessel function of n-th order, which means the energy carried in higher order components are negligible compared to the carrier and the first sidebands. Also this relation on the amplitudes shows an important result that the +1 order and -1 order sidebands phases differ by π. The two sideband components cancel when the beam interacts linearly with atoms or when no interaction, and only the non-linear interaction contributes the signal. The non-linear effect is known as four-wave mixing and it happens only when sub-Doppler resonance conditions are met, therefore it eliminates Doppler background on the signal. The resulting signal is in dispersive shape, has a zero-crossing on a resonance, and it is largest for the closed transition. One can control the dispersive signal shape by tuning the EO modulation frequency.

Unlike cesium or rubidium vapor cells, a vapor cell of lithium is not commercially available, and requires heating. As discussed in section 2.1, lithium has very low vapor pressure at room temperature therefore high temperature is needed to have sufficient pressure for the spectroscopy cell. Also lithium has a light mass that atoms in the cell move with high speed and stick to the window easily. To prevent the window being coated with lithium, the vapor

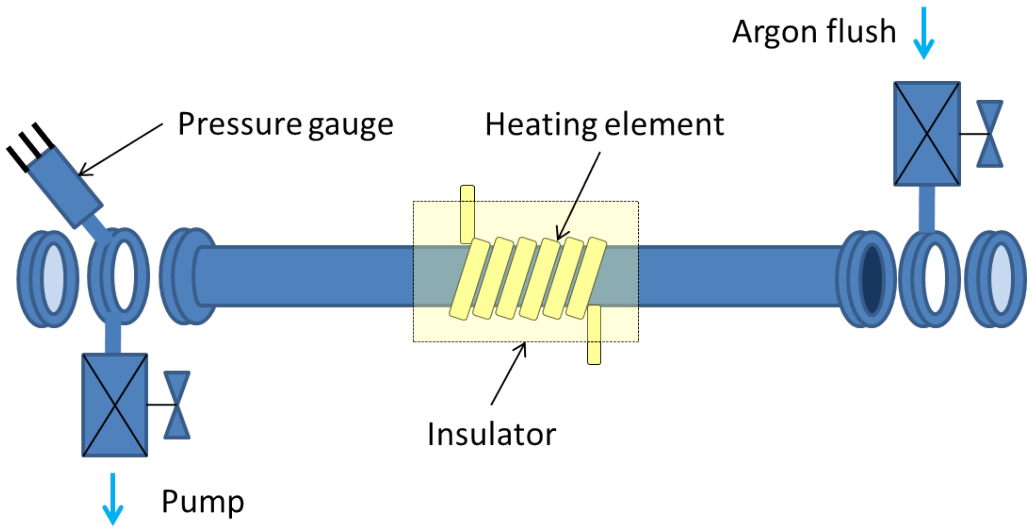

Figure 4.10: Spectroscopy cell

cell is long and filled with buffer gas argon[5] to reduce the mean free path of hot lithium. As shown in Fig.4.10 we use 60 cm 1.33″ CF pipe with two 670 nm AR-coated windows at both ends. Between one window and the tube flange, there is a thin double-sided flange with an adapter connecting to a valve, the other side, there is one with a thermocouple gauge and an adapter connected to a valve. The cell is leveled and mounted about 10 cm above the table, except the pump-side window, the other window and flanges are closed with copper gaskets (or silver-plated copper gaskets for less corrosion)in-between. Lithium chunk in mineral oil is cut in a size about 0.5″ diameter and 1/4″ thickness[6], and washed in pentane followed by washing in methanol. Lithium chunk starts being oxidized as soon as the oil is removed in solvent and it starts forming white lithium hydroxide powder layer on the chunk surface with a lot of bubbles[7]. The process takes just a few seconds, handling with tweezers and shaking while washing in solvents helps to shake off and remove the white layer. When washing is done the lithium chunk is moved quickly into the cell pipe while the pipe is flushed with argon gas. Argon gas flux should be moderate such that it does not blow away the lithium. When the lithium is positioned in the right middle of the pipe, the pump-side window is closed and tightened while argon gas flush is still through the pump-side valve. Argon input valve is closed and a roughing pump[8] is on, thermocouple gauge measures the pressure until it doesn't go down any more. If there is no leak, it takes just few minutes. The pump-side

[5]One should not use nitrogen for buffer gas since lithium and nitrogen can form a chemical compound such as lithium nitride at high temperature.

[6]One should not cut it too thick since it can block the space for the laser beam especially when the pipe is narrow.

[7]One should be careful not to inhale the hydroxide fume from the bubbles. It is a strong base in a moist condition and can irritate respiratory tract if inhaled.

[8]Our pump is 35 L/min dry scroll pump.

valve is closed with the pump still on, and argon input valve opens and fills the argon gas in the cell until the gauge reads atmospheric pressure. The pump valve is on and argon valve is closed and pump out the cell, and the pump-out and argon-fill process is repeated a few times to remove residual gases (such as oxygen, moisture and dust) inside the cell. In the end the argon pressure is kept about 100∼200 mTorr. The middle part of the pipe is wrapped with a heating tape or heating element such as a ni-chrome wire with insulating sleeve. To avoid magnetic field forming inside the cell due to solenoid-shaped current flow, one can wrap the resistive heating wires in one direction for one layer and the opposite direction for the next layer. It is very important to wrap only small part (about 4 inch wide is sufficient) in the middle of the pipe to keep the rest of the pipe wall cold[9]. The heating tapes are connected to the power supply, we monitor the cell temperature with a thermocouple temperature sensor directly attached to the heated part of the cell and keep the temperature at about 350^oC. During the initial settling period, the inside pressure get higher due to out-gasing after a few days then we pump out and fill argon gas a few times to remove dust (or undesired gas and chemical compounds). After a few iteration of pump-out and flush, we did not have to replace lithium for more than 3 years[10]. When optical setup is ready, total about 3 mW of beam power is used in the spectroscopy setup, after all optics such as EO, wave plates and cubes, only 0.5 mW or less per each beam path is enough for the beam power just before the cell[11]. The beam waist is about 1.4 mm. Overlapping of the two beam paths (pump beam and probe beam) is roughly done and the laser frequency is scanned by sweeping the piezo voltage around the desired frequency (670.961 nm for ^{7}Li D2). One can detect a change in power due to absorption when it hits the resonance either by a photo detector or by bare eyes (if scanning frequency is as low as a couple of Hertz). Fig.4.11 shows the resulting absorption spectra and dispersive signal due to MTS for ^{7}Li D2 transition. The other port looking at the pump beam (labeled as FM in Fig.4.9) gives another dispersive signal larger than MTS signal which is just frequency modulation spectroscopy (FM). However the resulting signal from FM port does not have the advantage of MTS (no background) because the four-wave mixing condition is not met.

We use the ground hyperfine crossover line for our reference frequency. Crossover signal appears when the two real spectroscopy lines are within the Doppler background which is about a few GHz for hot lithium. Whereas the real lines is due to atoms at rest(provided that the pump and the probe have the same carrier frequency and not shifted from each other), the crossover is a result of some atoms whose velocity thus corresponding Doppler frequency happens to be the exactly middle between two real lines and see the resonance by the Doppler effect. We adjust EO modulation frequency and beam alignment to make the crossover signal look straight and symmetric around zero and lock the frequency using a

[9]Otherwise, the lithium will stick to the window.

[10]In some literatures a fine metal mesh is placed inside the cell to recycle lithium droplets on the wall by sucking them back to the center with capillary action. We did not use a recycling method but the lithium chunk stays plenty in the cell.

[11]About 0.2 to 0.3 mW of absorption was observed on resonance.

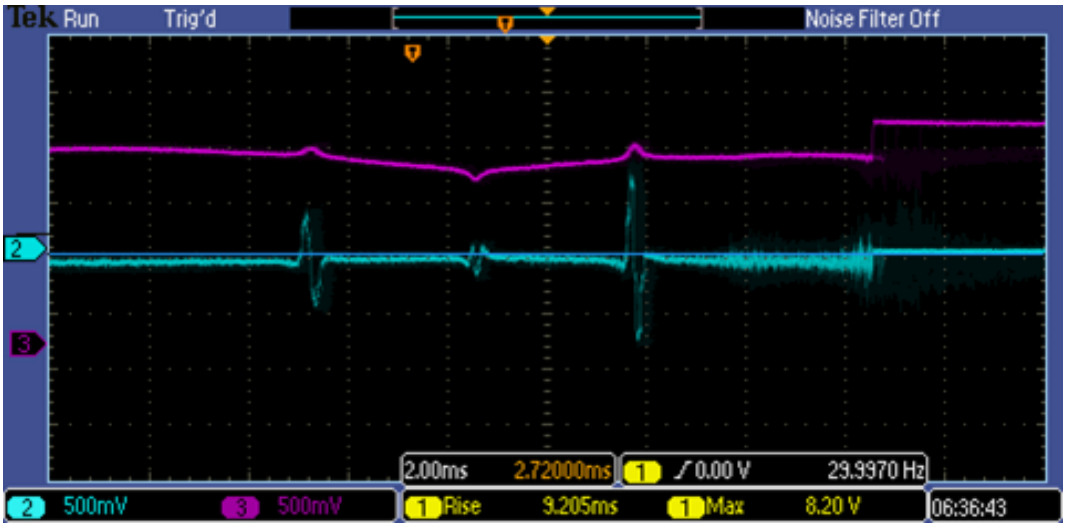

Figure 4.11: Spectroscopy signal of ^{7}Li D2. MTS output after demodulation- blue, absorption signal- purple. The absorption signal has a huge background while the MTS signal has no background. The step on the right side is a typical sign of a mode-hop, and can be moved away by adjusting diode current and piezo voltage.

home-built feedback circuit (Fig.4.12). The locking circuit consists of a Shmitt trigger which internally generates ramp and PI feedback loops for diode current and piezo. The internal ramp sweeps the diode current to scan the frequency[12]. When the ramp is reduced and the lock gain is increased the zero-crossing point of the spectroscopy signal (or also called the error signal) is fixed as a locking point. Proportional and integrator gains are set such that the lock does not oscillate and the error signal stays at zero.

[12]One can also use frequency scanning by piezo. Piezo scanning is convenient when larger scanning range is needed such as searching spectroscopy lines. Current scanning has narrower scanning range, but the current response is fast thus there is no lag between frequency and the ramp whereas a piezo scanning can have a lag.

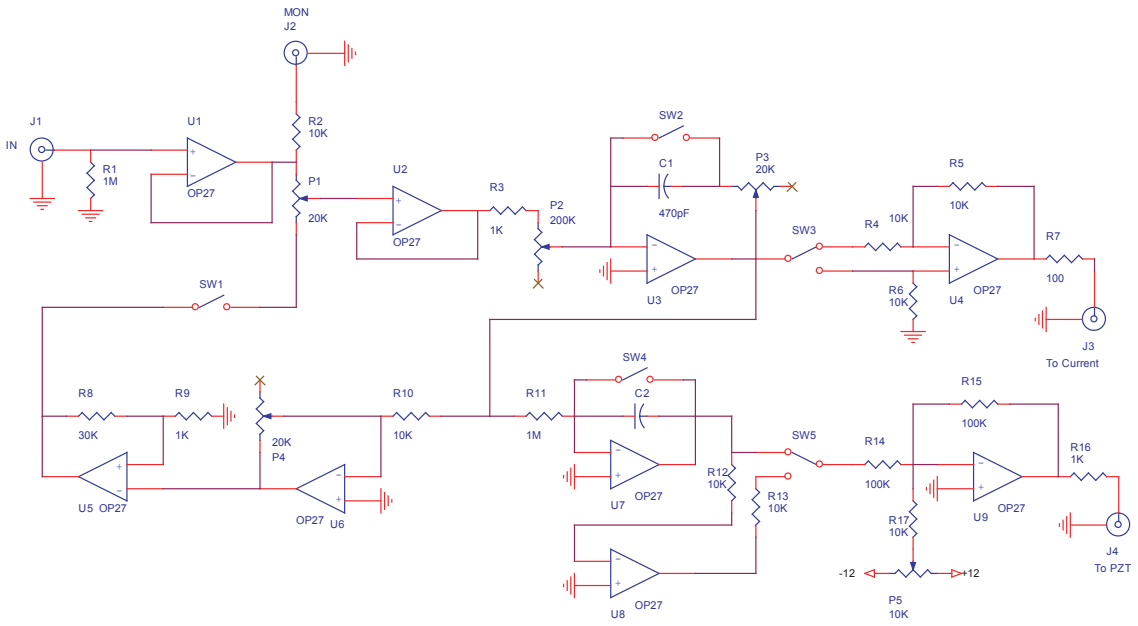

Figure 4.12: Frequency lock feedback circuit

4.1.3 Phase Locking

For lattice cooling experiment we use both blue and red detuning from both D1 and D2, and the detuning ranges from 1 to 10 GHz. We use the home-built ECDL as a lattice cooing laser and is phase locked to the reference beam. The reference beam has a frequency locked to ^{7}Li D2 ground state hyperfine crossover (ECDL1 and Slave1). As shown in the diagram Fig. 4.13, 50:50 non-polarized beam splitter cube overlaps the reference beam and lattice cooling laser beam. The resulting beat signal is detected by a ultra-fast photo detector (Hamamatsu MSM Photodetector G4176). An offset frequency (1-10 GHz) is generated by an RF generator (Agilent Technologies microwave generator for DC to 4 GHz, Vaunix LMS103 for 5 to 10 GHz) and mixed with the beat signal by a mixer (e.g. Minicircuit ZX05-153MH-S+ or similar). The resulting intermediate frequency (frequency difference) from the mixer is amplified and split to two arms. One goes to a mixer, and is mixed with 30 MHz function generator signal[13]. The difference goes to a direct frequency feedback to the current via a bias tee. The other arm from the first mixer intermediate frequency goes to a digital phase detector. The digital phase detector consists of two ultra-fast comparators which converts RF sine wave into digital rectangular pulses and an ultra-fast phase/frequency discriminator (AD9901) which takes two digital pulses as input and generate an error signal

[13]This frequency is a small offset to provide a lock point other than DC; therefore it does not have to be 30 MHz.

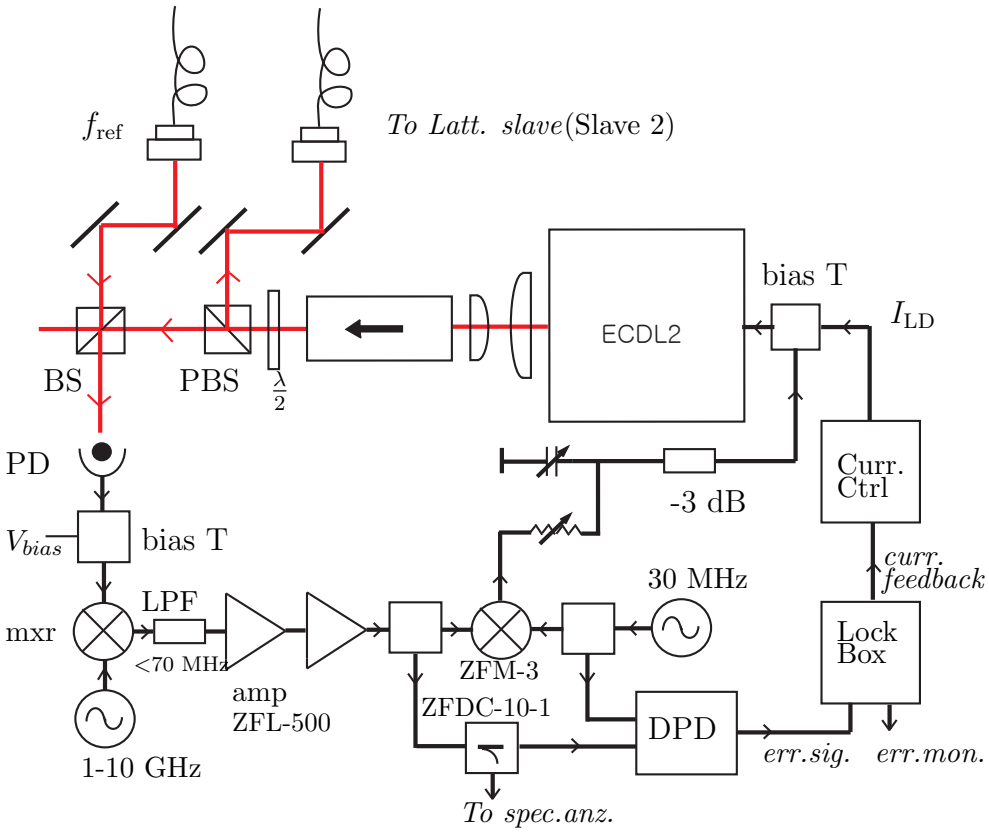

Figure 4.13: Schematics of phase lock setup

via XOR gate. Effectively it compares phase and frequency of the two inputs and generate a phase error signal. The error signal goes into a lock box and generate current feedback through the current controller. All cables and connections are kept short and fastened, and there is a feedback bypasses the digital box to keep the feedback loop fast.

4.1.4 Slave laser and Tapered-Amplifiers

Slave lasers

Slave lasers use the same type of laser (Fabry-Perot) diode as ECDL. In a Fabry-Perot diode, the waveguide is rectangular shape. When it has a narrow waveguide to excite only the fundamental gaussian mode it has a desirable feature as single-mode operation. The use of slave laser and its working mechanism is simple: A slave laser is used to amplify a weak stable reference laser beam which frequency is well-defined. The reference beam works as a seed beam and is injected into the laser diode. When these injected photons dominate than other frequency modes in the resonator, the seed beam gets amplified. The maximum power of commercially available laser diodes are all different for different wavelengths, but for many

visible and IR wavelengths more than 100 mW is available. For single-mode 670 nm laser diode the maximum power commercially available is less than 20 mW, however fortunately there are 120 mW laser diodes at 660 nm. We used ML101J27 (Mitsubishi, 660 nm, 120 mW, single-mode)[14], and heated to $60 - 70°$C. For thermal stability, two lasers of boxes are used to enclose the laser (Fig. 4.14). The inner box is made of black Delrin plastic for better thermal isolation. All inner box and outer box walls are separable for easier access. The laser diode is mounted on the typical f=4.5 mm collimation tube and the tube holder. Right underneath of the tube holder there is TEC for heating, and between the two, indium foil is used for better thermal conduction and for preventing thermal paste evaporation at high temperature[15]. Then the assembly is enclosed with a box made of black delrin material for better thermal isolation. All box walls are separable thus it makes easier part replacement and adjustment. The front face has AR-coated window for laser beam output. On the back wall there is a laser diode protection circuit. The bottom wall has rectangular hole for TEC. Outside enclosure is a box and a base made of aluminum. The outer box also has separable walls for easy access to the inner parts. Compared to a thin single layer enclosure, the laser injection locking stayed much more stable for double box design (e.g., it locks for through out a day unless the seed beam is disturbed).

[14]Obsolete and has been replaced by HL6545MG.

[15]We observed coating on the window of inner box and it was from thermal paste evaporation.

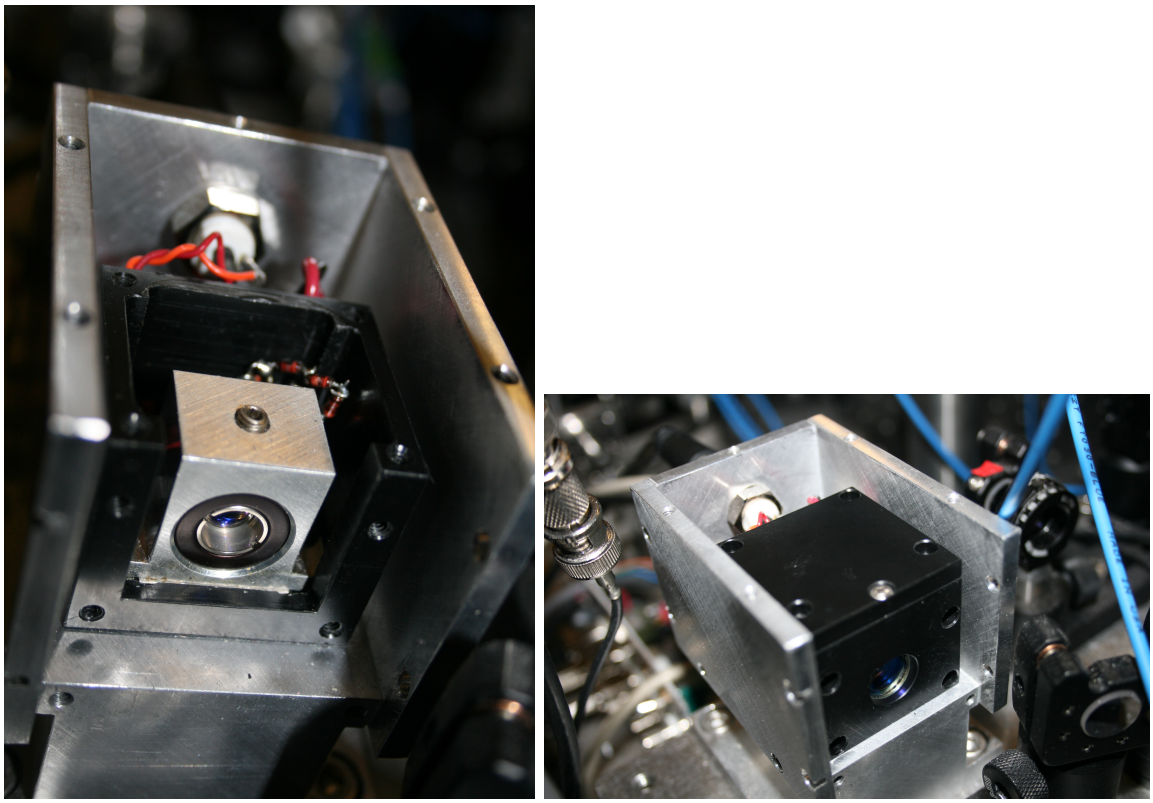

Figure 4.14: Slave laser. The lid and front wall are temporarily taken out for showing.

Tapered Amplifiers

A laser diodes used for master laser or slave laser has typically low power (less than 200 mW) but a good beam quality- e.g. single mode Gaussian spatial mode. It has narrow waveguide to allow single transverse mode therefore has a small emitting area which leads large divergence. Nevertheless its large beam divergence it is diffraction limited and the beam quality stays good. A broad-area laser diode, on the other hand, has one or two hundreds micron sized broad emitting strip; the waveguide has larger volume in its active area thus it can emit a larger power up to a few Watt. However, its broad area waveguide has multiple spatial mode therefore the beam quality is poor. Tapered amplifier combines the advantage of both. It has a straight narrow waveguide at the back which serves as a modal filter, and a tapered section in the front. The tapered section keeps the energy density below a critical value, above which the energy density is too high and the material can be destroyed by a self-focusing effect. The resulting output beam is as powerful as broad area laser and the beam quality is better, yet not Gaussian. Fig. 4.15 shows comparison of beam profile for narrow waveguide laser, broad area laser, and tapered amplifier.

We use three tapered amplifiers to generate 2D MOT, 3D MOT, and a lattice beam. Tapered

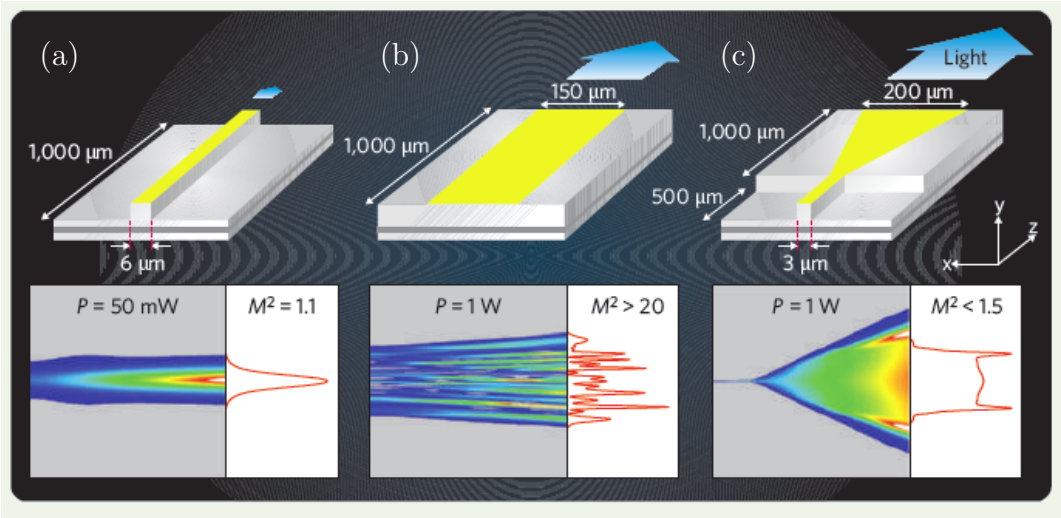

Figure 4.15: Beam profile comparison.(a)narrow waveguide (ridge waveguide),(b)broad area, and (c) tapered amplifier. Image is adapted from [14].

amplifiers that generate 2D MOT and 3D MOT are commercial lasers from TOPTICA (BoosTA for 2D and DLPro for 3D), and the lattice TA is home built. 670 nm commercial tapered amplifiers have been less available compared to other popular wavelengths for alkali atoms such as 850, 760 and 780 nm. A packaged tapered amplifier unit excluding a master laser would cost more than 25k USD. However the TA chip became available in the market recently under 1000 USD per piece therefore we built our own TA. Current available 670 nm tampered amplifier chip specs 500 mW for maximum power and 1 W chip may be available in the future (in comparison, other alkali wavelength TA chips are available for more than 1W). We use Eagleyard 670 nm 500 mW chip (EYP-TAP-0670-00500) on a C-mount. Fig. 4.17 shows our home-built tapered amplifier using the 500 mW 670 nm TA chip. The inside of TA (Fig. 4.16) consists of (a) a base, (b) a heat sink that has a holding place for the chip. The front and the back side of the chip, there are collimation lenses for output beam collimation (front, f=3.1 mm) and seed beam collimation (back, f=4.5 mm). Between the heat sink and the base, there is a TEC with cold face upward (facing the heat sink), and thermal paste on the surfaces. The chip C-mount sits on a heat sink with an indium foil in-between for better thermal conduction. The TA diode current runs from the c-mount body to the cathode tail and electric connections with a protection circuit attached.

The output facet of a TA chip is wide (hundreds μm) and thin (a few μm), the output beam diverges faster in vertical axis than the horizontal axis. The primary role of a short focal length aspheric lens for collimation is to collimate the vertical axis, not to collimate both axes at once. The beam shape after the front (output side) collimation lens is vertically collimated yet still diverging in horizontal direction; horizontal axis is collimated by a cylindrical lens pair outside the TA box. Since the collimation lens focal length is short, the output beam

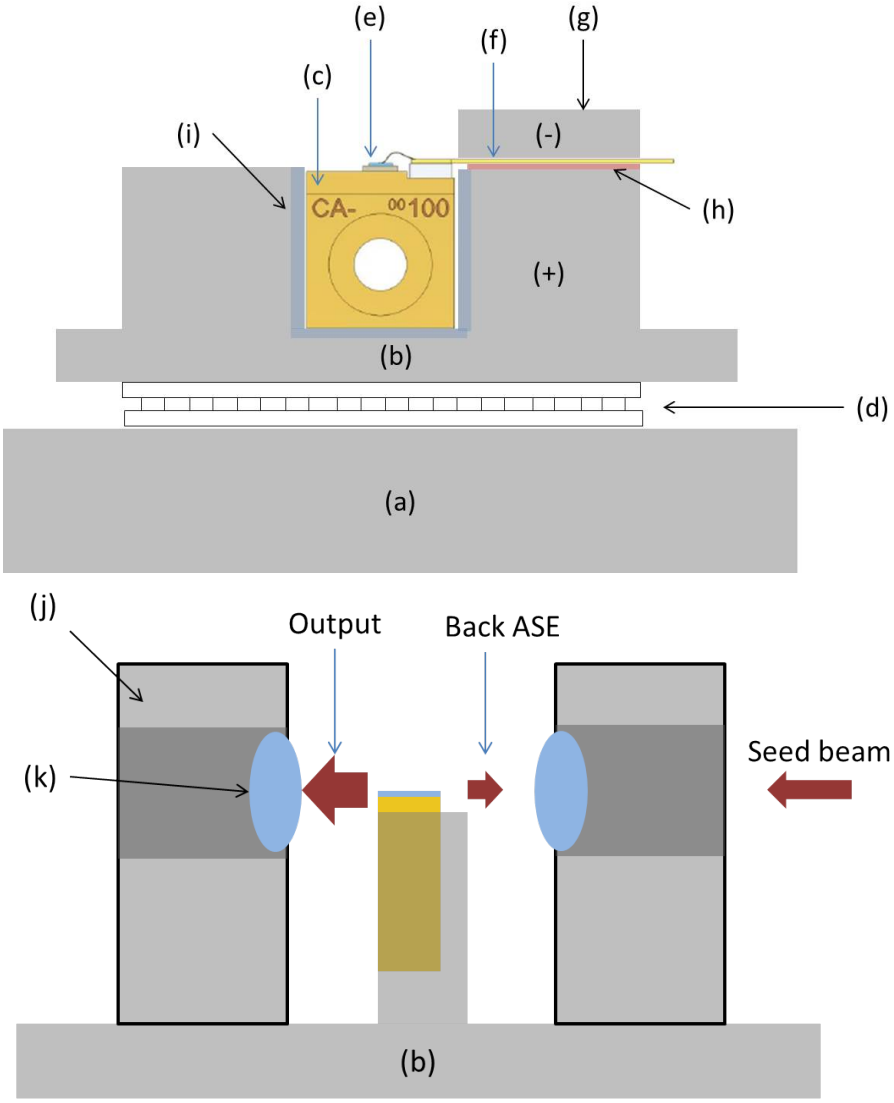

Figure 4.16: A tampered amplifier assembly. Upper: front view, Lower: side view. (a) base, (b) heat sink with chip holder, (c) TA chip (C-mount packaged), (d) TEC, (e) diode output facet, (f) electrode (cathode), (g) cathode connecting block, (h) insulating tape, (i) indium foil, (j) lens mount, (k) collimation lens.

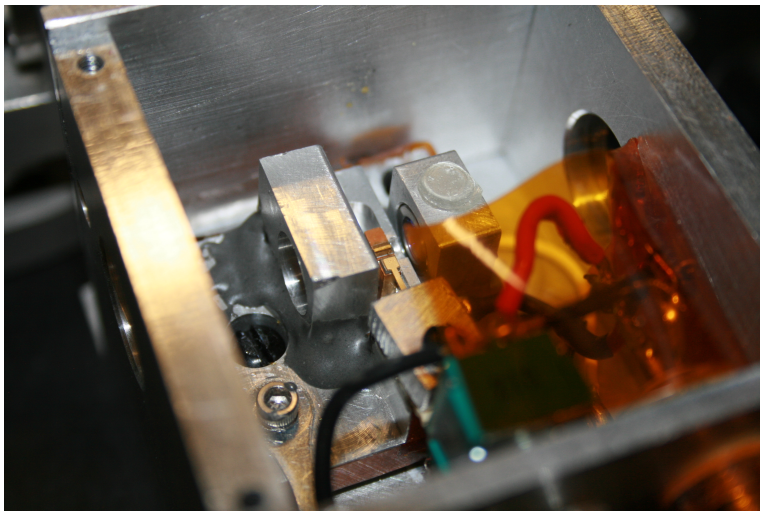

Figure 4.17: Inside of a tapered amplifier.

shape is very sensitive to its position and angle- a precision adjustment can be done by using a 3D translator. After the lenses are aligned, lens mounts are glued using JB-weld. During the collimation it is important to operate the TA in a low current since a TA chip degrades or can be damaged if it runs without a seed beam for long time[16]. The light coming out when there is no seed beam (no lasing) is called amplified spontaneous emission (ASE) and comes out both to the front and the back. At the max operating current (1 A) the front ASE without a seed beam is about 18 mW while with a 10 mW seed beam at the same current the output power from the TA exceeds 500 mW. We typically run the TA at 15 mW seed beam and 800 mA which output beam power is 480 mW (when measured before an isolator).

4.2 Laser system overview

Our laser system (Fig.4.19) consists of 1) spectroscopy and frequency locking setup, 2) frequency shifting setup for generating 3D and 2D MOT, and imaging frequencies (Fig. 4.20), and 3) cooling lattice phase lock setup. Except the cooling lattice laser which frequency lies between ^{7}Li D1 and D2 transitions, and requires a large frequency tuning range, all other laser frequencies are in D2 transition. Especially 2D MOT and 3D MOT beams need two frequencies: cooling (trapping) and repumping beams (Fig. 4.18).

In the spectroscopy setup, the grating laser labeled as ECDL1 in Fig.4.19 is a commercial grating laser (TOPTICA DL Pro, 670 nm) which beam path has been modified to send the full laser beam power (about 10 mW after a double stage faraday isolator) from ECDL1 to

[16]This is because the injected charges recombine without radiation thus the released energy heats up the diode and can damage.

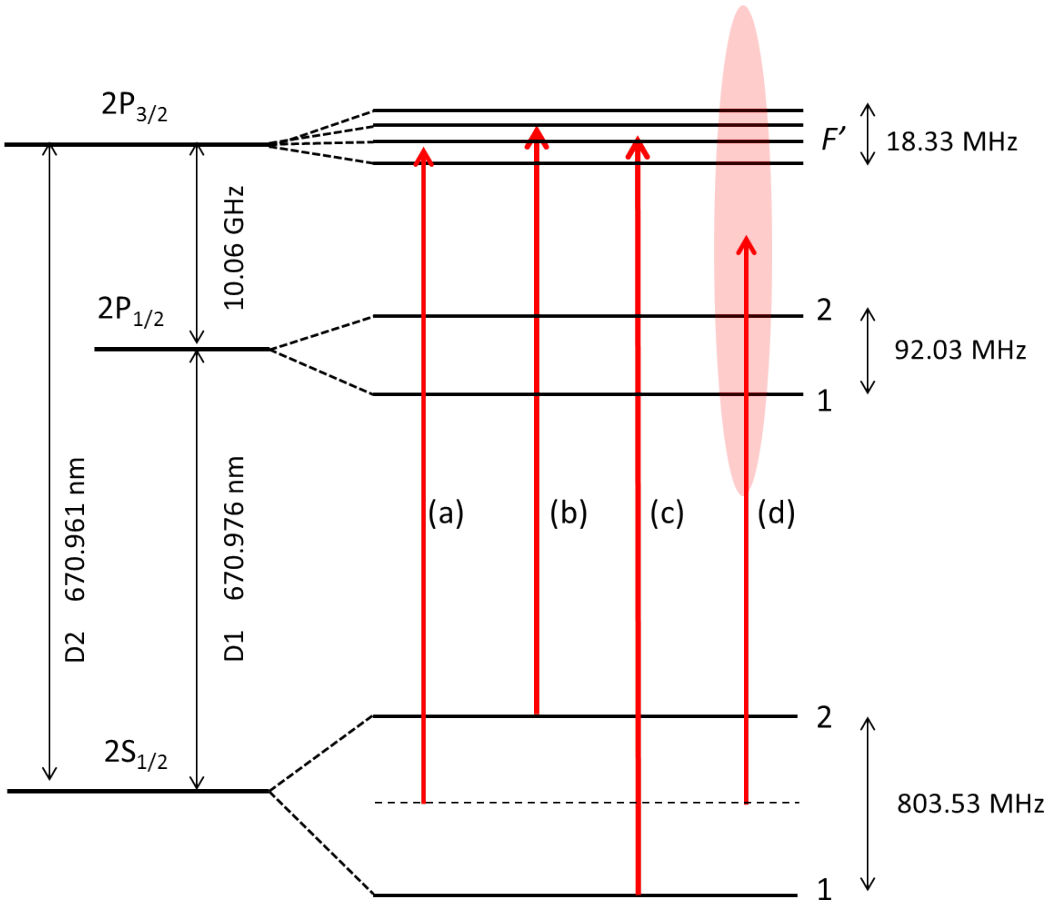

Figure 4.18: ^{7}Li energy level and laser frequencies. (a) master laser reference frequency, (b) 2D and 3D MOT trap frequency, (c)2D and 3D MOT repump frequency, (d) lattice cooling beam frequency. A dotted line between the ground hyperfine levels is the crossover between the two.

the spectroscopy setup, monitoring cavity, and seed beam for slave laser (labeled as slave1) instead of seeding the tapered amplifer of the DL Pro. The spectroscopy setup has an electro-optic-modulator for modulation transfer spectroscopy (MTS) and a heat-pipe lithium cell heated at about 350°C. The demodulated voltage signal from MTS setup is used to lock the frequency of ECDL1 at ^{7}Li D2 transition ground hyperfine crossover using laser diode current and piezo voltage feedback.

Slave1 is a home-built laser and is injection locked to ECDL1. Slave1 uses Mitsubishi 660 nm laser diode (ML101J27) and can output 90 mW after the isolator when it is heated at about 70°C. The output of the slave is split into seven paths using polarization beam splitting (PBS) cubes; one of them is fiber coupled and goes to the cooling lattice laser setup to be

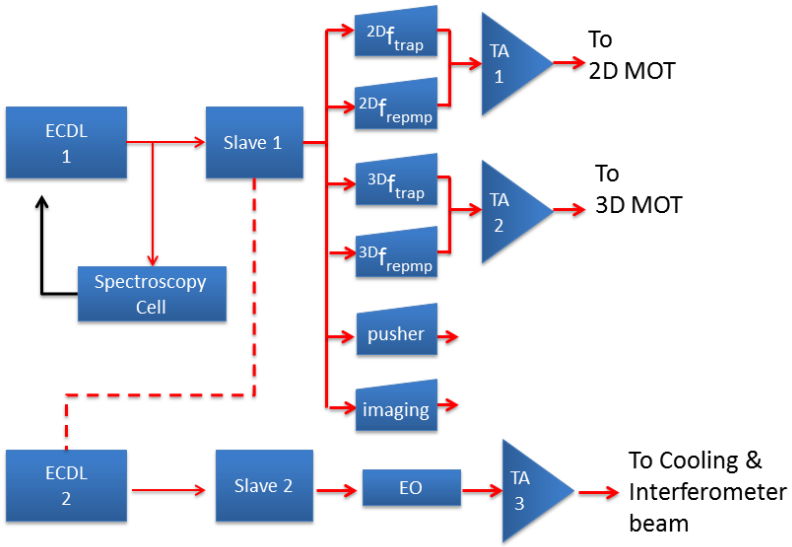

Figure 4.19: Schematic diagram of the laser system

used as a reference beam, and the rest go through double pass AOs to generate frequencies required for trapping and repumping in 2D and 3D MOT, and pusher and imaging beam. The frequency shifting AOs are controlled by voltage controlled oscillators (VCOs), and are about 400 MHz shifted up from the crossover for 2D and 3D MOT repumping frequencies, and 400 MHz down-shifted for 2D and 3D MOT trapping frequencies, imaging and pusher beam frequencies. More details about their detuning will be discussed in section 4.4. After passing double pass AOs, for each 3D and 2D MOT, trap and repump beam frequencies are combined in PBS cubes making trap and repump beams overlapped with polarization orthogonal to each other. Then the combined beam is fiber coupled and is seeded to each TAs. Seed beam powers after the fibers are typically 7 mW (4 mW for trap and 3 mW for repump) for 2D MOT TA and 4.5 mW (2.5 mW for trap and 2 mW for repump) for 3D MOT TA. As a result, 2D MOT beam power after a high power single stage faraday isolator is 200 mW or more, 3D MOT beam power after isolator is about 285 mW. Both TAs are spec-ed to give maximum 500 mW, however due to low seed beam power their output powers are only 200∼300 mW. 180 mW of power remains after shutters and other optics before the MOT setup, and goes to 2D MOT setup in free space. About 260 mW for 3D MOT beam after the shutter is fiber coupled and split into six fiber ends and are delivered to 3D MOT beam expanders, each output beam after the fiber is about 5 mW.

Part of beam from slave1 sent to cooling beam lattice setup is used as a reference beam, and

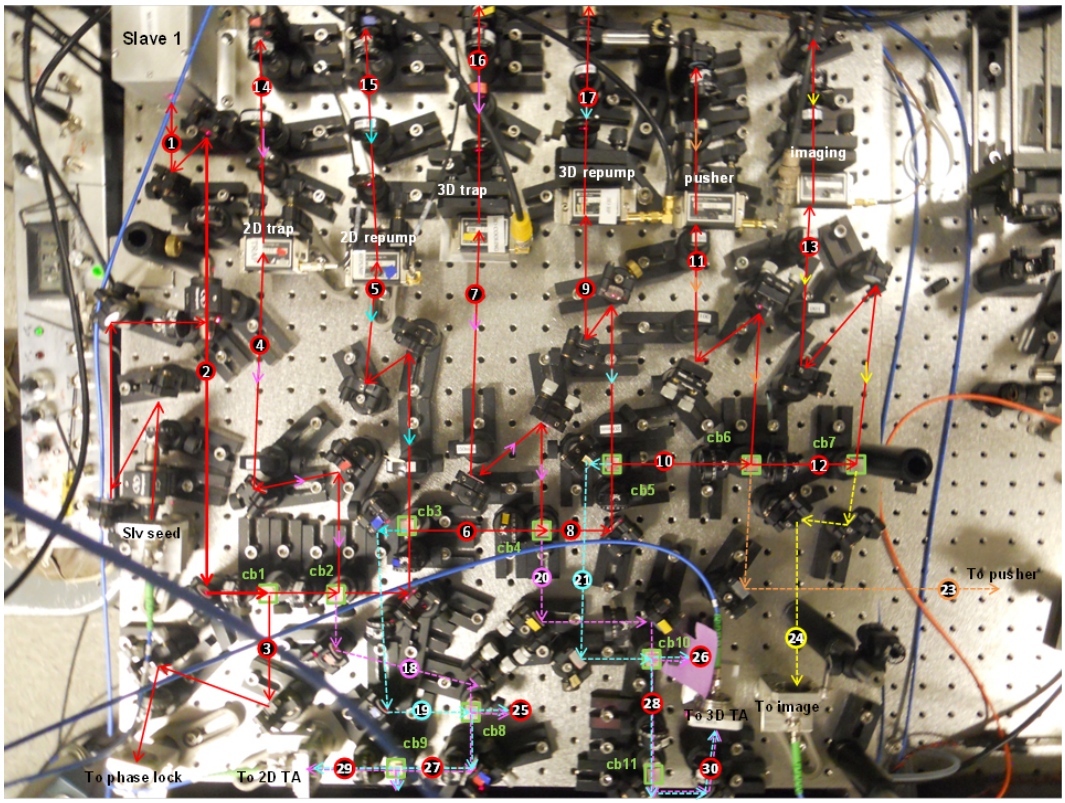

Figure 4.20: Frequency shifting setup for MOT frequencies

is overlapped with a beam from a home-built grating laser, ECDL2 at one of the arms of a non-polarizing beam splitting cube, and the resulting beating signal is detected by a detector (Hamamatsu MSM G4176[17]). The beating signal is modulated and demodulated by a RF frequency (1 to 10 GHz) and a phase lock circuit gives a current (and also piezo) feedback to ECDL2 to lock the laser's frequency to ECDL1's frequency with a few GHz detuning given by the RF frequency. Part of beam from ECDL2 is fiber coupled and get injected into a slave laser (Slave2). The output light passes through an EO which modulation is off for the lattice cooling stage and on for Raman interferometer stage. The beam is them fiber coupled to a home-build tapered amplifier (TA3). TA3 produces 410 mW after an isolator when 16 mW is seeded. After passing an AOM the power in the first order beam is 250 mW. After filtering polarization using a PBS, the lattice beam is fiber coupled to give an output power of 110-140 mW maximum.

[17]metal-semiconductor-metal GaAs fast photodiode. Its rise time is 30 ps therefore it gives about 10 GHz bandwidth.

4.3 Vacuum system

4.3.1 Vacuum system design

Vacuum setup consists with oven, 2D MOT chamber, differential pumping tube, 3D MOT chamber, various vacuum pumps and vacuum gauges(Fig. 4.21). Oven is custom designed and made with standard vacuum parts welded together. Its bottom is a 1.5″ diameter 1.5″ height cylinder with a closed bottom and a top with welded 1.33″ CF flange facing upward. The material is 304 stainless steel except the flange part. The oven flange is made of 316LN stainless steel which is harder and corrosion resistant. Since lithium is highly reactive on copper gasket[18], a nickel gasket is used for oven flange- a knife edge made of 316 stainless steel works better for nickel(harder than copper) plus it is more corrosion resistant.

2D MOT chamber is made of a six-way cross (2-3/4″ CFF, 304 SST) and a 1.33″ CF flange (316LN SST) welded on to the cross for oven connection. The 1.33″ flange is at 45^o angle between two arms of the 6-way cross (Fig.4.22) and the pipe is about 2.5″ long from the welding joint. 5 view ports AR-coated at 670 nm are used on front and four side arms of the cross. As shown in side view of Fig.4.22, the back side arm of the 6-way cross connects to flange cross adapter and to a differential pumping stage then to a gate valve. A flange cross between 6-way cross and the differential pumping stage connects to an ion gauge, an all-metal valve and a turbo pump to pump 2D MOT chamber efficiently during baking. The turbo is detachable from the all-metal valve[19] after baking. The differential pumping stage is made of a 1/4″ OD (inner diameter is about 4.5 mm) 6″ long stainless steel tube welded onto a double sided CF flange with 1/4″ thru-hole. Compared to a thin and short skimmer design in [13], our 4.5 mm ID 15 cm long skimmer offers easier pusher beam alignment and easier construction without compromising its performance. With 40 L/s ion pump attached on 3D MOT chamber, the 2D to 3D chamber pressure ratio by the differential pumping skimmer is more than 500:1[20] which suggests that the 3D MOT chamber can be safely at UHV level even though 2D MOT vacuum is about micro Torr level (very unlikely to be worse than that). A gate valve between DP and 3D MOT chamber is normally open for MOT operation but is very useful when breaking vacuum or baking separately. 3D MOT chamber is an 8″ spherical octagon chamber. 2 large view ports (8″, Non AR-coated) and 6 small view ports (2-3/4″, AR-coated) are used for beam access windows. One of the small ports on the horizontal axis connects to 2D MOT chamber, and the other one is connected to flange crosses connecting to a Titanium sublimation pump (TSP), a detachable turbo pump with all-metal gate valve, an ion pump (40 L/s, StarCell, Varian), and an ion gauge.

[18]It is severer for an oven than a vapor cell because in oven it is high flux and liquid phase can form on the walls and joints inside the oven.

[19]All-metal valve has better vacuum isolation than gate valve thus suitable isolating UHV from atmosphere, plus it has high bake-out temperature $\sim 450^o$C.

[20]By the vacuum standard, conductance calculation is based on dry air at RT. Formula is for molecular flow regime, and circular cross-section tube.

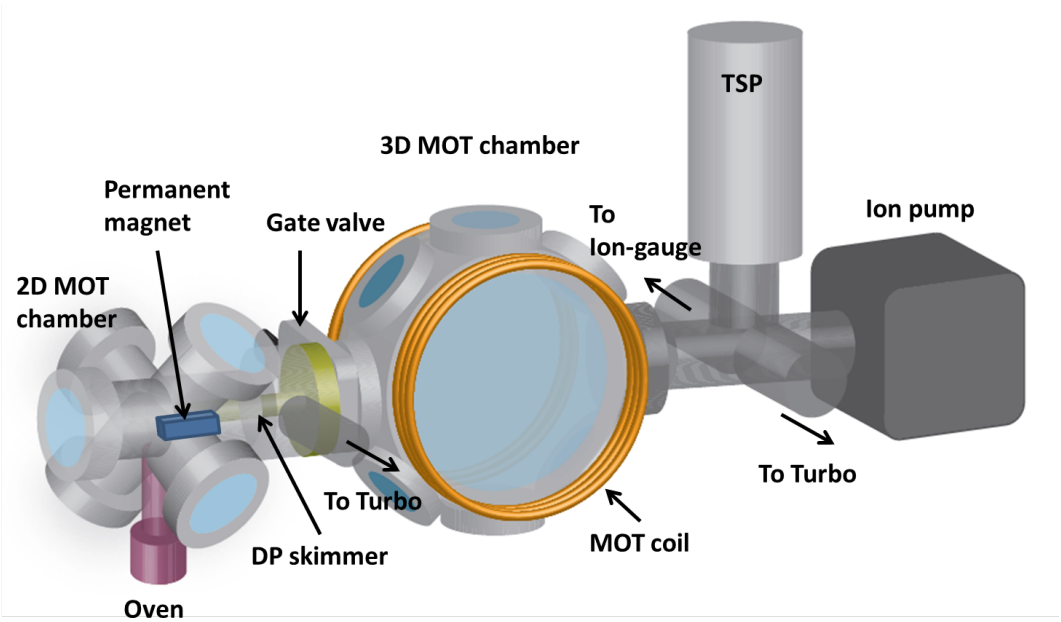

Figure 4.21: Vacuum setup

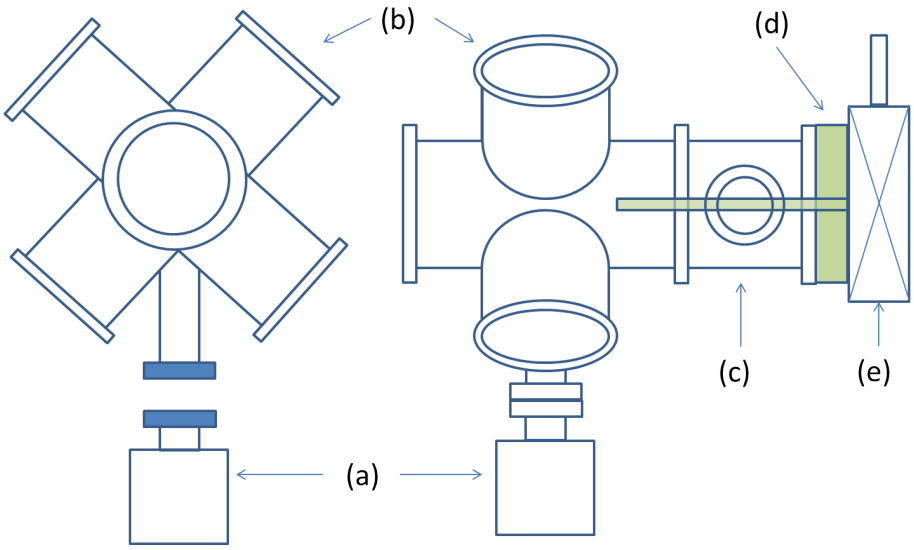

Figure 4.22: Left: Front view of 2D MOT chamber and oven. Shaded flanges (blue) are 316 LN stainless steel and a nickel gasket is used between them for sealing. Right: side view of 2D MOT chamber assembly. (a) oven, (b) 2D MOT chamber, (c) flange cross for pump access, (d) differential pumping skimmer (shaded green), (e) gate valve.

4.3.2 Atom preparation

Lithium purum has residual hydrogen compound produced during the manufacture process, and baking at 600^{o}C can get rid of the hydrogen compound residual. Since the high baking temperature will produce high flux of lithium, pre-baking at a separate chamber is needed. We put natural abundance purified lithium granules in argon seal into our oven in argon atmosphere[21]. Then the oven is assembled with an adapter followed by right angle elbow, and a valve inside the argon filled glove box. Between the oven flange and the adapter flange, nickel gasket is used and silver plated (or anti-seize grease can be used) bolts and nut plates are used to prevent jamming after the bake-out. After oven assembly in argon atmosphere, with valve closed, the oven assembly is taken out of the globe box and assembled with a metal bellow, and a turbo pump, connected to a roughing pump and a thermocouple gauge. The oven is wrapped with heating tape, a thermometer, and thermal insulating material. Roughing pump is on with the oven-side valve still closed to get rid of air in the bellow and the turbo. Turbo is on when the roughing gauge reads below 0.1 mTorr or at equilibrium by roughing. When air is pumped out then the valve is slowly open to evacuate argon in the oven[22]. Bake-out starts, oven temperature is increased slowly to 600^{o}C, kept baking for 2+ hours. Oven and the joints near oven are wrapped with thermal insulation to make smooth thermal gradient but other parts are kept cold to prevent hot lithium atoms bouncing and arriving to the turbo. Elbow or tee on top of the oven blocks most of high flux lithium turning them into liquid[23], drop or slide back into the oven. After baking is done and all parts are cooled down the valve is closed and pumps are closed, bellow is detached from the valve. 2D MOT chamber parts are sonicator-cleaned and assembled. A gate valve is at the end of differential pumping skimmer flange. 2D MOT chamber and oven are connected inside the argon atmosphere glove box with a new nickel gasket in between. After assembly is done and the gate valve closed, the 2D MOT with oven assembly is taken out from the glove box and pumped out with a turbo as much as it can to remove argon (likely also residual air) in the 2D MOT chamber. 3D MOT chamber parts are cleaned and assembled[24], connected with 2D MOT chamber with the valve kept closed. 3D chamber is pumped out with a turbo pump attached to 3D MOT chamber. Heating tapes are wrapped evenly without crossing each other to avoid a hot spot. View ports are protected with UHV aluminum foils before wrapping heating tapes to prevent too high temperature at the windows. With pumping with turbo pumps on both 2D and 3D MOT chamber, the heaters turn on and baking starts. While baking we keep monitoring temperatures and control heaters such that 3D MOT chamber temperature is about 300^{o}C, 2D MOT chamber is above 200^{o}C, windows at

[21] We used an argon filled glove box for convenience and better controlled environment however glove bag with argon flush also works.

[22] Since the argon gas in oven and parts before valve is at atmospheric pressure (although the volume itself is small compared to the rest), the valve should open very slowly not to shock the turbo.

[23] Without heating separately, the thermal gradient cam make it still hot- more than 200^{o}C which is enough temperature for lithium to be liquid

[24] When putting the big windows on to the chamber, one should bolt down symmetrically otherwise it is likely to cause a leak problem.

about 100^{o}C, gate valves, ion gauges and ion pump (with magnets taken off) are at about 200^{o}C. After bake-out and things cool down, the 3D MOT chamber pressure is at 10^{-9} Torr or below with the ion pump on.

4.4 MOT setup and cooling lattice setup

The 2D MOT beam is generated from a TA (Toptica, BoosTA) with a total power 250 mW at 7 mW seed beam (cooling beam and repumping beam combined)[25]. After a 4 mm-aperture isolator, shutter and optics, about 190 mW of power goes (via free-space) to the 2D MOT optics setup which includes beam splitting cubes, two telescopes, mirrors and wave plates, resulting ending power of about 50 mW per one 2D MOT axis. One beam through the 2D MOT is retro-reflected using a silver mirror and an 1 inch zero-order $\lambda/4$-wave plate. The beam size ($r_{e^{-2}}$) is 4.5 mm which gives a peak intensity around 150mW/cm^2. The 3D MOT beam takes 5 mW seed beam (both cooling and repumping beam) and is amplified by a TA (Toptica DL Pro) to generate 230 mW. After an isolator and a shutter it is fiber coupled and is split into 6 beam outputs. Each output beam has 5 mW, and is expanded from the fiber tip end to a 2 inch achromatic doublet with f= 150 mm, and gives a beam size of $r_{e^{-2}} = 4.4$ mm (corresponding peak intensity is 16 mW/cm^2. Between the lens and the fiber tip there is a half-inch zero-order quarter wave plate to generate a circular polarization. Pusher beam has a beam size of $r_{e^{-2}} = 1$ mm and power of 250 μW (peak intensity of 16 mWcm^2). It passes through the differential pumping channel to push atoms in the 2D MOT to the 3D MOT chamber, the angle and positioning of the pusher beam is carefully tweaked such that the resonant light does not disturb the atom in 3D MOT. The imaging beam is fiber coupled and expanded from the fiber tip to a lens. It has 2.5 mm beam size and 100 μW beam power, and is sent to the 3D MOT chamber bottom view port and shoots upward. On the top of 3D MOT chamber, there is a CCD camera (PCO pixelfly). The lattice cooling beam has beam size of $r_{e^{-2}} = 0.7$ mm, and beam power of typical maximum at 110 mW after the fiber, frequency ranging between -5 GHz to D1 and $+5$ GHz to D2 line. The lattice cooling beam path is similar and almost parallel to 3D MOT beam. The polarization of the beam is linear, retro-reflected beam polarization is either orthogonal or parallel to the incoming beam ($lin\perp lin$ or $lin\|lin$). Table 4.1 shows the frequency detunings of laser beams for 2D MOT, 3D MOT, pusher, and imaging.

A magnetic field gradient of the 2D MOT is generated by permanent magnets locating at the left and right sides of the 2D MOT (Fig. 4.21) A custom-made aluminum frame firmly attached to the 2D MOT chamber holds those magnets ± 4 cm from the 2D MOT center, generates a magnetic field gradient about 50 G/cm. 3D MOT magnetic field is generated by a water-cooled hollow rectangular magnetic coil. The coil diameter is $15 - 21$ cm, $11 - 19$ cm separation between the two sides, about 64 windings per one side (8 layers, 8 windings

[25]The maximum output power by spec is 500 mW, our TA power is limited by

Beam	transition	frequency detuning in Γ
2D MOT Trap	^{7}Li D2 $F = 2 \rightarrow F'$	$-8.19\,(-7.0)$
2D MOT Repump	^{7}Li D2 $F = 1 \rightarrow F'$	-0.12
Pusher	^{7}Li D2 $F = 2 \rightarrow F'$	$-0.18\,(+1)$
3D MOT Trap	^{7}Li D2 $F = 2 \rightarrow F'$	$-6.15\,(-5.0)$
3D MOT Repump	^{7}Li D2 $F = 1 \rightarrow F'$	-0.33
3D CMOT Trap	^{7}Li D2 $F = 2 \rightarrow F'$	$-2.05\,(-0.9)$
3D CMOT Repump	^{7}Li D2 $F = 1 \rightarrow F'$	-1.86
Imaging	^{7}Li D2 $F = 2 \rightarrow F'$	$-0.89\,(+0.3)$
Lattice cooling	^{7}Li D1 & D2	$-15 \sim +5$ GHz to D2

Table 4.1: Frequency detunings. The excited state reference point of each transition is the fine structure of the corresponding excited state. Detuning values in the parenthesis are referenced to the cycling transition.

per a layer), 30 A current through the coil can generate 20 G/cm at the center of the chamber.

4.5 Experimental sequence

We use National Instrument data acquisition boards and Cicero software (Fig. 4.23) to control the sequence (Fig. 4.24). 3D MOT loading is done for 1 s and it gives typically $3-4\times10^7$ atoms[26] in the trap with temperature of 1 mK. After loading into 3D MOT, atom cloud is compressed (CMOT- compressed MOT) by ramping up the MOT magnetic field gradient to 30 G/cm [27], decreasing the power to 20% of the power in MOT loading stage and decreasing the frequency detunings to -12 MHz for trap beam and -11 MHz for repump beam. After the CMOT stage atoms are cooled to 300-400 μK.

During the last 1 ms of CMOT stage, the lattice cooling beam is shined. After CMOT stage ends, 3D MOT trap and repump beam as well as 3D MOT magnetic filed are turned off. The magnetic field decays with a time constant of $\tau_{e^{-2}} \sim 500\,\mu$s due to eddy currents. The lattice cooling beam stays on for lattice holding time (500 μs- 1500 μs), then the lattice cooling beam is turned off using both AOM and a mechanical shutter[28]. During the time of flight (TOF) stage all light and magnetic field is off and atoms expand freely. After the expansion the imaging beam is turned on for 200 μs in fluorescence imaging mode (65 μs in absorption

[26]the atom number is limited by available laser intensity of 3D MOT, we observe sharp increase (1.5-2$\times$) in atom number when 3D MOT power is increased (by 25%).

[27]As discussed in 5.4, CMOT works without changing magnetic field gradient and gives similar final temperature after the compressing the MOT.

[28]a mechanical shutter shut-off time is on the order of 1 ms, therefore an AOM is needed to turn off faster.

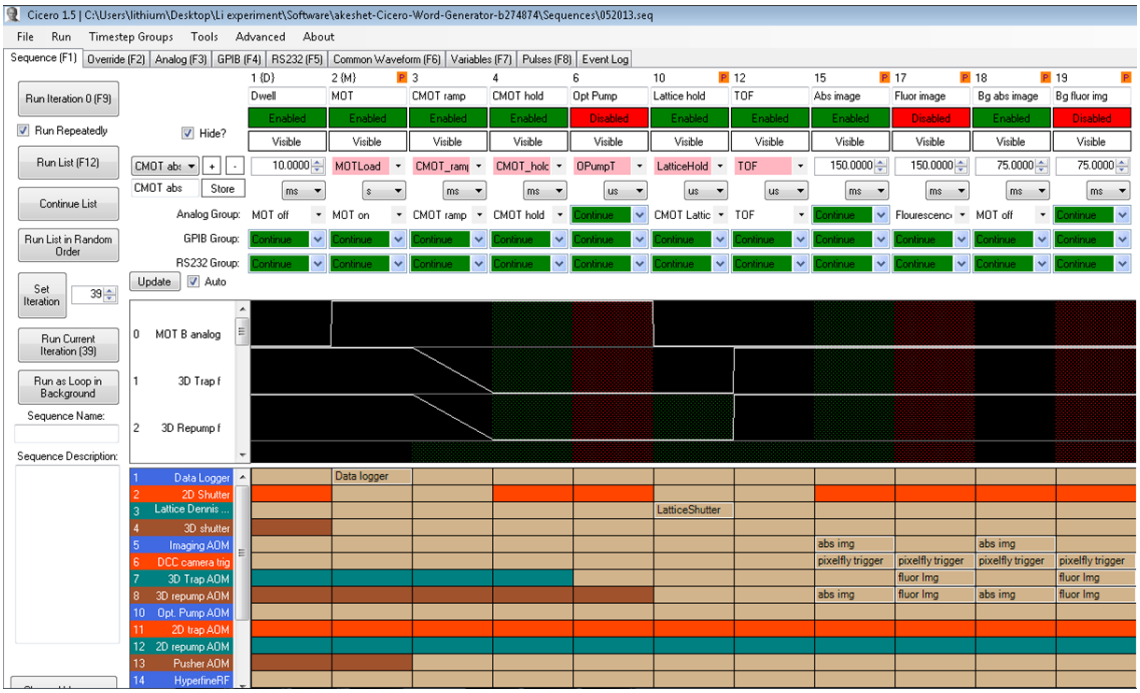

Figure 4.23: Cicero software for sequence control.

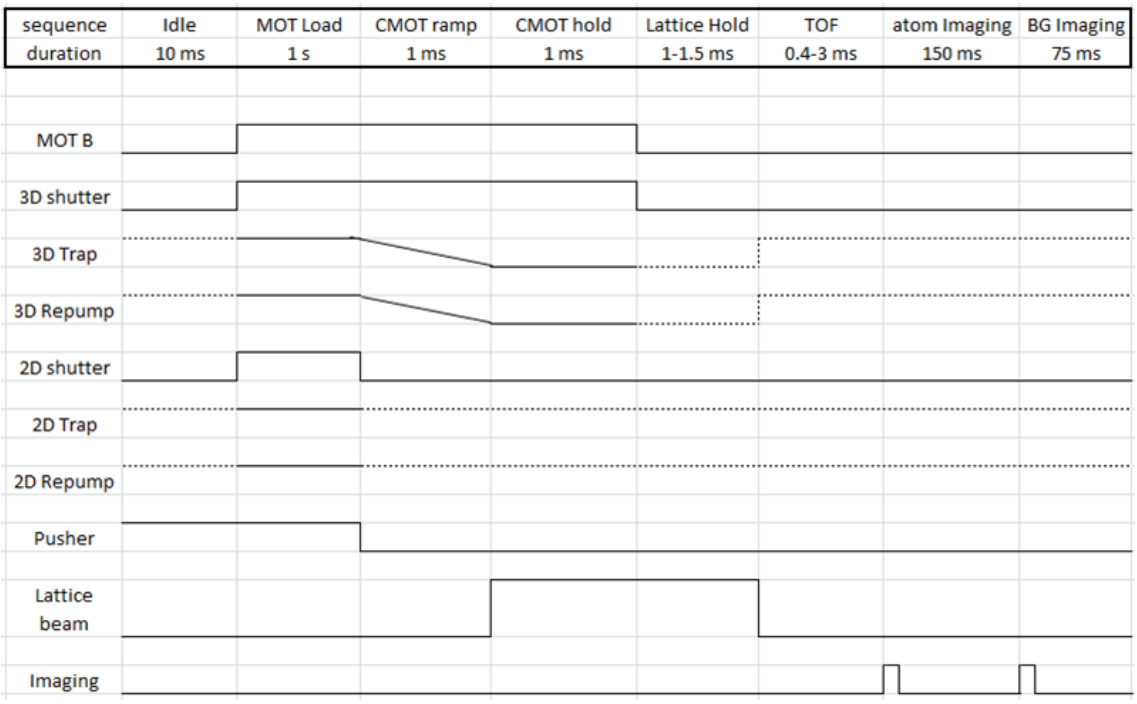

Figure 4.24: Experiment control sequence.

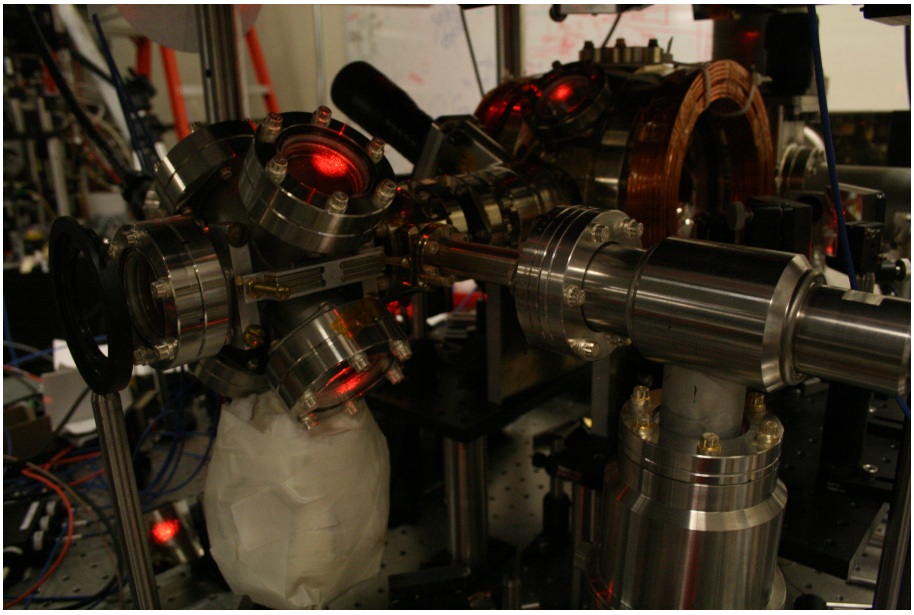

Figure 4.25: MOT setup.

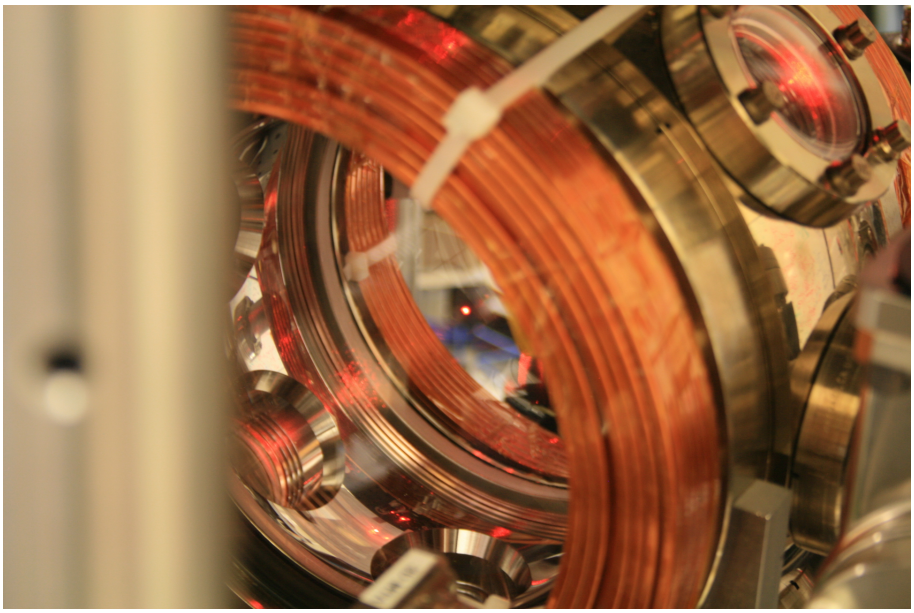

Figure 4.26: 3D MOT: A bright spot at the center is an image of atom cloud trapped in the 3D MOT.

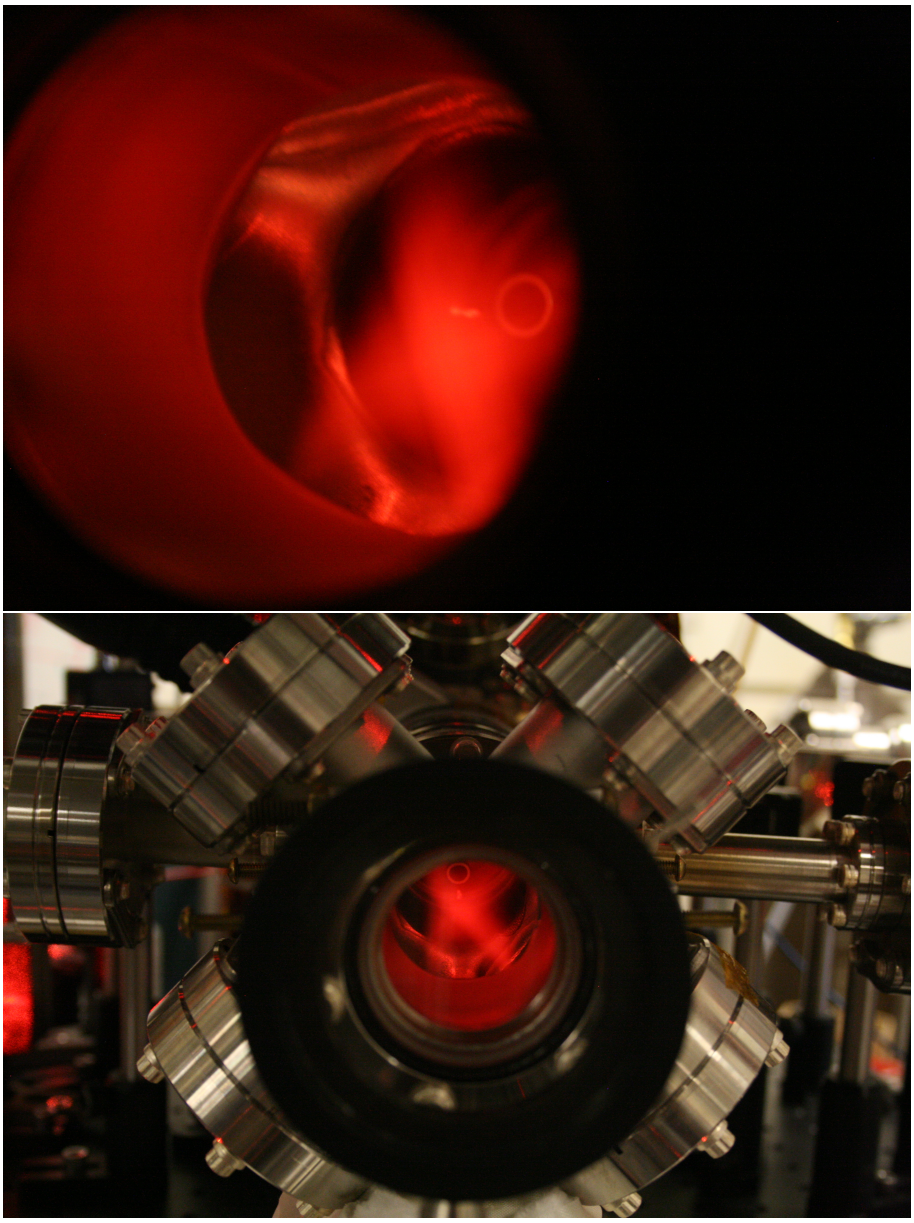

Figure 4.27: 2D MOT: A bright spot in the middle is an image of atom cloud trapped in the 2D MOT.

imaging mode) and takes an image of the atom cloud. To compensate a background noise from the imaging beam, after about 150 ms of idle time the imaging beam flashes again and takes an image without atom. We use a software written in MATLAB to show processed images and calculate MOT number and size in real time. By scanning TOF duration the cooled temperature is calculated from a time of flight fit.

Chapter 5

Result

Overview

We find the cooling depends on various factors: cooling beam intensity, cooling beam detuning, cooling beam polarization, holding time in the lattice, cooling beam shut-off time, MOT and CMOT current (magnetic potential depth), residual magnetic field gradient in the MOT center, temperature after CMOT stage, and dimension of cooling. Despite of these many factors to be optimized to get the lowest cooled temperature possible and larger cooled fraction, cooling can be obtained without precise conditions and complicated alignment as in Raman sideband cooling and without huge beam intensity requirement, long cooling cycle ($1 \sim 10$ s) and small efficiency (<0.01%) as in evaporative cooling. In this chapter each factor's effect on cooling temperature and fraction is discussed. We address optimal conditions first and then focus on main control parameters (cooling beam intensity, detuning and polarization) and their effect on cooling temperature, effect of (non)adiabatic switch-off of cooling beam on cooling temperature in 1D cooling and we also discuss the result for 3D cooling.

5.1 General features and optimum conditions

We observe cooling in a broad range of detuning[1]and modest beam intensity[2]. Holding time of $500 \sim 2000\,\mu s$ in the lattice showed that the cooling works without compromising the fraction too much, and the optimum holding time occurs between $1000\,\mu s$ and $1500\,\mu s$ for -5 GHz detuning from D2. At this optimal point the lowest cooling temperature and considerable cooled fraction happens. Within the parameter space we obtained cooling as low as $20 \sim 50\,\mu$K with cooling fraction of 10 ∼40% in 1D cooling and $70 \sim 100\mu$K with fraction of $20 \sim 60\%$ in three dimension. We find the cooling in three dimension the lowest cooling

[1]Almost any detuning between D1 and D2 for $lin \perp lin$, and red to D1 and blue to D2 for $lin \parallel lin$

[2]$20 \sim 150$ mW at $1.4 \sim 1.5$ mm beam waist

temperature was higher than in one dimension[3] and the cooling fraction is always higher. We also find that 3D cooling is more robust than in one dimension in the sense that 3D cooling works well even with low beam power where 1D cooling would not work, and temperature is less sensitive to parameter changes than in 1D.

5.1.1 Alignment

When MOT and CMOT magnetic potential minimum and molasses light potential minimum are not at the same position, the total potential minimum position changes as MOT (CMOT) is extinguished and can force the cloud to one direction and disrupt cooling. To get best cooling at given conditions we optimize the MOT potential minimum position by aligning MOT beams such that the MOT position does not change as magnetic field gradient changes; we simply ramp up and down the MOT current and tweak MOT mirrors until the cloud does not move. Cooling beam is roughly aligned by hitting cloud with a cooling beam tuned to close-to-resonance until it disturbs the cloud most and then further alignment is done while running the computer sequence and watching the image updated in real time and make the cloud shape as symmetric as possible. Alignment is considered to be optimized when we observe biggest atom number captured after cooling and best cooled cloud shape- i.e. double Gaussian shape. Yet cooling beam alignment affects cloud shape and cooling performance it is as robust as 10 degree of misalignment would not greatly affect the cooling result.

5.1.2 Effect of MOT magnetic fields and CMOT temperature

We obtained $300 \sim 400\,\mu K$ temperature after CMOT when MOT and CMOT current varied from 15 A to 50 A where the CMOT current is the same as MOT current. Generally when MOT (and CMOT) current is higher, the cloud is more tightly confined in the MOT potential thus has smaller cloud size and higher atom number. We observe substantial change in 1D cooling temperature when the MOT current is varied (Fig.5.1). We find there is a trade-off between temperature and the over all atom number as we vary the MOT current therefore as an empirical optimum condition we used 25 A for MOT and CMOT current (corresponding to 17 G/cm) to obtain lower final cooling temperature and still good number of atoms. We also tried CMOT current different from MOT current by ramping up or down the current during the CMOT stage however it did not change or increased the cooling temperature. Sitting at not-optimum conditions for CMOT beam frequencies can make CMOT temperature higher even when CMOT current is not changed. Most time we kept the CMOT temperature between 300 to 340 μK at 25 A however rarely but it happened that CMOT temperature was increased up to $370\mu K$ due to long-term drift of our spectroscopy

[3]We attribute it to our 3D cooling beam geometry which is over constrained, and the limited cooling beam power that is only 35 mW per axis in three dimensional case.

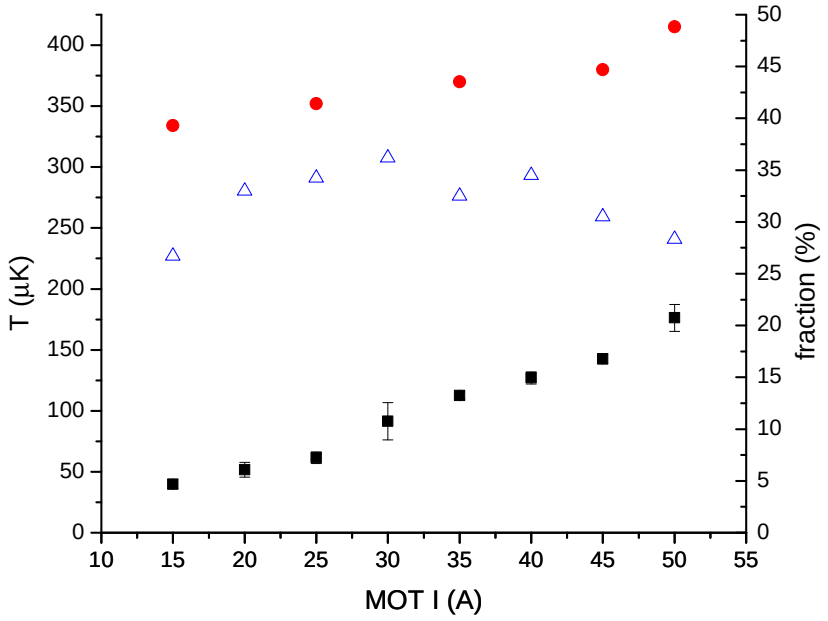

Figure 5.1: 1D cooling temperature vs. MOT and CMOT current. Square- 1D cooling temperature, Triangle- 1D cooling fraction, Circle- CMOT temperature.

lock point, and when it happens we either re-optimized the MOT and CMOT frequencies or re-adjusted the frequency locking point.

5.2 1D cooling

We observed a cooling in 1-dimensional optical lattice. The typical sign of 1D cooling is shown in Fig.5.2. The cloud is squashed in the cooling beam axis and elongated along the other axis. In certain conditions where the cloud's momentum distribution exhibit long-tailed shape, it can be modeled as double-Gaussian which is the simplest model to separate cooled part from un-cooled (or heated by scattering) part. Temperature of both cooled and un-cooled components are extracted by time of flight measurement with the double Gaussian fit, giving one smaller width (cooled) and one larger (un-cooled). We aligned cooling beams such that the atom cloud is as symmetric as possible and used fixed-center double Gaussian model which has six free parameters; two amplitudes, two widths, common position and offset.

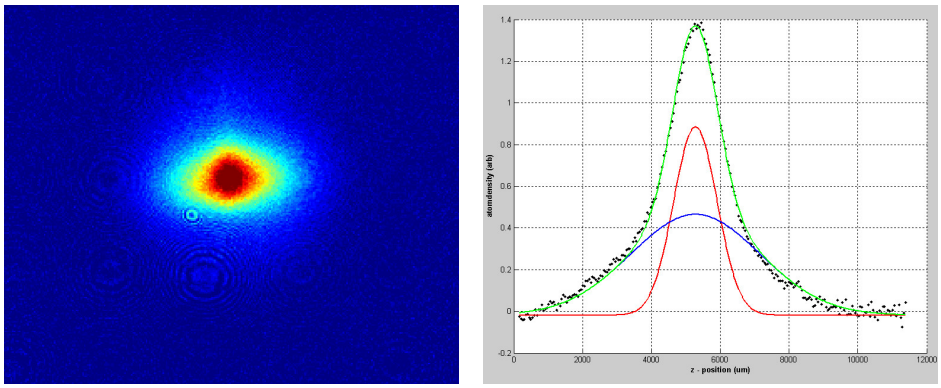

Figure 5.2: Absorption image of a cloud cooled in 1-dimension (left) and its double Gaussian fit (right). A cooling beam comes from below the cloud on the image and its retro-reflected beam shined from the top of the image; the actual beam lies horizontally in the lab frame. Double Gaussian fitting represent a cloud with momentum distribution with separated cooled component (red line) from un-cooled part (blue line). Cooling beam conditions are -5 GHz to D2, 100 mW at 1.42 mm waist, and lattice holding time 1.5 ms.

5.2.1 Effect of cooling beam detuning and intensity: Cooling mechanism

We measure the cooling temperature over various detunings ranging from -5 GHz to D1 transition to +5 GHz to D2 transition and cooling beam intensities ranging from 1300 $\sim$ 7200 mW/cm^2. Fig.5.3 shows 1D cooling temperature dependence on the frequency detunings at fixed power for one symbol on the figure. Region (a) is where frequency is red detuned from ^{7}Li D1 transition, (b) is between D1 and D2 transition, and (c) is blue detuned to D2 transition. In region (a) and (c) low temperature ($10 \sim 30\,\mu K$) and low fraction ($< 20\%$) can be obtained in $lin \parallel lin$ polarization, and higher temperature ($> 60\mu K$) and low fraction ($< 20\%$) for $lin \perp liln$ polarization. Useful cooling ($> 50\,\mu K$ and $\leq 40\%$) happens in region (b) with $lin \perp lin$ polarization, whereas $lin \parallel lin$ does not work in (b). We find that two cooling mechanisms are combined in region (b) and give sub-Doppler temperature and large cooled fraction at the same time.

The big difference between the region (b) and the regions (a) and (c) comes from the difference in the cooling mechanism. As discussed in section 3.3.2, Sisyphus cooling works efficiently in the region (b) and it does not work well in region (a) and (c). In region (b), the cooling temperature is minimum at -5 GHz to D2 and it increases as the frequency gets closer to either of D1 or D2 resonance. Intuitively this is because the parameters used in the plot are roughly in the regime where the Sisyphus cooling temperature satisfies $T \propto U_0$: The total light potential for the detunings red to D2 and blue to D1 is shown in Fig. 5.4. For large enough potential U_0 where $T \propto U_0$ it is expected to have the cooling temperature has the minimum around the center between D1 and D2.

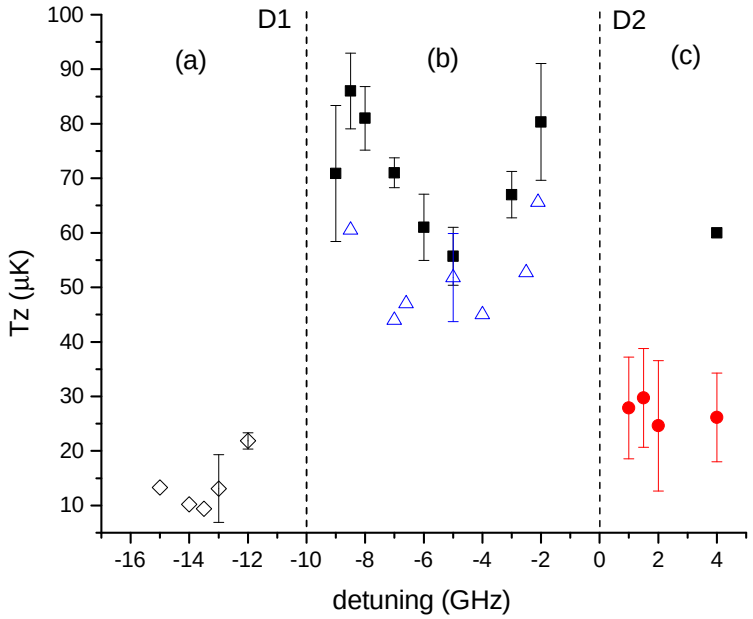

Figure 5.3: 1D cooling at various detuning. Square- 100 mW at 1.42 mm waist ($U_0 \approx 74\,E_r$) with $lin \perp lin$, Triangle- 70 mW at 1.4 mm waist ($U_0 \approx 103\,E_r$) with $lin \perp lin$, Circle- 45 mW at 1.42 mm waist with $lin \parallel lin$, Diamond- 70 mW at 1.4 mm waist, $lin \parallel lin$.

Although the Sisyphus cooling mechanism can explain the overall behavior of the cooling temperature we observed that the experimental result of the minimum cooling temperature (50 μK) is about factor of two lower than the theoretical result of the Sisyphus cooling in D1 and D2 using the quantum treatment. Also, the region (a) and (c) showed a cooling at $lin \parallel lin$ polarization with lower temperature and lower fraction which cannot be explained by the Sisyphus cooling mechanism. We identified the adiabatic cooling (section 3.4) as an additional cooling mechanism which comes into play when we shut off the optical lattice. By chance we were using a mechanical shutter to shut off the lattice beam, thus the shut off time was about 1 ms which is slow enough to turn off the lattice adiabatically. To test our hypothesis we replaced the 40 MHz AOM, which shut-off time is limited to 3.5 μs, by a faster one (200 MHz) and used telescope lens pairs to shrink the lattice beam on the AOM. A fast RF switch using a mixer (a MOSFET generated 40 mA switch current through the 'intermediate frequency' port of the mixer) can shut off the lattice beam through AOM within 40 ns. By modifying RC constant of the gate voltage of the MOSFET, we could easily control the lattice shut off time constant. We varied the shut-off time (time that takes to decay from 90 % to 10 %) from 50 ns to 20 μs and measured the cooling temperature. Fig. 5.5 shows the resulting cooling temperatures when varying the lattice shut-off time.

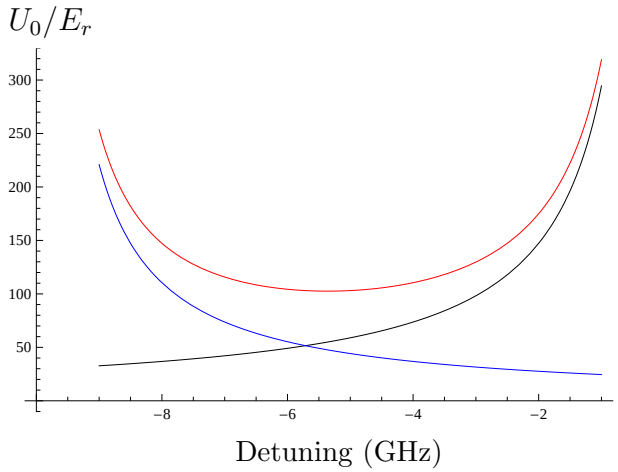

Figure 5.4: Light potential as a function of frequency detuning from D2 at $\Omega = 1.9 \times 10^9$. Blue and black solid lines are potential from D1 and D2 transition respectively, and the red line is the effective potential. The potential minimum value is around 100 E_r near 5-6 GHz red detuned from D2.

We tested at different frequency detunings (-5 GHz and -7 GHz), both shows the same trend which cooling temperature decreases by a factor of two when the lattice is turned off adiabatically.

In Fig.5.6 theoretical and experimental results are compared for 1) cooling with both Sisyphus cooling and adiabatic cooling and 2) Sisyphus cooling without adiabatic cooling. Semi-classical treatment for Sisyphus cooling (red dashed line in Fig.3.8) and Sisyphus+adiabatic cooling (black dashed line) predict temperature higher by more than factor of two than the experimental result, however the quantum treatment (red and black solid lines) agree well with experimental result (Fig. 5.6). Data points were taken at various detunings ranging from -2 GHz to -9 GHz and power ranging from 10 mW to 100 mW [4] in adiabatic and non-adiabatic regime (20 μs and 50 ns turn-off time respectively) and averaged over similar U_0/E_r to show temperature dependence on a universal dimensionless parameter.

Phenomenologically, however, different combinations of experimental parameters lying on the same U_0/E_r parameter are not exactly the same; As shown in Fig. 5.7, resulting temperature is slightly different when different Rabi frequency (beam intensity) is used. While the blue triangles coincide better with the simulation result which used the same Rabi frequency, the black squares shows discrepancy. Also, the cloud shapes after cooling are not the same (e.g. Fig.5.8). This shows that U_0/E_r is not as perfect universal parameter to describe the cooling, however the cooling temperatures are similar within $\sim$20 μK difference and scatters around the theoretical predictions.

[4] Beam waist is 1.42 mm.

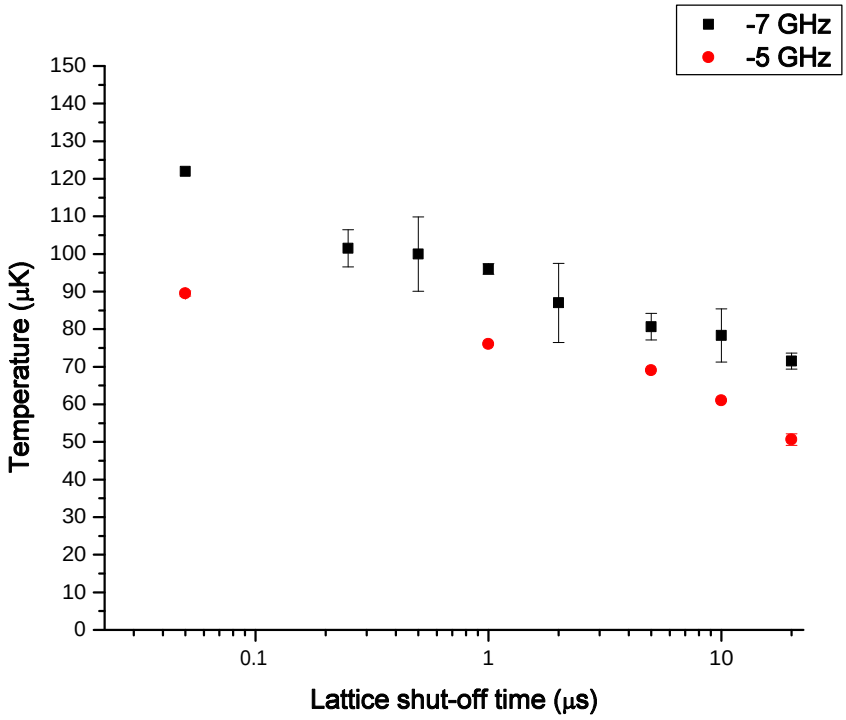

Figure 5.5: 1D cooling at various lattice shut-off time. Square: -7 GHz to D2, Circle: -5 GHz 50 D2. Both data set are taken at 100 mW power and 1.42 mm beam waist with $lin \perp lin$ polarization.

5.2.2 Effect of holding time in the lattice

Holding time (time during which atoms are held in the cooling lattice after CMOT beams and magnetic field are extinguished) affects the final temperature as well as the momentum distribution of the atom cloud. As in Fig.5.10 there is a sweet spot where the cooling temperature is the lowest due to cooling and scattering competition. For fraction or number of atoms left decreases monotonously as holding time increases. At short holding time the cloud starts with round shape and as time of flight increases the shape becomes more elongated as one can expect that atoms expand slower along the cooling axes (vertical on the image), while at longer holding time cloud is already elongated at early time of flight and has less atoms left as seen in Table.5.1. It is interesting to note that this cloud shape by lattice holding time is related to the momentum distribution in cooling axis; for example, holding time of 500 μs at early time of flight exhibit a shape of in-between single and double

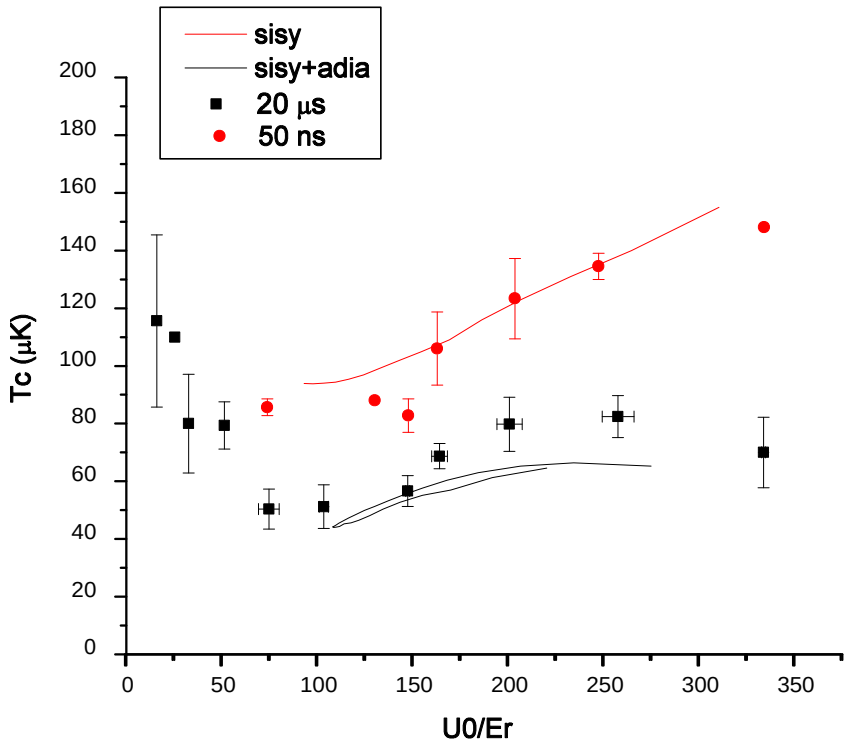

Figure 5.6: Experimental confirmation of two cooling mechanisms. The red and black lines are from simulation and symbols are experimental data. Simulation is done at fixed Rabi (angular) frequency of $1.8 \times 10^9 s^{-1}$ and detunings between $1.5 - 8.5$ GHz red to D2 line. The red solid line represents simulation for only Sisyphus cooling mechanism when localization is considered, whereas the black solid line represents simulation for both Sisyphus and adiabatic cooling mechanisms when localization is considered. Lattice turn-off time values 20 μs and 50 ns correspond to adiabatic and non-adiabatic regime respectively. Data is taken for various frequency detunings and beam intensities, and the points are the result of averaging over similar U_0 which may include different detunig and intensity values.

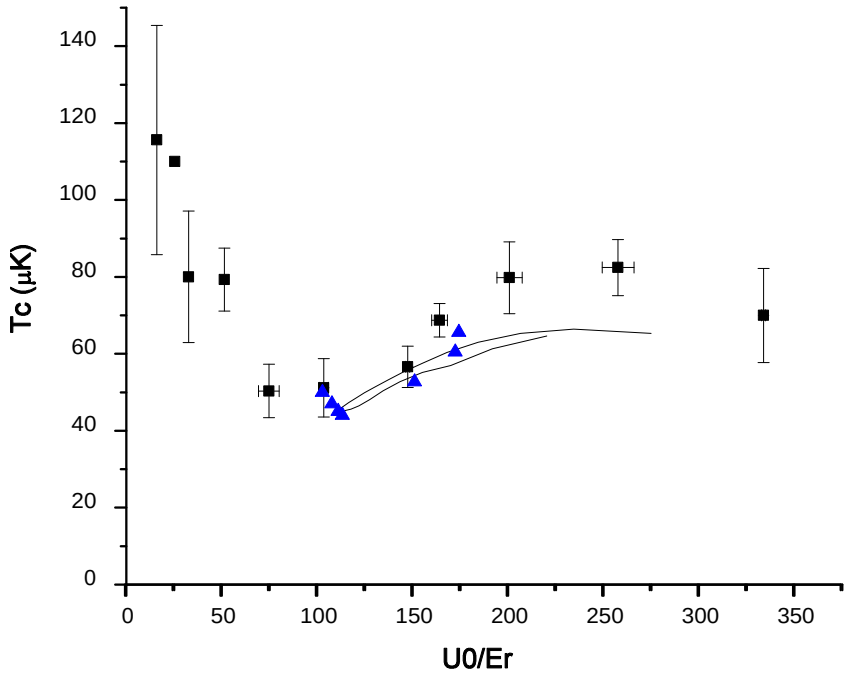

Figure 5.7: Checking U_0/E_r as a universal parameter. Black solid line is a quantum simulation result using Rabi frequency $\Omega = 1.8 \times 10^9\ s^{-1}$ corresponding to experimental parameters $P_0 = 70$ mW, $w_0 = 0.7$ mm used to obtain blue triangles. Blue triangle data points are obtained at a fixed intensity and different frequency detunings, and the one dimensional optical lattice is vertically oriented. Black squares are taken at various beam intensity and detunings and averaged over all different Rabi frequencies, and the optical lattice is horizontally aligned. Despite of difference in optical lattice geometry and other parameters, the final temperature values agree within the uncertainty and show the same trend.

Gauss due to its high cooling fraction where as it becomes clear double Gauss as holding time increases until it is too long. We experienced difficulty with fitting into double Gaussian model when the lattice holding time was around 750 μs or less; difficulty in fitting sigma of cooled component at early time of flight causes inaccuracy in temperature fitting, however this fitting issue has been resolved by using proper lattice holding time. Although we have not tried exploring, the sweet spot can be different for different cooling beam conditions since its cooling efficiency and scattering rate are different.

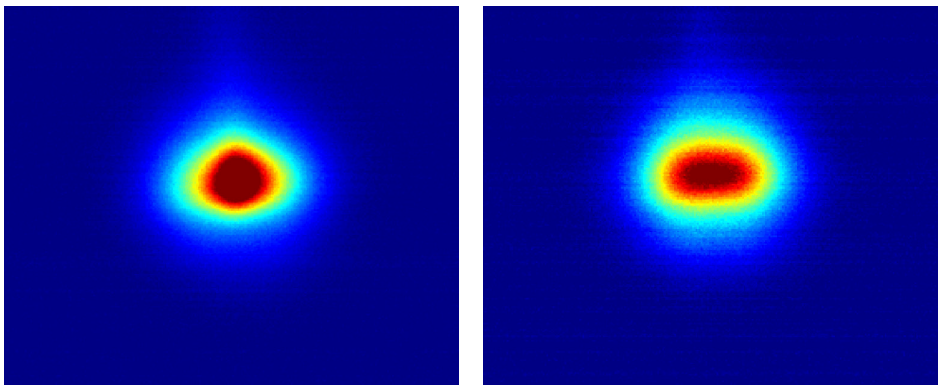

Figure 5.8: Fluorescence image of clouds cooled with detuning of 5 GHz red to D2 (left) and with detuning of 9 GHz red to D2- equivalently 1 GHz blue to D1(right). Note that they have almost the same $U_0/E_r \sim 145$ but are not identical in cloud shape (and resulting cooling temperature) after cooling.

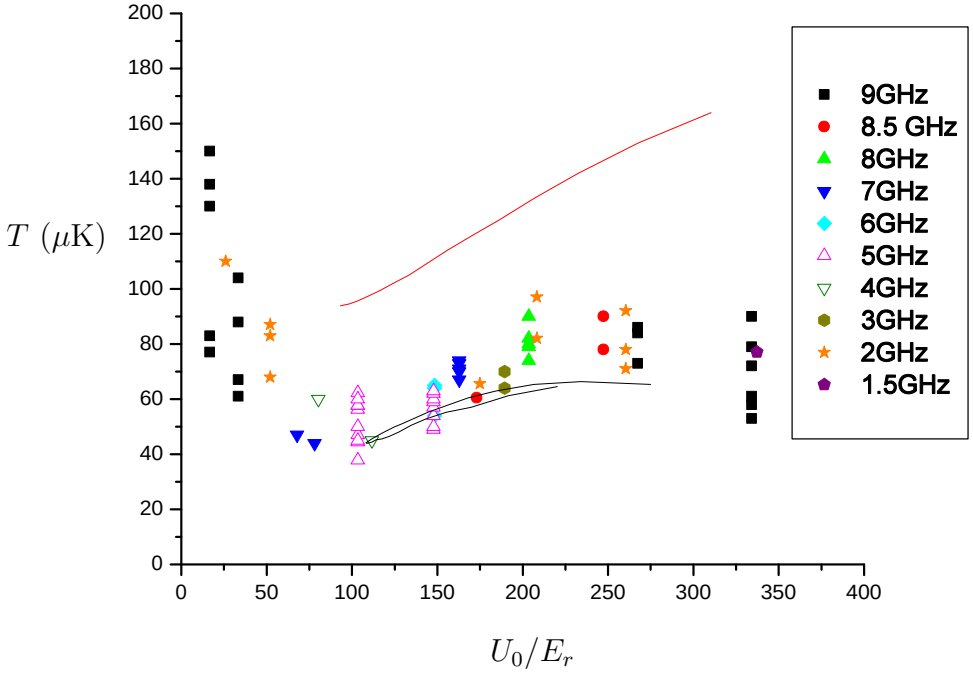

Figure 5.9: 1D cooling temperature at various detunings and beam intensities. Different symbols represent different detunings to ^{7}Li D2 transition locked at ground hyperfine state crossover. Cooling beam polarization is $lin \perp lin$ only.

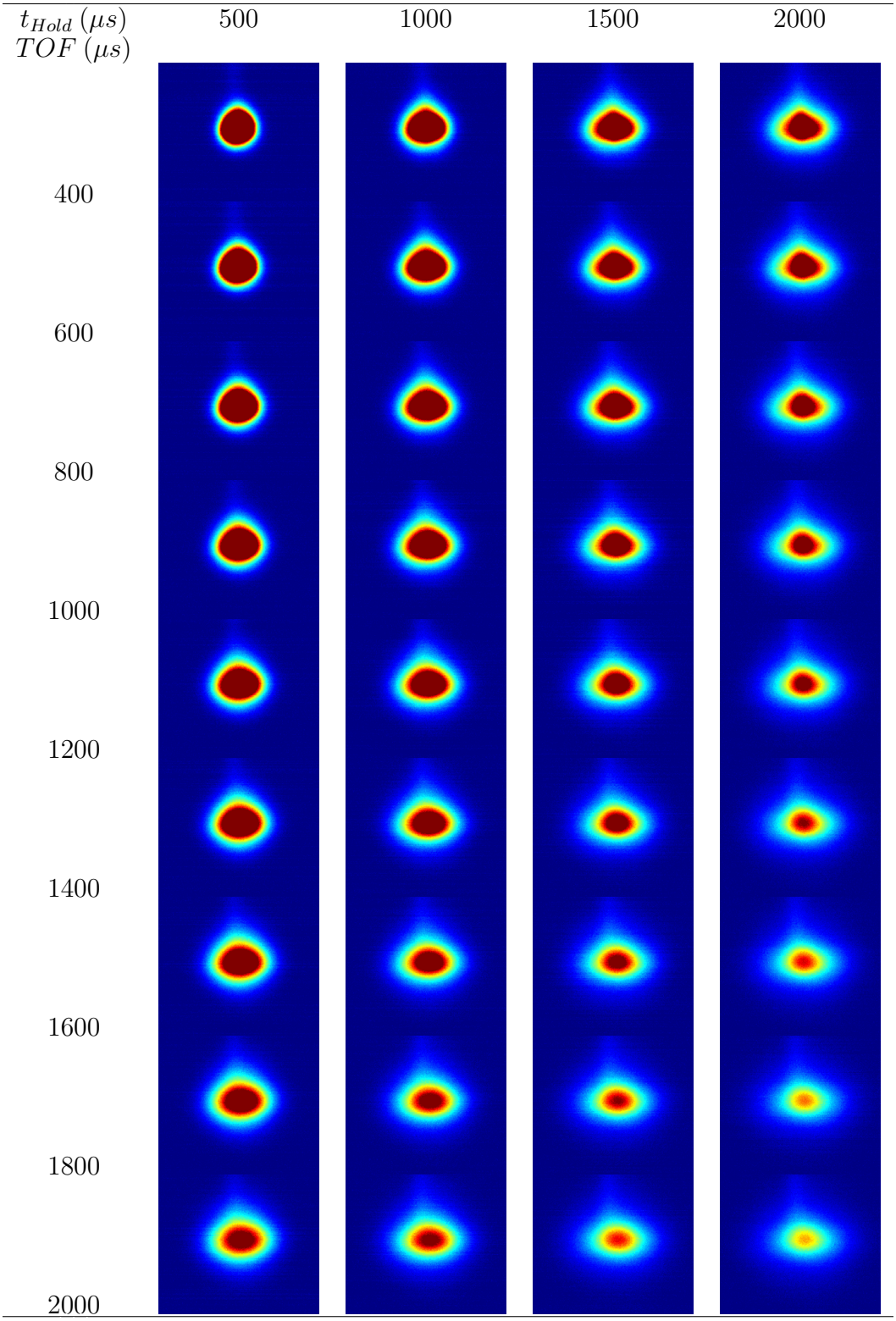

Table 5.1: Time of flight images at various lattice holding time.

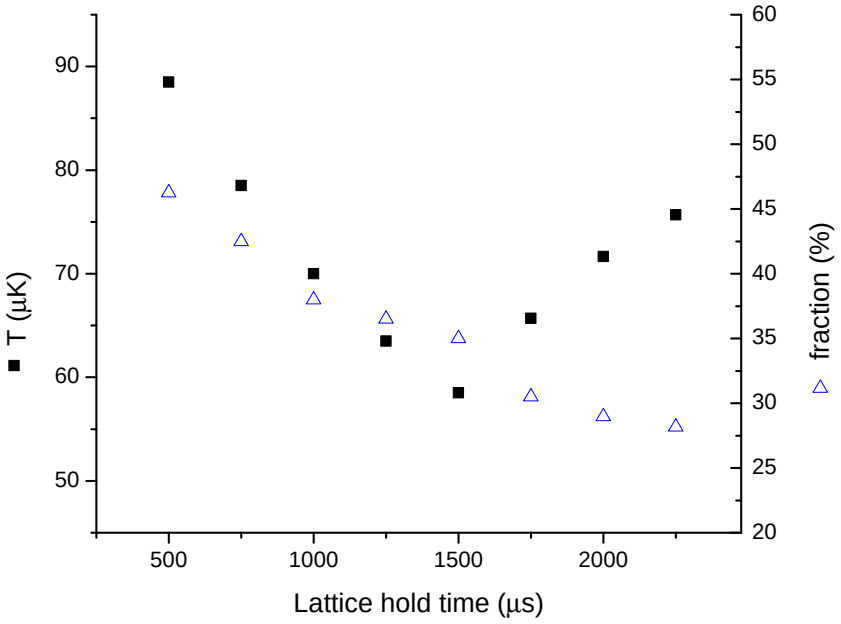

Figure 5.10: Effect of hold time in the cooling(lattice) beam on temperature and fraction. Cooling beam condition was at -5 GHz detuning from D2 with 100 mW. Lowest cooling temperature with good cooling fraction occurs around 1500μs lattice holding time.

5.3 3D cooling

We split 110 mW cooling beam into three paths using polarizing beam splitter cubes and used retro mirrors to form a 3D lattice. The horizontal beam (x-axis) is the same as 1D lattice, and the other two axes are on the y-z plane, 45° to the z-axis. A CCD camera facing down takes images from the top of the chamber such that it can capture cooling along both horizontal (x) and vertical (y and z) axes. We investigated cooling temperature dependance on detuning, intensity or power ratio, polarization combinations, and fixed other parameters such as lattice holding time and MOT current at the same optimum values for one dimensional lattice cooling. The resulting cooling temperature dependance on detunings is shown in Fig.5.11. Compared to the 1D result, the cooling fraction stays relatively high and plain across the different detunings, which is because atoms are cooled from all directions. In terms of overall cooling temperature, the resulting cooling temperature in 3D lattice is higher than in 1D. This is due to combination of two factors- first, the power per one beam in 3D lattice is only one third of the value in 1D lattice which makes small potential depth. The second reason is that adiabatic cooling mechanism does not work efficiently due to the lattice geometry. We used six-beam geometry (three orthogonal laser beams with retro-reflections) rather than pyramid geometry due to our chamber shape. In a 3D lattice, the six-beam

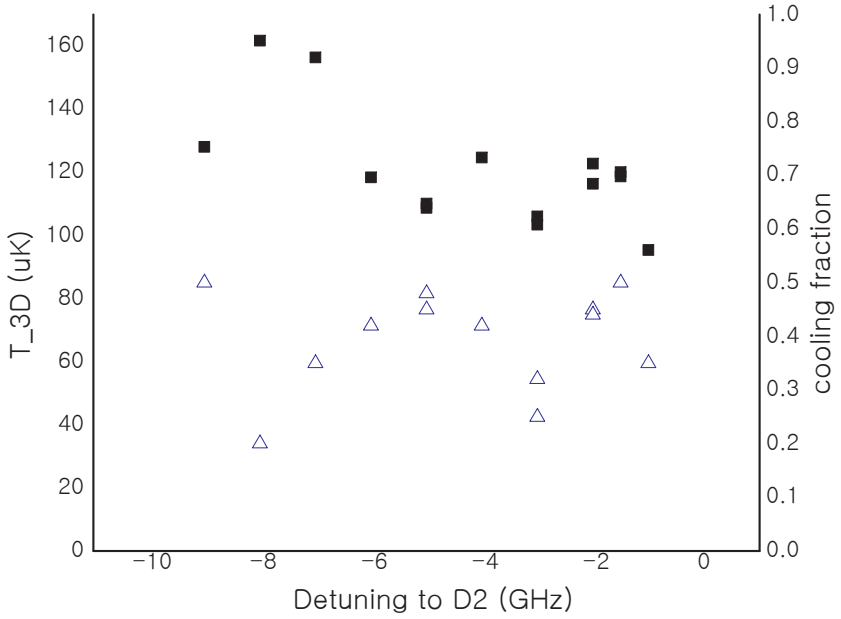

Figure 5.11: 3D cooling temperature vs. Detuning. Square- 3D cooling temperature, Triangle- 3D cooling fraction. Polarization is kept $lin\perp lin$ for all three axes, beam size kept the same as $r_{e^{-2}} = 0.71$ mm, the total laser power is 110 mW which equally split into three.

geometry makes the lattice over-constrained thus the three dimensional potential shape can rapidly fluctuate which makes adiabatic cooling difficult.
As shown in Fig.5.11 the cooling temperature decreases as the laser frequency gets closer to the resonance which indicates that the light potential is smaller than the potential that the minimum cooling temperature when we take an analogy to the 1D cooling temperature versus potential curve as shown in Fig. 5.6 and Fig. 5.9.
We also tried different polarizations (all $lin\perp lin$, all $lin\|lin$, and part $lin\perp lin$ - part $lin\|lin$ polarizations) in the 3D lattice beam, but did not find any big difference in the cooling temperature result. In a blue lattice (2 GHz blue to D2 detuning), lower temperature (50-60 μK) was achieved with lower cooling fraction (< 20 %). The cooling temperature with different power ratio showed that the axis with greater power gives higher cooled atom fraction for that axis, but lower fraction for the rest axes which power became lower.

5.4 Result summary

The cooling temperatures and the conditions in various cooling stages in our experiment is shown in Table 5.2. We observed a sub-Doppler cooling temperature about $T \sim 7T_r$ in

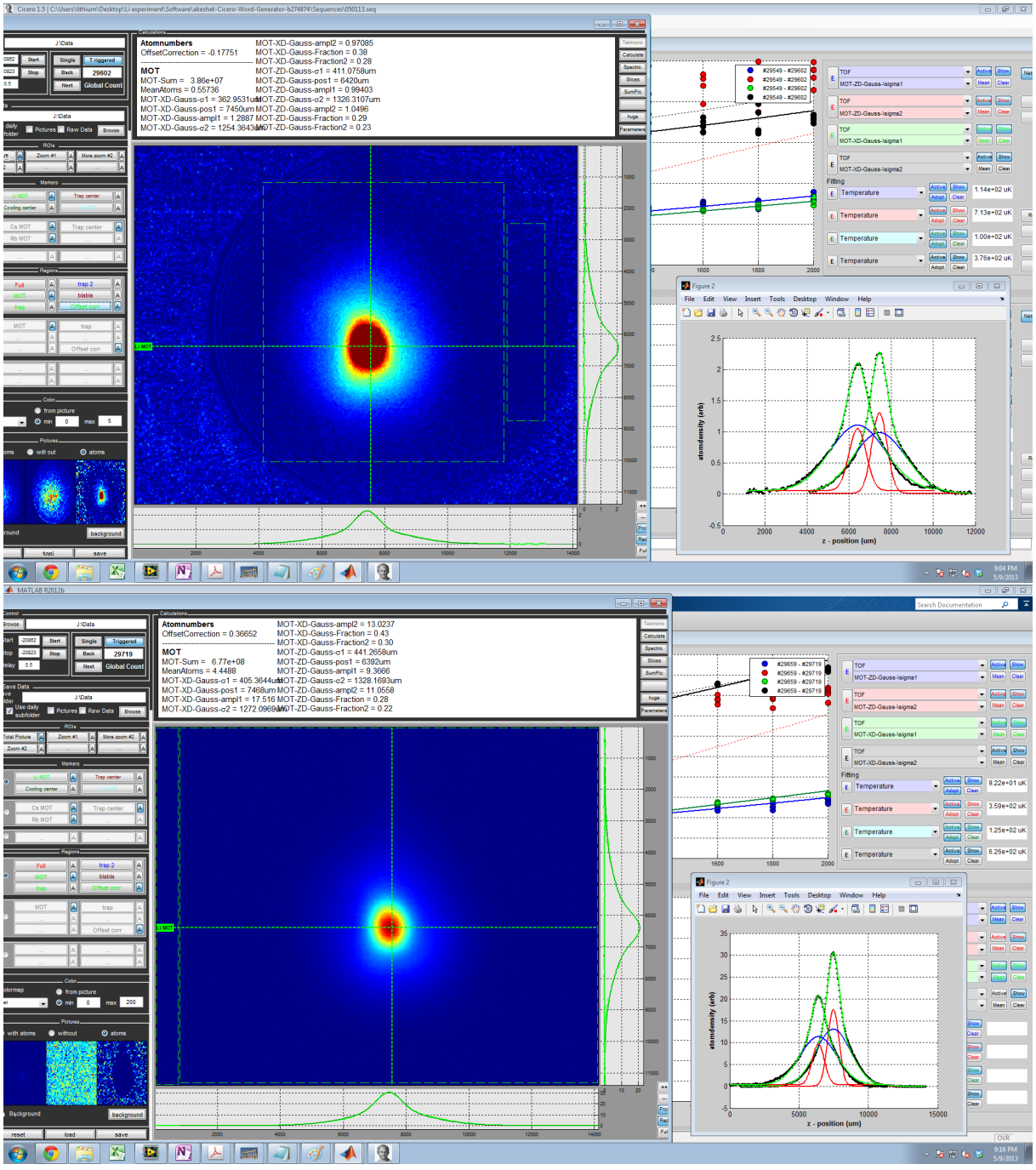

Figure 5.12: Absorption (upper) and fluorescence (lower) images of atoms cooled in 3D

Cooling Type	Conditions	Temperature	Atoms
3D MOT	$B' = 17$ G/cm,	1 mK	5×10^7
	$\Delta = -36$ MHz, 16 mW/cm^2/beam, $\sigma^+ - \sigma^-$		
3D CMOT	$B' = 17$ G/cm,	350 μK	5×10^7
	$\Delta = -12$ MHz, 3.2 mW/cm^2/beam, $\sigma^+ - \sigma^-$		
1D Sisyphus Only	$\Delta = -5$ GHz (D2), 6500 mW/cm^2, $lin \perp lin$	$85 - 100$ μK	$30 - 40$ %
1D Adiabatic Only	$\Delta = -4$ GHz (D1), 4500 mW/cm^2, $lin \parallel lin$	10 μK	$5 - 15$ %
	$\Delta = +4$ GHz (D2), 6500 mW/cm^2, $lin \parallel lin$	30 μK	$10 - 20$ %
1D Sisyphus+Adiabatic	$\Delta = -5$ GHz (D2), $4500 - 6500$ mW/cm^2, $lin \perp lin$	40-55 μK	$30 - 50$ %
3D Sisyphus	$\Delta = -2 \sim -5$ GHz (D2), 2200 mW/cm^2/axis, $lin \perp lin$	100 μK	$30 - 50$ %

Table 5.2: Cooling result summary

1D lattice, and identified the mechanism of the cooling. We discovered that the cooling mechanism is due to the combination of the Sisyphus cooling and the adiabatic cooling.
The final temperature by a combination of the Sisyphus and the adiabatic cooling is as low as 40 μK in 1D lattice, and the cooling efficiency is as high as 50 %. When the lattice is switched off faster than the adiabacity condition, only Sisyphus cooling mechanism works and gave 100 μK in 1D. In 3D lattice, our lattice geometry is not a stable 3D lattice, thus adiabatic cooling did not work efficiently yet Sisyphus cooling worked and gave a final temperature of 100 μK.
Table 5.3 shows the Doppler limit and recoil limit of the alkali atoms typically used in ultracold atom experiments. Most alkali atoms have similar Doppler limit values in $120 - 250\mu$K range while the recoil limit values widely changes. Theoretical limit of laser cooling is the recoil temperature, however in real experiments the final temperature of Sisyphus cooling stays at about 20 times recoil temperature as discussed in section 3.3. A Sisyphus cooling temperature of cesium has been reported to 3 μK [27], and 6 μK for rubidium [28] which temperatures are in $15-20\,T_{rec}$ range. With the same analogy, for ^{7}Li, the recoil temperature is 6 μK thus the Sisyphus cooling result is expected to be in $90 - 120\,\mu$K which agrees with our result. Although the Sisyphus cooling has been enough to give a temperature far below the Doppler limit for typical alkali atoms such as cesium and rubidium, due to the high recoil temperature of lithium, the result from the Sisyphus cooling only (100 μK) is not attractive compared to the Doppler temperature (142 μK). Our combined method (Sisyphus+Adiabatic) can improve the result by about factor of two (40 μK)[5], with a high efficiency (50 %).

[5]Confirmed in 1D, but the adiabatic cooling did not work in 3D due to our setup geometry, however in principle with the same method a lower temperature can be obtained also in 3D.

Atom	Mass (a.u.)	D2 transition line λ (nm)	D2 line width $\Gamma/2\pi$ (MHz)	Doppler limit T_D (μK)	Recoil limit T_{rec} (μK)
^{6}Li	6	670.977	5.9	142	7.07
^{7}Li	7	670.961	5.9	142	6.06
^{23}Na	23	589.158	9.8	235	2.40
^{39}K	39	786.701	6.0	145	0.836
^{40}K	40	786.701	6.0	145	0.808
^{85}Rb	85	780.241	6.1	146	0.370
^{87}Rb	87	780.241	6.1	146	0.362
^{133}Cs	133	852.347	5.2	126	0.198

Table 5.3: Alkali atoms and their cooling limits

Chapter 6

Atom source improvement- Zeeman slower

We used a 2D MOT over a Zeeman slower in our setup since a 2D MOT requires less instrumentation effort and time for setup. Our compact oven and 2D MOT design gives 5×10^7 atoms in the 3D MOT with 1 s loading time. More than 10^8 lithium atoms can be trapped in 3D MOT using a similar design 2D MOT [13], however the highest atomic flux to date can be obtained from a Zeeman slower [91, 92, 93]. Typically, a Zeeman slower can have more than a factor of 10 higher atom flux than a 2D MOT. A Zeeman slower requires careful design in order to operate properly. In this chapter our Zeeman slower design and its simulation are discussed.

6.1 Zeeman slower design

6.1.1 How it works

A Zeeman slower is used to decelerate hot atoms from the oven.[1] Atoms coming from a hot oven have axial velocity distribution according to Maxwell-Boltzmann distribution, where the most probable velocity is $v_p = \sqrt{2k_BT/m}$. For lithium atoms entering into Zeeman slower, the mean velocity is on the order of 1000 m/s and it has to be decelerated to around 100 m/s to be loaded in to 3D MOT. Zeeman slower decelerates hot atoms by shining laser beam against the hot atom beam. Zeeman slower provides a magnetic field varying a long the slowing axis such that the Zeeman shift compensates Doppler shift all the time and atoms are always on resonance to the slower beam during the slowing process. The resonance condition for atoms in Zeeman slower can be written as (6.1), where δ_0 is the laser detuning to the

[1] Using oven and Zeeman slower as atom source can generally produce higher atom flux than using a getter or a design consisting of an oven and a 2D MOT. It has been reported that 2D MOT can also produce comparable 3D MOT loading rate as Zeeman slower does [13]. The preference can be different for different atomic species and also the experimental need.

unperturbed energy level, $\frac{v}{\lambda}$ is the Doppler shift and $-\frac{\mu B}{h}$ is the Zeeman shift[2].

$$\delta = \delta_0 + \frac{v}{\lambda} - \frac{\mu B}{h} = 0 \tag{6.1}$$

The deceleration comes from the scattering force experienced by an atom when it is excited by a photon in the laser field and spontaneous decay back to ground state. The momentum of a laser photon is against the atom's momentum but the photon emitted by spontaneous emission has no preferred direction, therefore after many cycles the atom is decelerated along the slowing axis. Scattering force F_{scatt} = (photon momentum) × (scattering rate) and in two-level system it can be written as (6.2)[1].

$$F_{scatt} = \hbar k \frac{\Gamma}{2} \frac{s}{1 + s + 4\delta^2/\Gamma^2} \tag{6.2}$$

Here, s is the saturation parameter defined as $I/I_{sat} = 2\Omega^2/\Gamma^2$. At the infinite laser intensity limit, the maximum deceleration is set by

$$a_{\max} = \frac{\hbar k}{m} \frac{\Gamma}{2}. \tag{6.3}$$

For ^{7}Li, $a_{\max} = 1.8 \times 10^6\ m/s^2$. In reality, the beam intensity is finite, therefore the deceleration is less than $a_{\max}$, and often the efficiency parameter η is introduced[3]; $a = \eta_{beam} a_{\max}$. If atoms are always on resonance with the light, then (ideally) the average deceleration over all atoms are constant along z, from which we can model the Zeeman slower with constant deceleration. From ${v_0}^2 - v^2 = 2az$, the ideal velocity profile along z becomes

$$v(z) = v_0 \sqrt{1 - \frac{z}{L_0}}, \tag{6.4}$$

where v_0 is the initial velocity at the entrance and L_0 is a distance where the velocity becomes zero[4]. The ideal magnetic field profile from the resonance condition (6.1) is

$$B(z) = B_0 \sqrt{1 - \frac{z}{L_0}} + B_b, \tag{6.5}$$

where B_0 is a parameter setting the maximum capturable initial velocity $B_0 = \frac{h}{\mu\lambda} v_0$, and B_b is the bias magnetic field which is related to the laser detuning $B_b = \frac{h}{\mu}\delta_0$.

[2]In general, μ is a constant times the Bohr magneton. Note that the Zeeman splitting may not be proportional to magnetic field in some magnetic field regime.

[3]In the literature, η is called safety parameter when it comes to designing the magnetic field profile. However, the safety parameter is set by the magnetic field whereas there is an inherent deceleration efficiency set by the laser beam intensity (and detuning); here they are distinguished as η_{Bfield} and η_{beam}.

[4]Note that L_0 doesn't have to be the length of the Zeeman slower

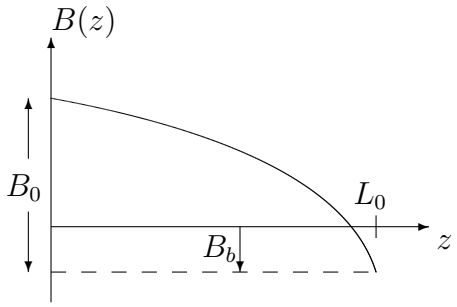

Figure 6.1: Magnetic field in Zeeman slower. B_b can be both positive or negative depending on the design.

6.1.2 ^{7}Li Zeeman shift

In the magnetic field above 20 G (Fig. 6.3), the excited state($2^2P_{3/2}$) of lithium is in the Paschen-Back regime where J and m_J become good quantum numbers instead of F and m_F. In the Paschen-Back regime, the electron total angular momentum J and the nuclear spin I are uncoupled therefore the energy shift is given by

$$\Delta E_{PB} = \mu_B g_J m_J B + \mu_B g_I m_I B + m_I m_J A_{HFS} \tag{6.6}$$

For the magnetic field range inside the Zeeman slower, the ground states ($2^2S_{1/2}$) are in a regime where there is no general analytic expression. However for the special case of $F = I \pm 1/2$, which $^7Li(I = 3/2)$ $F = +2$ state satisfies, an analytic expression known as Breit-Rabi formula exists [4]. For $S_{1/2}F = +2, m_F = +2$ state, the energy shift in Breit-Rabi regime simplifies as

$$\Delta E_{BR} = \frac{3}{4} A_{HFS} + \mu_B B \tag{6.7}$$

Constants A_{HFS} in equation (6.6) and (6.7) are magnetic dipole hyperfine constant for corresponding states. Since A_{HFS} for $P_{3/2}$ state is small (-3.05 MHz) and the nuclear gyromagnetic ratio g_I is three orders of magnitude smaller than electronic one $g_{J'=3/2}$, those two terms are negligible in equation 6.6. Therefore, for $J' = 3/2$ state the energy splitting is just

$$\Delta E_{PB,J'=3/2} = \mu_B g_{J'} m_{J'} B \tag{6.8}$$

and the magnetic field induced part of the total energy splitting is therefore,

$$\Delta E_B = \mu_B g_{3/2} m_{3/2} B - \mu_B B \simeq \mu_B B \tag{6.9}$$

Therefore equation(6.10)becomes

$$\delta = \delta_0 + \frac{v}{\lambda} - \frac{\mu_B B}{h} = 0. \tag{6.10}$$

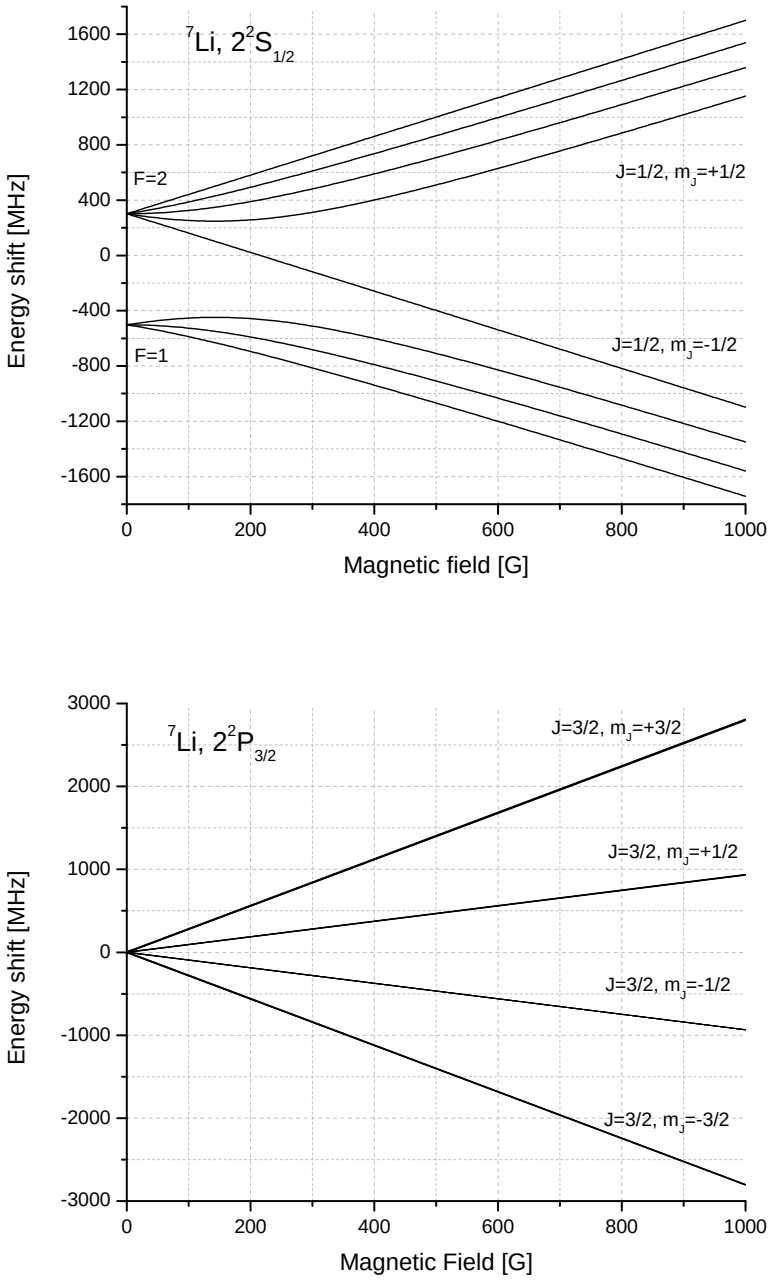

Figure 6.2: Magnetic field dependence on energy shifts of ^{7}Li ground state ($2^2S_{1/2}$) and excited state ($2^2P_{3/2}$) magnetic sublevels

Property	Value [Ref]
g_J Electronic g-factor $2^2S_{1/2}$	2.002301 [35]
$g_{J'}$ Electronic g-factor $2^2P_{3/2}$	1.335 [35]
g_I Nuclear g-factor ^{7}Li	-0.001182 [35]
$A_{2^2S_{1/2}}$ Magnetic dipole hyperfine constant $2^2S_{1/2}$	401.76 MHz [37]
$A_{2^2P_{3/2}}$ Magnetic dipole hyperfine constant $2^2P_{3/2}$	-3.05 MHz [38]

Table 6.1: Hyperfine constants of a ground and an excited state (D2) of ^{7}Li.

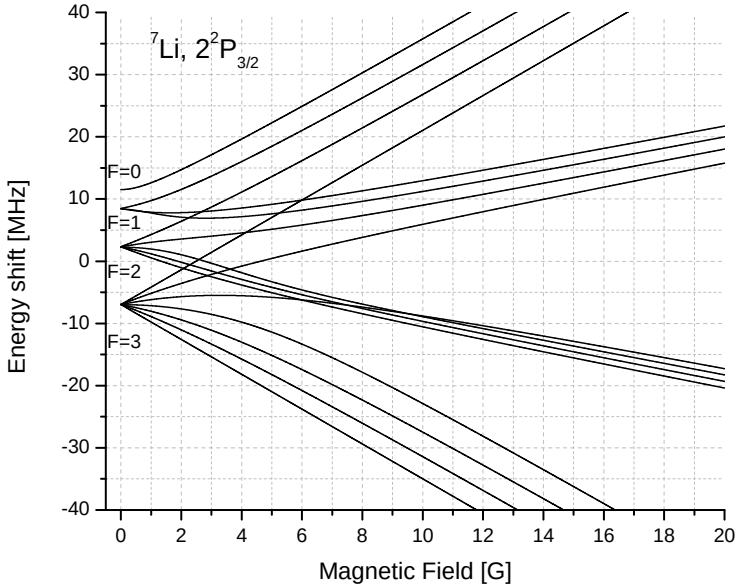

Figure 6.3: Magnetic field dependence of $2^2P_{3/2}$ magnetic sublevels in a low field

6.1.3 Types of Zeeman slower

Most obvious type of Zeeman slower is decreasing field type [2]. In decreasing field Zeeman slower, usually $m_F = +F$ states are chosen and $\sigma+$ polarization beam is used to match the decreasing Doppler shift along z axis. Decreasing field slower has an advantage that close-to-zero field at the exit does not disturb 3D MOT magnetic field, therefore the distance between Zeeman slower and 3D MOT can be closer which enhances 3D MOT loading rate. However it has a disadvantage that the slowing beam disturbs 3D MOT. General methods to avoid this are 1) misaligning a Zeeman slower slightly such that slowing beam does not hit the 3D MOT 2) applying blue-detuned laser beam and positive biased magnetic field. 3) spin-flip Zeeman slower; same as applying red-detuned laser beam and negative biased magnetic field. Another disadvantage is that the final velocity distribution is not as narrow

as increasing field case since atoms are still decelerated after the Zeeman slower exit.

Increasing field Zeeman slower uses $m_F = +F$ states and $\sigma-$ polarization laser beam. Increasing field Zeeman slower defines final velocity better since atoms become suddenly off-resonant to the slowing laser beam at the exit. The large detuning of the slowing beam is advantageous for not disturbing the 3D MOT, however making laser system with a large frequency detuning is inconvenient. Also its large fringing magnetic field at the exit can disturb 3D MOT atoms, so 3D MOT has to be farther then the MOT captures less atoms.

Spin-flip Zeeman slower has been used to combine advantages of both increasing and decreasing field Zeeman slower. The name "spin-flip" is due to the reversed spin orientation with respect to the magnetic field although the atom's spin in lab frame does not change. It starts with decreasing field and the magnetic field crosses zero near the exit and increases. It has relatively smaller fringing magnetic field at the exit and the increasing field region at the end makes narrow final velocity distribution. However at the zero-field point all Zeeman sublevels become degenerate and the population loss into different magnetic sublevels can happen during atoms cross the zero-field point. Moreover, the residual radial field around zero-axial magnetic field($B_z = 0$) makes the quantization axis to be poorly defined with respect to the laser beam polarization therefore atoms are lost into a dark state. A repumping laser beam can help resolving this problem in a limited velocity group range.

6.1.4 Zeeman slower design parameters

Design parameters overview

Zeeman slower performance depends on many parameters. The key parameters are the oven temperature T, the magnetic field profile curve magnitude B_0, bias field B_{bias}, characteristic length L_0, laser beam intensity I and laser beam detuning δ_L. Those parameters are related to not only the resulting quantities but also related to each other and make limiting conditions.

Oven temperature T

Oven temperature is directly related with the atom flux from the oven. The hotter the oven the more atom flux, however increasing oven temperature too high has drawbacks: 1) it increases also the speed of atoms thus makes cooling difficult, 2) too high oven pressure makes the vacuum pressure of MOT chamber high as well. The MOT chamber vacuum pressure should be on the order of 10^{-9} Torr or lower for the MOT operation. A skimmer can be used to make a jet of high flux atoms which is convenient to cool, and to isolate the pressure between the oven and the main chamber.

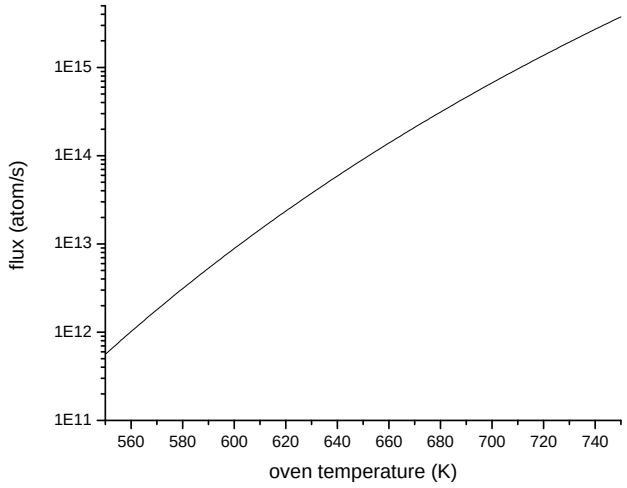

Figure 6.4: Estimated flow rate through the skimmer

Our lithium oven consists of vertical body cylinder and a thin skimmer 90° welded onto the body[5]. The skimmer is 4 mm wide and 15 cm long, which is something in between short and long orifice. Lithium oven runs typically at around 400°C where the saturated vapor pressure is on the order of 0.1 mTorr, the mean free path is about 2 m, and Knudsen number is around $470 (K_n \gg 1)$, therefore it is in the molecular flow regime. In molecular flow regime, the flow rate through short and long round orifice can be described as [5]

$$\begin{aligned} &Q_{short} = \tfrac{1}{4}\bar{v}\ \pi a^2\ (P_1 - P_2)/k_B T \\ &Q_{long} = \tfrac{2}{3}\bar{v}\ \pi a^3/l\ (P_1 - P_2)/k_B T \\ &, where\ \bar{v} = \sqrt{\tfrac{8k_B T}{\pi m}} \end{aligned} \tag{6.11}$$

At $T = 670$ K, $P_1 = 10^{-4}$ Torr, $P_2 = 10^{-8\sim-9}$ Torr, Q ranges $10^{14\sim15}$/s. Atom flux goes up sharply as the oven temperature increases, however the temperature cannot be too high because the mean velocity also increases and the fraction of cooled atoms is limited by magnetic field anyway and all other atoms not cooled are wasted or disturb 3D MOT[6].

[5]Similar to Hulet group design [3]

[6]High flux in hot atoms that are not cooled in Zeeman slower can knock and disturb 3D MOT seriously. To avoid this, some people make a Zeeman slower angled to the main chamber and use a push beam to deflect only slowed atoms.

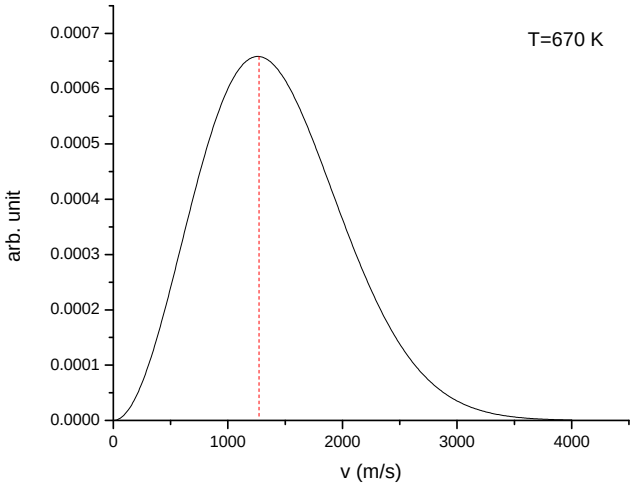

Figure 6.5: Velocity distribution along z-axis

Choosing B_0: targeting initial velocities

Once the oven temperature is set, the percentage of capturable atoms can be easily estimated. In Maxwell-Boltzmann distribution(6.12)

$$f(v) = \sqrt{\frac{2}{\pi}} \frac{v^2}{a^3} \; e^{-\frac{v^2}{2a^2}}, \tag{6.12}$$

where a parameter a is defined as $a = \sqrt{\frac{k_B T}{m}}$, and has a dimension of velocity. The most probable speed is $\sqrt{2}\ a$, and the mean speed is $\sqrt{8/\pi}\ a$, which correspond to 1260 m/s and 1420 m/s at $T = 400$°C, and the percentage of atoms below those velocities is 43% and 53% respectively. A target velocity (maximum capurable velocity v_0) is limited by experiment parameters. For lithium, the most probable velocity v_p is already high ($\sim$ 1300 m/s) therefore the target velocity is usually lower than v_p which means that the percentage of slowed atoms is sensitive to the target velocity.- e.g., $P_{(v \leqslant 800 \text{ m/s})} = 15\%$, $P_{(v \leqslant 1000 \text{ m/s})} = 26\%$, $P_{(v \leqslant 1200 \text{ m/s})} = 39\%$. Since $B_0 = \frac{h}{\mu_B \lambda} v_0$, choosing 1200 m/s gives $B_0 \sim 1300$ G.

Choosing L_0: characteristic length and the safety factor η

When designing magnetic field profile of a Zeeman slower, it is important to keep the magnetic field gradient below the limit corresponding to the maximum deceleration $a_{\max}$. Furthermore, since the laser intensity is not infinite, it is limited by the effective maximum

deceleration $\eta_{\text{beam}} a_{\max}$. The condition to be $a < \eta_{\text{beam}} a_{\max}$ is[7]

$$\left|\frac{\mathrm{d}B}{\mathrm{d}z}\right| < \frac{h}{\mu\lambda v}\eta_{\text{beam}} a_{\max}. \tag{6.13}$$

There is a minimum characteristic length ${L_0}^{\min}$ for given target velocity because the acceleration cannot exceed $a_{\max}(= 1.8 \times 10^6\ m/s^2)$.

$${L_0}^{\min} = \frac{{v_0}^2}{2a_{\max}}. \tag{6.14}$$

For $B_0 = 1300\ G,\ {L_0}^{\min} = 0.41\ m$. From (6.5) and (6.14), equation (6.13) becomes

$${L_0}^{\min} \leqslant \eta_{beam} L_0 \tag{6.15}$$

η_{beam} is deceleration efficiency and is determined by the laser beam parameters.

$$\frac{s}{1 + s + 4\delta^2/\Gamma^2} \tag{6.16}$$

$\eta_{beam}$is typically greater than 0.8 therefore it is reasonable to assume that the characteristic length L_0 for Zeeman slower can be 0.5 m for $B_0 = 1300\ G$ case, which means the safety factor is about 0.83.

Bias magnetic field B_{bias}, laser detuning δ_L, and the beam intensity I_0

Bias field can be chosen for the convenient detuning to avoid disturbing 3D MOT($B_b = \frac{h}{\mu}\delta$). In idealized field profile, the positive bias field in decreasing field type Zeeman slower also act as setting parameter for exit velocity.

Laser beam detuning δ_L may not be necessarily the same as the detuning compensating the bias magnetic field. As will be shown in the simulation additional red detuning helps to control the steepness of deceleration without changing magnetic field gradient. In this case the overall laser detuning can be written as

$$\delta_L = \delta_{bias} + \delta_{rel}. \tag{6.17}$$

Laser beam intensity $I_0$is related to the deceleration efficiency η_{beam} by equation (6.16). Since the beam profile is Gaussian, the beam intensity at an off-centered site is weaker than the center; atoms in off-centered position experience less deceleration which may be improved by using a higher beam intensity.

[7]In general, η_{beam} is a function of r and z since the intensity of the laser beam has (ideally) a Gaussian profile.

B_0 [G]	1200	1300	1400
$v_{i,\max}$ [m/s]	1127	1221	1315
$L_{0,\min}$ [m]	0.3528	0.414	0.4802
$L_{0,\eta=0.8}$ [m]	0.441	0.5176	0.6002

Table 6.2: Test parameter range

6.2 Simulation Result

6.2.1 Bias magnetic field and laser beam parameters

After choosing parameters that can be easily determined by requirements (temperature, target initial velocity and length or safety factor), the rest parameters such as bias field, laser detuning and laser intensity are tested by a simulation; here, the transverse heating effect and randomness of dynamics of atoms during the cooling process are not included for the simplicity.

Table 6.2 shows a few examples of parameter choices. $v_{i,max}$ is the highest velocity of atoms that can be slowed by the Zeeman slower, and is determined by the magnetic filed magnitude B_0. In general, laser power not more than 20 mW is required to slow down atoms to 100-200 m/s of exit velocity. A slight red detuning ($\delta_{rel} \sim$ -100 to -200 MHz) makes slowing slope less steep so that atoms can exit the Zeeman slower at the end.

Figures 6.6, 6.7 and 6.8 show the phase-space trajectory with no bias, positive bias, and negative bias (spin-flip) magnetic field at the exit. The maximum speed of atoms being decelerated is the same for the three cases (the same magnetic field magnitude). As shown in the figure 6.6 when B_{bias}=0 G, for any choice of laser detuning, laser power or the length L, the velocity at the exit is not well defined because a decreasing field without bias magnetic field cannot be sharply off-resonant at the exit. For decreasing field with positive bias field (Fig. 6.7), a choice of B_{bias}=300 G and δ_{Laser}=+300 MHz($\delta_{rel} = -120$) works best for the same initial velocity groups. To compare with negative bias case (which can be called as spin-flip type Zeeman slower), the same magnitude of bias magnetic field is chosen (-300 G), but the relative detuning (δ_{rel}) is chosen to give a best shape for the given bias field (Figure 6.8). As shown in the figures 6.7 and 6.8, the velocity spread at the exit is very different for positive bias and negative bias cases. In the positive bias case, the lower velocity at the exit gets closer to the resonance as the atom being slowed and this results in spreading the exit velocity width, while the negative bias case it becomes more off-resonant as the lower velocity atom gets slowed. The estimated captured atom percentage is high for two cases(35 % for blue and 42 % for red detuning) and the mean exit velocities well below 200 m/s for both cases when transverse heating effect is not considered. Transverse heating can make it worse in terms of captured atom fraction and the mean velocity after the exit since some

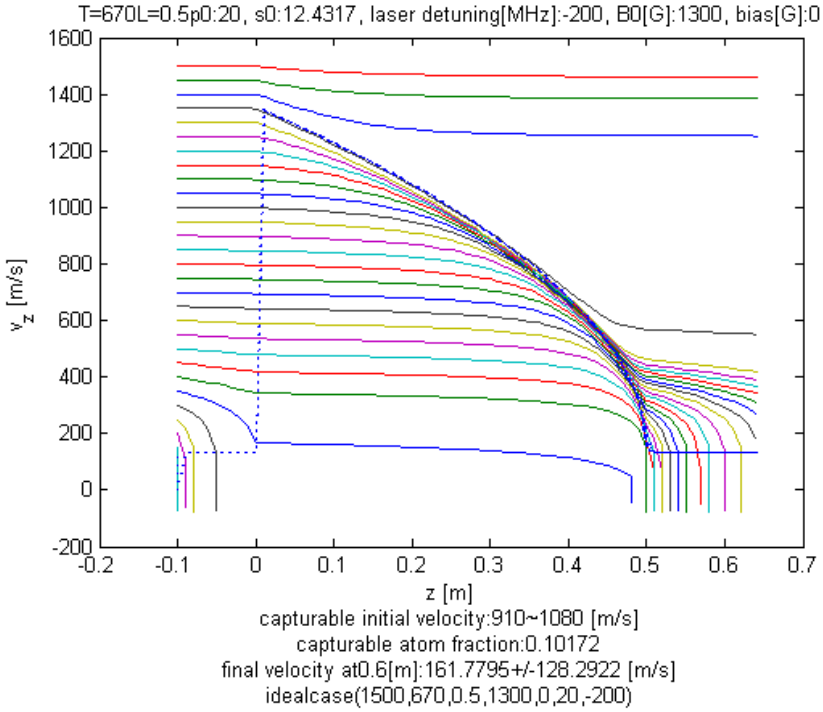

Figure 6.6: Typical output when B_{bias}=0 G. The capturable fraction is at best about 10 %

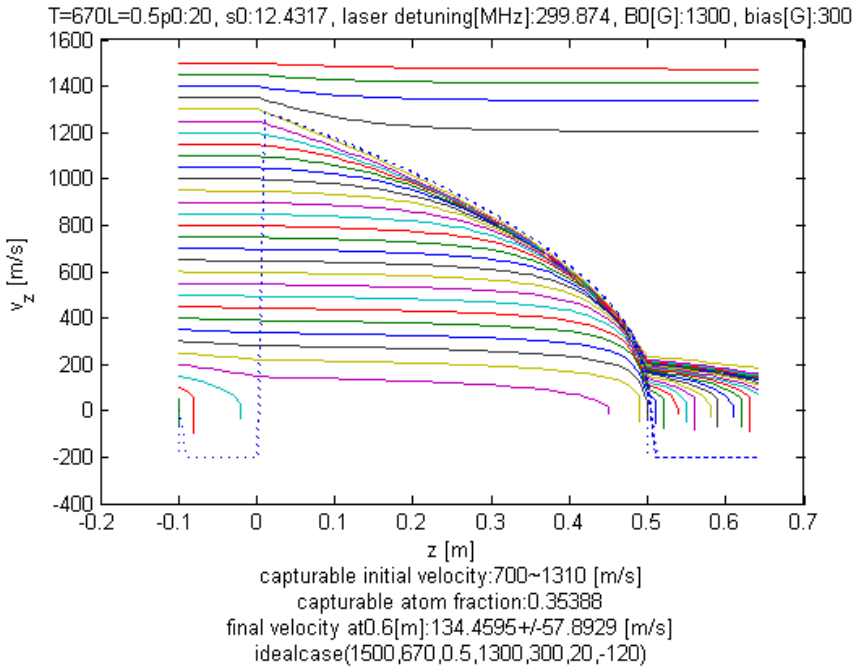

Figure 6.7: B_{bias}=300 G, δ_{Laser}= 300 MHz

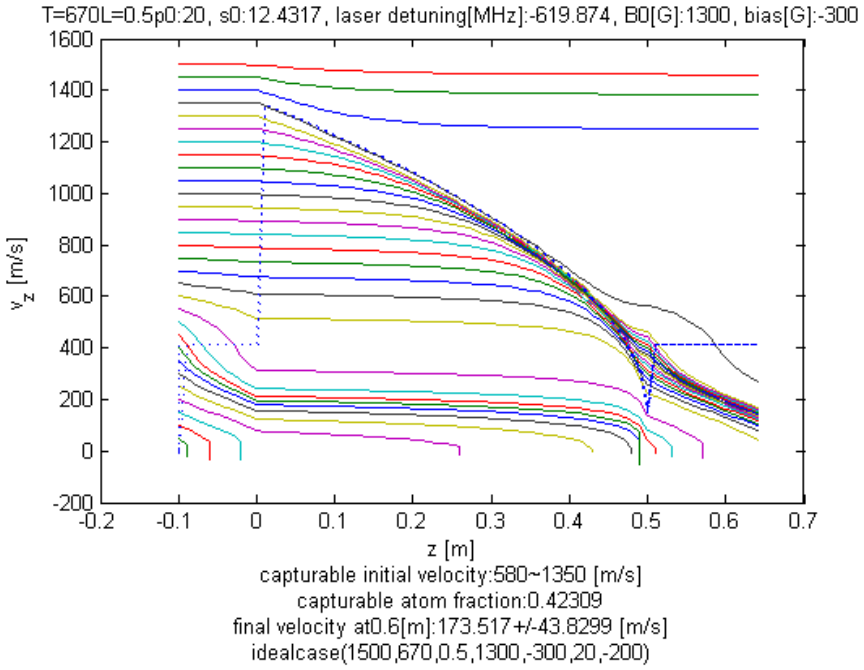

Figure 6.8: B_{bias}=-300 G, δ_{Laser}= -620 MHz

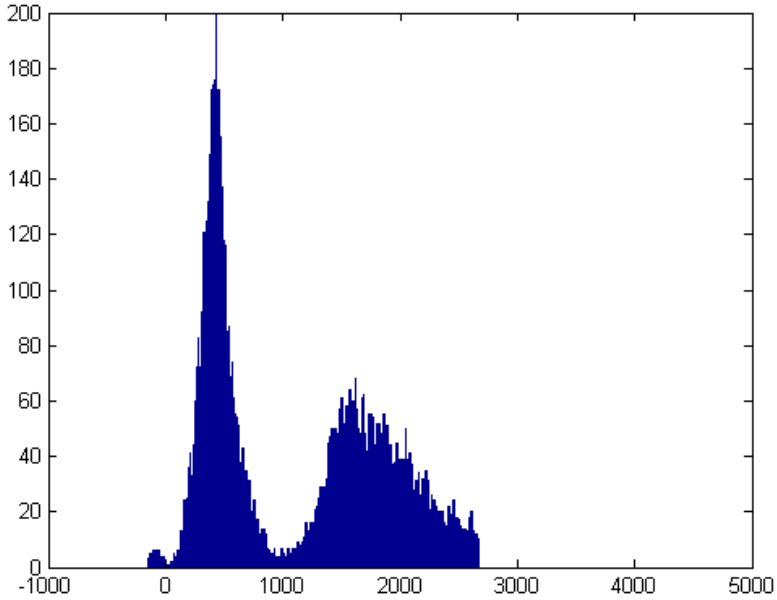

Figure 6.9: Exit velocity profile B_{bias}=300 G, δ_{Laser}= 300 MHz

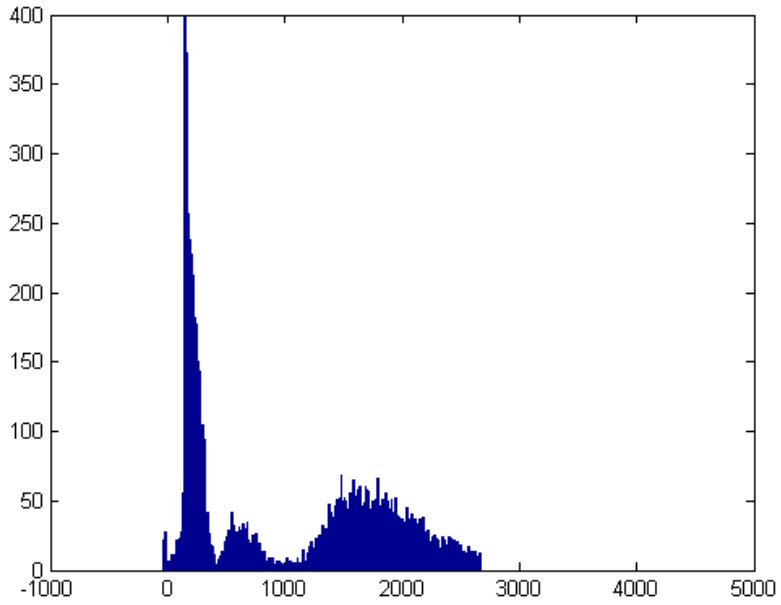

Figure 6.10: Exit velocity profile B_{bias}=-300 G, δ_{Laser}= -620 MHz

atoms can move out of the slower beam through the transverse motion. Figure 6.9 and 6.10 shows the result when the transverse heating effect is considered. The simulation is done for a pulsed mode operation (10^4 atoms in 5 ms duration), in the presence of a collimation before Zeeman slower, which gives input transverse velocity spread σ_{v_r}=5 m/s. [8] In figure 6.9, the mean velocity of the slowed atoms (narrow peak in the graph) is higher(centered around $v_{z,\text{exit}}$=420 m/s) than when transverse heating is not considered (130 - 170 m/s), while in the spin-flip case(red detuning, negative bias) the slowed atom velocity peak is narrower and has lower mean velocity(centered around $v_{z,\text{exit}}$=180 m/s). The reason why the cases with transverse heating have worse exit velocity spread and higher mean velocity is because atoms that are not at $r = 0$ get less deceleration and leave the slowing curve earlier so end up with high exit velocities. In the negative bias(red detuning) case the effect is less sever than positive bias(blue detuning) case because the resonance line at the exit is close to certain high velocity (400 m/s in this example) therefore it can still push those early left atoms towards the slowing curve.

6.2.2 Transverse heating and initial transverse velocity

Transverse heating due to random walk by spontaneous emission makes atoms spread during the cooling process [15]. There is another effect- free expansion, when an atom has initial

[8] Without collimation, the transverse velocity spread is bigger (σ_{v_r}= 15 m/s).

transverse velocity and spend time t inside a Zeeman slower the transverse displacement is greatly affected by the initial transverse velocity. To see the effect of transverse heating and initial transverse velocity, initial velocity is assumed to have a Gaussian distribution, and non-zero spatial distribution is assumed. When atoms are entering a skimmer from the oven, the distribution in radial position is uniform, and the transverse velocity distribution is a simply Gaussian distribution with $\sigma = v_{rms} = \sqrt{\frac{3k_BT}{m}}$. After the collimation it is reasonable to assume that the transverse velocity is still Gaussian, but with a reduced width $\sigma_{v_r} = d/l\ v_{rms}$ (Eqn. 6.18),

$$f(v_r) = \frac{1}{\sqrt{2\pi}\sigma_{v_r}} e^{-\frac{{v_r}^2}{2{\sigma_{v_r}}^2}}, \tag{6.18}$$

where l is the length and d is the inner diameter of the skimmer. The spatial distribution can be calculated by taking a spatial convolution of a uniform distribution (for the initial spatial distribution) and the Gaussian distribution (for the transverse velocity). The result is shown in Eqn.6.19.

$$f(r) = \frac{\mathrm{Erf}(\frac{d/2-r}{\sqrt{2}\,d\,s}) + \mathrm{Erf}(\frac{d/2+r}{\sqrt{2}\,d\,s})}{2\,d\,s(e^{-\frac{1}{2s^2}} - 1)\sqrt{\frac{2}{\pi}} + 2\,d\,\mathrm{Erf}(\frac{1}{\sqrt{2}\,s})}, \tag{6.19}$$

where the new parameter s is a dimensionless quantity representing a ratio of the rms displacement $\sqrt{r^2}$ to the skimmer diameter d.

$$\sqrt{r^2} = \sigma_{v_r}\bar{t} = d\ s \tag{6.20}$$

Figure. 6.11 shows simulation results for σ_{v_r} = 0, 5, 10, 15 m/s with both positive and negative bias $B_{bias} = +300, -300$ G. In (a) and (b), the initial transverse velocity is frozen at $v_r = 0$ yet initial radial position distribution has the same form defined in equation (6.19). Those are not physical cases, but it is convenient too isolate the only the transverse heating due to scattering (pure random walk) from an effect due to the initial transverse velocity. The result shows that initial collimation greatly affects the shape of the exit velocity profile, and that the result of negative bias is in general better than that of positive bias. For $\sigma_{v_r} > 10$ m/s, the exit velocity profile suffer severely from the transverse heating thus the capturable atom fraction is smaller.

Table (6.3) shows the number of captured atoms, hot atoms and lost atoms for σ_{v_r} = 0, 5, 10, 15 m/s and $B_{bias} = \pm 300$ G, with an initial atom number of 10000. Captured atoms are ones that arrived at $z \geq 0.6$ m with the exit velocity of $0 < v_z \leq 200$ m/s, hot atoms refer to atoms with $z \geq 0.6$ m and $v_z > 200$ m/s, and the rest is lost either inside or outside the Zeeman slower. Pure random walk effect when initially $v_r = \sigma_{v_r} = 0$ m/s shows still good capture percentage $30 \sim 40\%$ compared to the result without random walk. It means that captured atom fraction is very sensitive to the initial transverse velocity width σ_{v_r} than to random walk effect itself. Without additional collimation $\sigma_{v_r} = 15$ m/s gives only $6 \sim 7\%$ of atoms captured. Therefore further collimation(smaller σ_{v_r}) using optical molasses or 2D MOT will help to have better atom number at the exit.

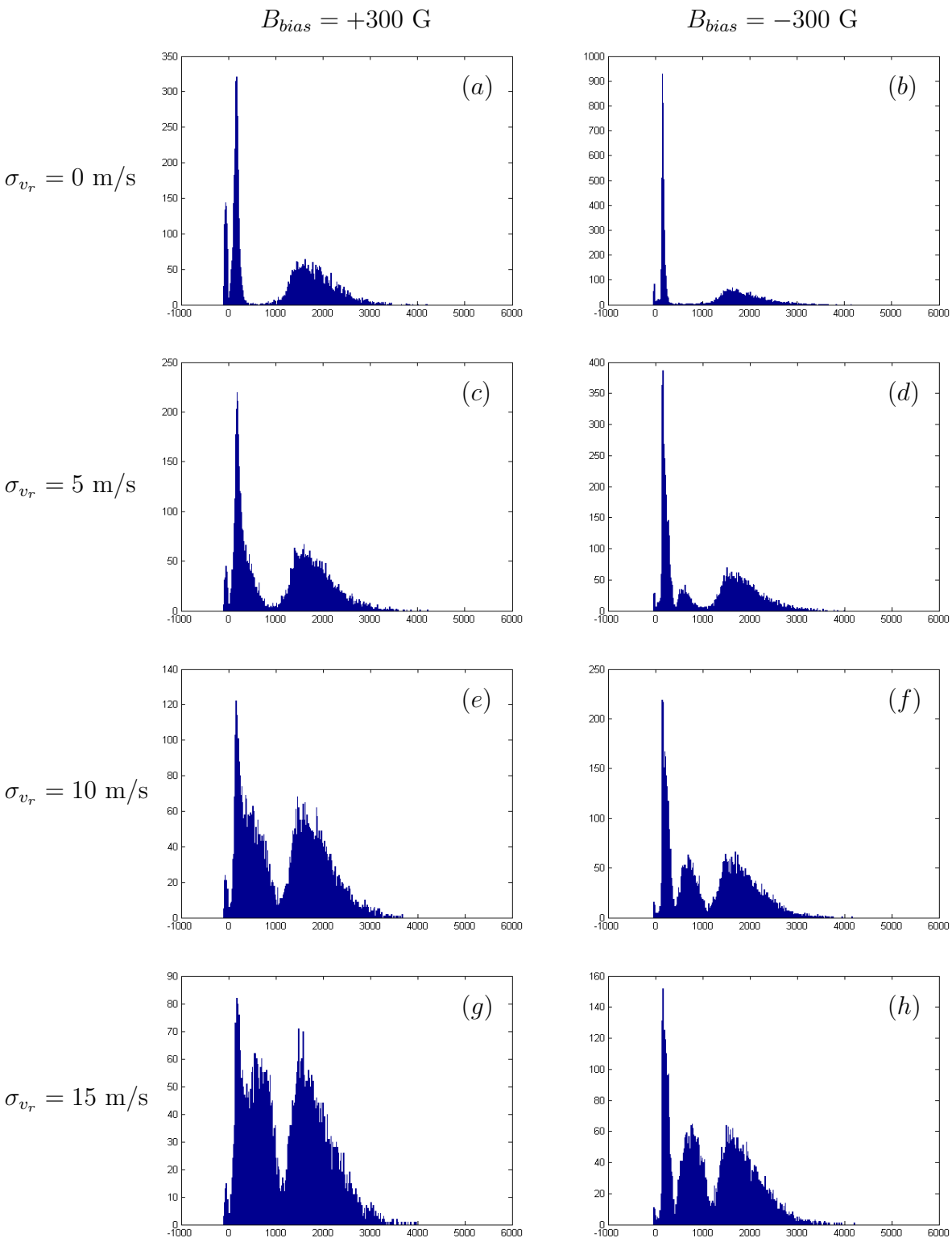

Figure 6.11: Exit velocity profile dependence on initial transverse velocity width

N=10000	Captured		Hot		Lost	
σ_{v_r} [m/s]	+300 G	-300 G	+300 G	-300 G	+300 G	-300 G
0	2752	3900	6220	5841	1028	259
5	1563	1916	7933	7586	504	498
10	896	1085	7752	7596	1352	1319
15	599	710	6876	6831	2525	2459

Table 6.3: Atom number counting for various σ_{vr} for $B_{bias} = \pm 300$ G.

6.3 Magnetic Coil Design

Once the magnetic field parameters are chosen by simulations, number of coil windings and current are determined such that the resulting magnetic field resembles the ideal magnetic field. Our Zeeman slower frame (Figure 6.12) has 8 sections divided by seven copper disks (1/8" thick, 6" wide) and has a water cooling unit which water runs between 1" OD stainless steel tube and 1.375" OD copper tube. The seven copper disks are welded on the the copper tube and each disk has one cut with smooth wedge for coil escape. At the both ends of the frame, there are 2 copper disks with spiral copper tubing (1/4" OD) on the outer side which has inlet and outlet for water circulation. Each section has of 6 cm between wall, the total length of coil winding region is 50.8 cm. In each section 14 AWG solid round copper wire will be wound for slot and bias field separately[9]. To generate B_0=1300 G and B_{bias}=300 G, bias coil layer $n_{y,b}$=6, slot coil layer n_y= [18,16,15,12,11,9,7,3] is wound[10] with current $I_b = 8$ A, $I_s = 10$ A, where B_{bias} becomes 335 G and $B_0 \sim 1300$ G according to the calculation result (Figure 6.13). With the same condition the power consumption is estimated which gives 1860 and 3458 windings for bias and slot coils which has lengths of 249 m and 802 m, resistance of 2.40 Ω and 7.73 Ω, require supply voltage 19.2 V and 77.3 V, and power 153.5 W and 773.5 W respectively. The resistivity is assumed conservatively as $2.5 \times 10^{-8} \Omega m$ whereas pure bare copper resistivity at 20°C is $1.68 \times 10^{-8} \Omega$m [6]. The magnet coil is 14 AWG round solid copper wire with double Ployester-amide-imide coating (APT) coating[11]. Actual measurement on resistance of one spool of the coil which is 4020 m long gives 10.8 Ω whereas it is higher than ideal pure copper case(8.2 Ω) but lower than the conservative estimation (12.3 Ω). Assuming that the wire temperature is at 100°C and using the temperature coefficient of copper $\alpha = 3.9 \times 10^{-3}$, resistance for bias and slot coil are 3.1 Ω and 10 Ω, require supply voltage of 25 V and 100 V, power of 200 W and 1 kW. Our power supply Agilent N5769A/J01 can generate 100 V, 10 A and used to supply the current through the slot coil.

[9]For more flexibility coils can be wound such that independent current control is possible.

[10]The calculation is done for $a = d$ packing, therefore may not be exact, also the number of windings per layer can be a little different

[11]NEMA MW35-C rated, good for up to 200°C.

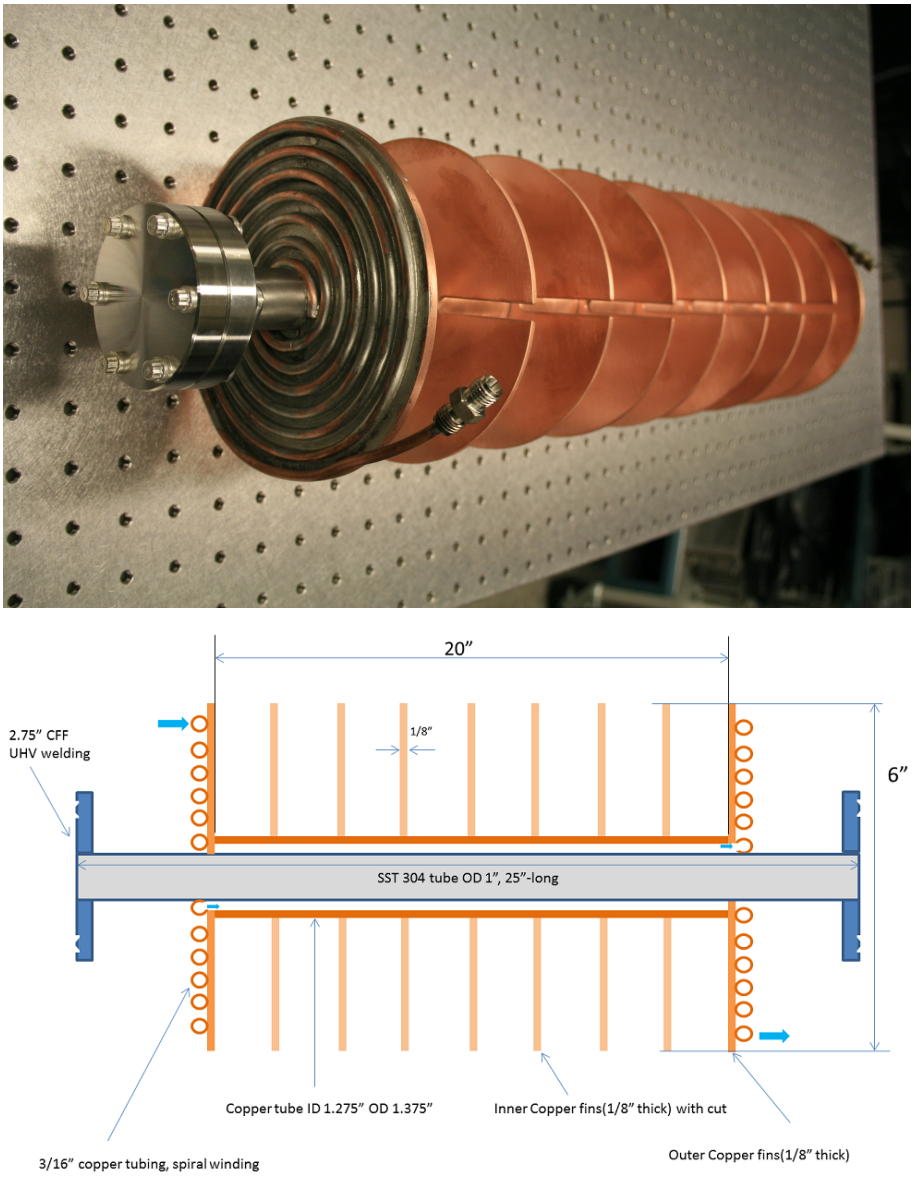

Figure 6.12: Zeeman slower frame

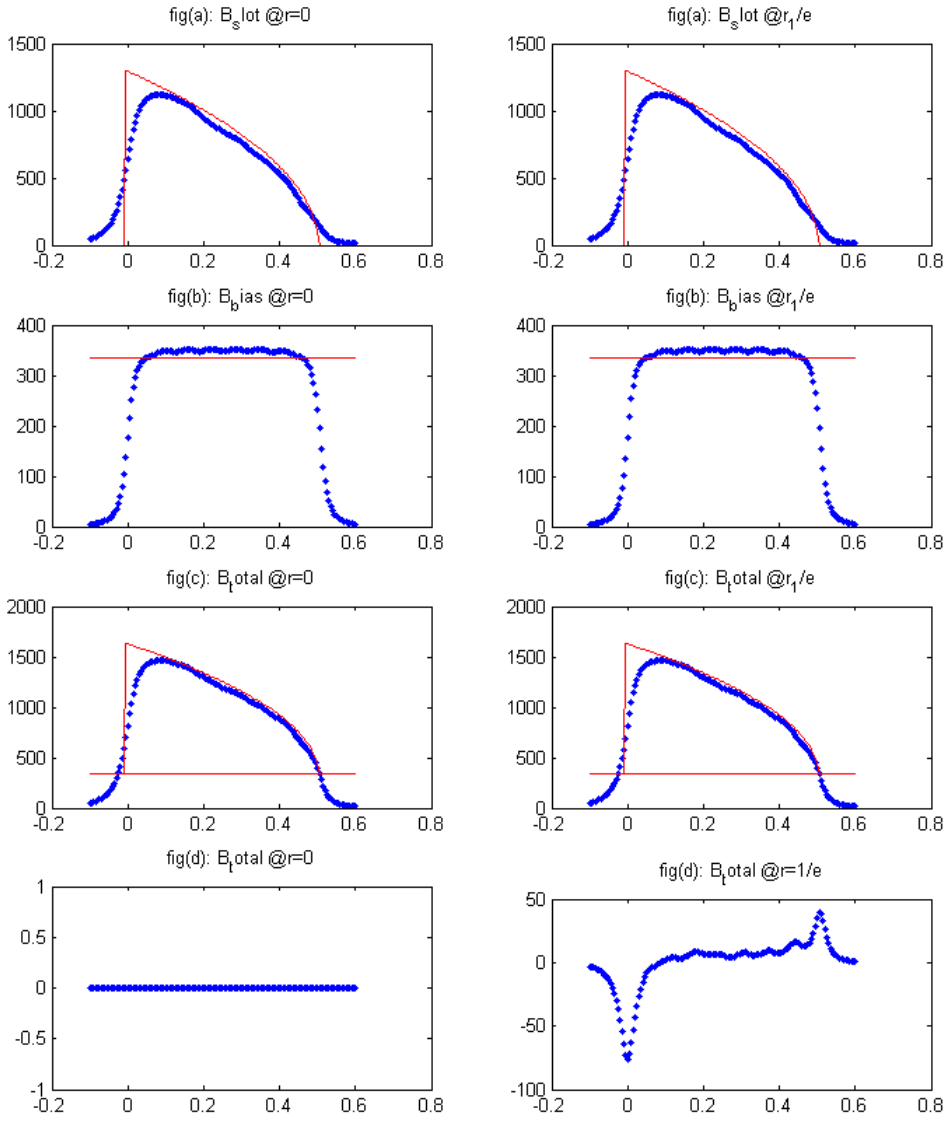

Figure 6.13: Realistic magnetic field B_z at $r = 0$ and $r = r_{1/e}$

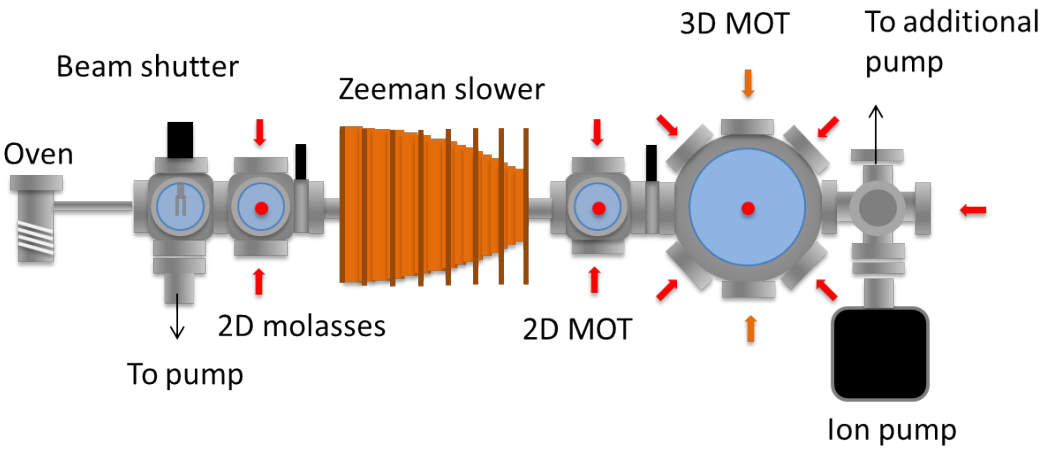

Figure 6.14: Zeeman slower setup plan

6.4 Result summary

To improve the number of atoms in the MOT, we designed a Zeeman slower with 2D MOT/molasses. Zeeman slower can provide the highest atom flux to date, however it requires an engineering effort to have a good performance. We have modeled a Zeeman slower, run a Monte Carlo simulation and identified that a spin-flop type Zeeman slower with 50 cm length and a magnetic field of 1300 G magnitude and a -300 G bias, and with the moderate laser intensity $s_0 = 12.4$ (at 20 mW power) and red detuning $\delta_{Laser} = -620$MHz, works best for our need. To avoid heating and expanding in transverse direction, 2D molasses and 2D MOT are added before and after the Zeeman slower stage as shown in Fig. 6.14.

Chapter 7

Atom interferometer

7.1 Atom interferometer types and beam splitters

There are many different types of atom interferometers [69], among which the Mach-Zehnder type and the Ransey-Bordé types are most common. As shown in Fig. 7.2, Mach-Zehnder interferometer (MZI) consists of two $\pi/2$-pulses and a π- pulse in between the two, Ramsy-Bordé interferometer (RBI) consists of four $\pi/2$-pulse beam splitters [86] thus can form a conjugate interferometer consisting of two RBIs.

In an atom interferometer the laser pulses act as diffraction gratings. The light pulses transfer a momentum to an atom with a probability. In the Bloch picture of the two level system, a $\pi/2$ pulse transfer atoms in the one state to the superposition state of the two states with the equal weight therefore a $\pi/2$ pulse acts as a beam splitter. Similarly a π pulse acts as a mirror in an atom interferometer. There are many different techniques to make a beam splitter [69], among which the Raman beam splitter and the Bragg beam splitter are the most common.

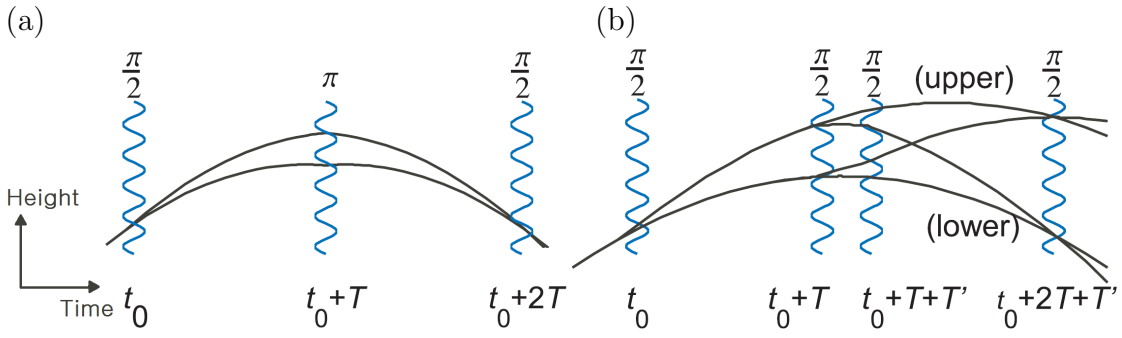

Figure 7.1: Types of atom interferometer. (a) Mach-Zehnder, (b) conjugate Ramsey-Borde. Figures adopted from [77]

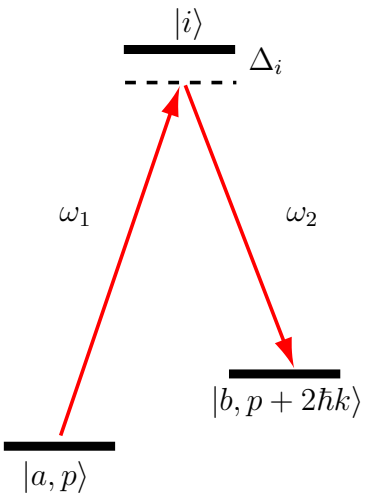

Figure 7.2: Schematics of a Raman beam splitter with $2\hbar k$ momentum transfer ($2\hbar k = \hbar k_1 + \hbar k_2$).

A Raman beam splitter uses a Raman transition between the two ground hyperfine states, thus an atom changes its internal state when deflected by the beam splitter [87]. The effective Rabi frequency for Raman transition is determined by

$$\Omega_{\text{eff}} = \sum_i \frac{\Omega_{1,i}\,\Omega_{2,i}^*}{2\Delta_i}, \tag{7.1}$$

where i is an intermediate state index.

A Bragg beam splitter uses Bragg diffraction of an atom matter-wave by an optical lattice. Unlike in a Raman beam splitter, an atom's internal state does not change in a Bragg beam splitter. The effective Rabi frequency for n^{th} order Bragg diffraction in the long pulse regime is given by [88]

$$\Omega_{\text{n,eff}} = \frac{\Omega^n}{(8\omega_r)^{n-1}[(n-1)!]^2}, \tag{7.2}$$

where Ω is the two-photon Rabi frequency defined as

$$\Omega = \frac{\Omega_0^2}{2\Delta}. \tag{7.3}$$

In an atom interferometer, the phase difference between the two paths is the sum of the free evolution phase difference and the laser phase difference

$$\delta\phi_{\text{tot}} = \delta\phi_{\text{free}} + \delta\phi_L. \tag{7.4}$$

The free evolution phase difference $\delta\phi_{\text{free}}$ of the atom's matter-wave is given by integrating over the enclosed path of the Lagrangian L

$$\begin{aligned} \Psi(t) &= \Psi(0)e^{\frac{i}{\hbar}\int_{\text{path}} L\,dt}, \\ \delta\phi_{\text{free}} &= \frac{1}{\hbar}\oint_{\text{path}} L\,dt. \end{aligned} \tag{7.5}$$

Laser phase difference is the laser phase gained by the upper path minus the laser phase gained by the lower path. For $2n\hbar k$ momentum transfer, the phase difference of a MZI becomes [85, 77]

$$\begin{aligned} \phi_{\text{MZ}} &= 2nkgT^2 + n\phi_L, \\ \phi_L &= 2\phi_2 - \phi_1 - \phi_3, \end{aligned} \tag{7.6}$$

and the phase difference of a RBI becomes [77]

$$\begin{aligned} \phi_{\text{RB}} &= \pm 8n^2\omega_r T + 2nkg(T+T')T + n\phi_L, \\ \phi_L &= \phi_2 - \phi_1 + \phi_3 - \phi_4. \end{aligned} \tag{7.7}$$

The $\pm$ signs in the expression of ϕ_{RB} are for the upper (+) and the lower (-) RB interferometers in the Fig. 7.2 (b). This suggests that a RBI can measure a recoil frequency ω_r by taking the differential signal from the two ports.

For our purpose, a simple MZI can be used to measure gravitational acceleration of lithium atoms. As mentioned, there are many choices for a beam splitter, however a beam splitter using a $2\hbar k$ Raman transition is easier to achieve than other types of beam splitters. The next section will discuss our Raman beam frequency setup.

7.2 Interferometer beam frequency setup

To generate the frequencies for a Raman beam splitter for a simple interferometer, we use an electro-optic modulator with a modulation frequency at 401.5 MHz. We achieved an EO modulation index of 2.40 such that the carrier frequency component is suppressed while the two first order sidebands separated by the ground hyperfine energy splitting (803 MHz) are maximum. By switching on and off the EOM, we can switch between the interferometer beam and the lattice cooling beam. The interferometer beam frequency generating setup is shown in Figure 7.3. Our EO crystal is lithium tantalate ($LiTaO_3$) which properties are shown in Table 7.1.
For EO crystals with $3m$ symmetry such as $LiNbO_3$ and $LiTaO_3$, the modulation index β is given by [16]

$$\beta = \frac{\omega}{c} l(n_o^3 r_{13} - n_e^3 r_{33})\frac{V_m}{d}, \tag{7.8}$$

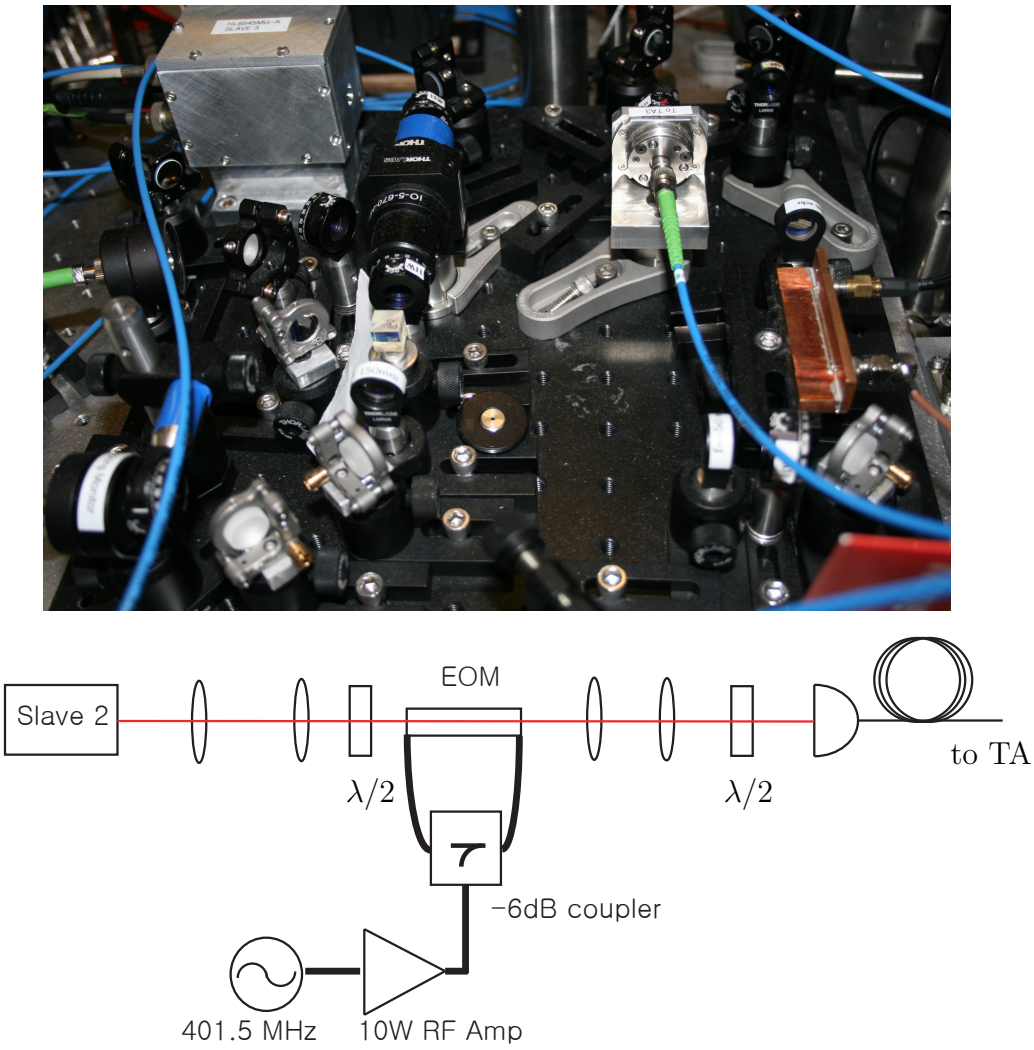

Figure 7.3: Interferometer beam EO setup.

Property	Symbol	Value
Index of refraction	n_o	2.176
	n_e	2.180
Electro-optic coefficients	r_13	7.5
	r_{33}	33
	r_{51}	20
	r_{22}	1

Table 7.1: Properties of lithium tantalate crystal at λ= 633 nm when modulated in the high frequency regime (RF). Values from [16]

where ω is the laser frequency in vacuum, l is the EO crystal length, and V_m is the amplitude of the modulation voltage across the crystal with the travel distance d. As a result of an EO phase modulation, the electric field of the light through EO becomes

$$\begin{aligned} E' &= E_0 \exp\left[i(\omega t + \beta \sin \omega_m t)\right] \\ &= E_0 \sum_{n=-\inf}^{\inf} J_n(\beta) e^{i(\omega + n\omega_m)}, \end{aligned} \tag{7.9}$$

where the J_n is the Bessel function. We use 401.5 MHz modulation frequency and obtain two first sidebands which frequency separation is about the ground hyperfine splitting. To make the carrier band vanish the modulation index needs to be the first zero of the J_0, $\beta \approx 2.40$. Our EO is 5 cm long and has 1.2 mm $\times$ 1.2 mm square-shape cross section. Our EO and connectors designed to form a 50 Ω transmission line. Using Eq. (7.8) and values, the required voltage becomes about 77 V. To get this RF power we use 10 W RF amplifier, and the RF is coupled using a -6 dB coupler which results in the energy loss of 25 % on each path. The RF power circulates in the loop similarly to the ring cavity, thus a very high modulation index can be achieved with our setup.

7.3 Plans for a ^{7}Li-^{6}Li dual atom interferometer

Once we achieve a ^{7}Li atom interferometer, we plan to extend to a ^{7}Li-^{6}Li dual atom interferometer which can test the Einstein equivalence principle by simultaneously measuring the accelerations of both isotopes. As mentioned in section 1.2, ^{7}Li-^{6}Li atom interferometer is advantageous for testing EEP. However a difficulty comes from the spectroscopic properties of the lithium isotopes. Although it is convenient that only one laser is needed to address transitions for both ^{7}Li and ^{6}Li, it is troublesome when cooling both isotopes together since the D1 transition of ^{7}Li and the D2 transition of ^{6}Li overlaps. A dual MOT of ^{7}Li-^{6}Li has been successfully demonstrated, yet the number of ^{6}Li atoms are about a thousand smaller than that of ^{7}Li atoms due to its smaller natural abundance and limited loading time in MOT to avoid interfering with ^{7}Li transition [95]. Using a high-flux Zeeman slower and an enriched ^{6}Li source the number of ^{6}Li atoms can improve. The same problem exists for interferometer beam frequencies, however by choosing the frequencies near D2 of ^{7}Li for the ^{7}Li AI and near D1 of ^{6}Li for the ^{6}Li AI, this effect can be negligible.

As shown in Fig. 7.4, in a ^{7}Li-^{6}Li dual atom interferometer with MZ configuration, the pathes for ^{7}Li and ^{6}Li atoms do not overlap exactly, since their recoil velocities are different. This leads to a systematic effect due to the gravity gradient which can be as large as $10^{-13}g$ for a pulse separation time $T = 1$ s and a momentum transfer $p = 2\hbar k$. This causes a problem when we aim to measure the gravitational acceleration with the precision of $10^{-14}g$. Nevertheless, the systematic effect can be eliminated by a good apparatus design which can cancel a gravity gradient. For example, consider a sphere with a vertical narrow channel,

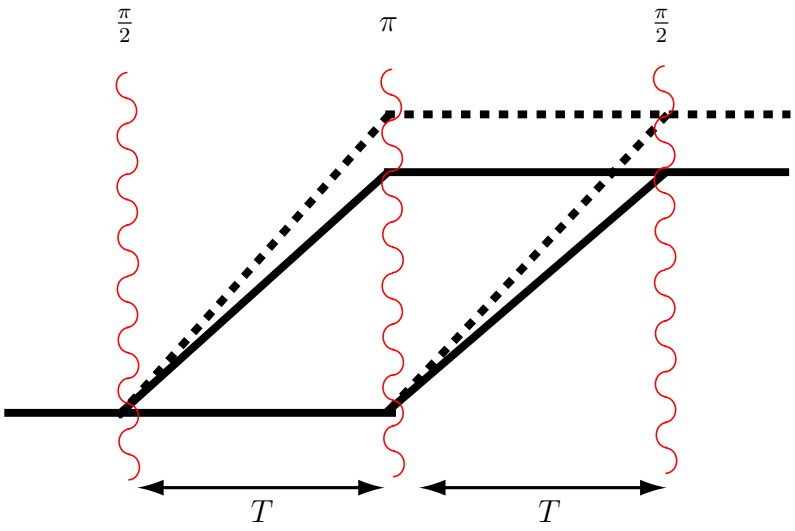

Figure 7.4: ^{7}Li-^{6}Li dual atom interferometer in MZ configuration. Solid line represents the path of a ^{7}Li atom and dotted line represents the path of a ^{6}Li atom. Gravity is ignored in the trajectories for the graphical simplicity.

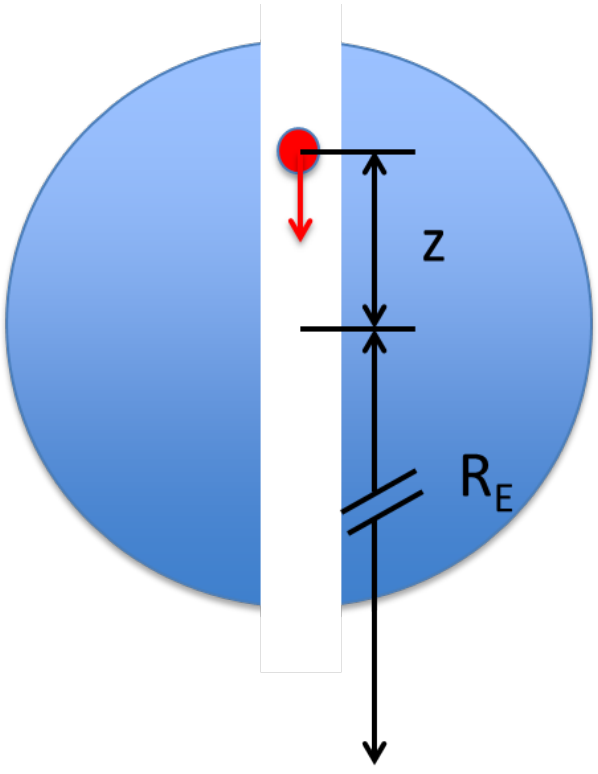

Figure 7.5: Gravity gradient canceling using a sphere mass.

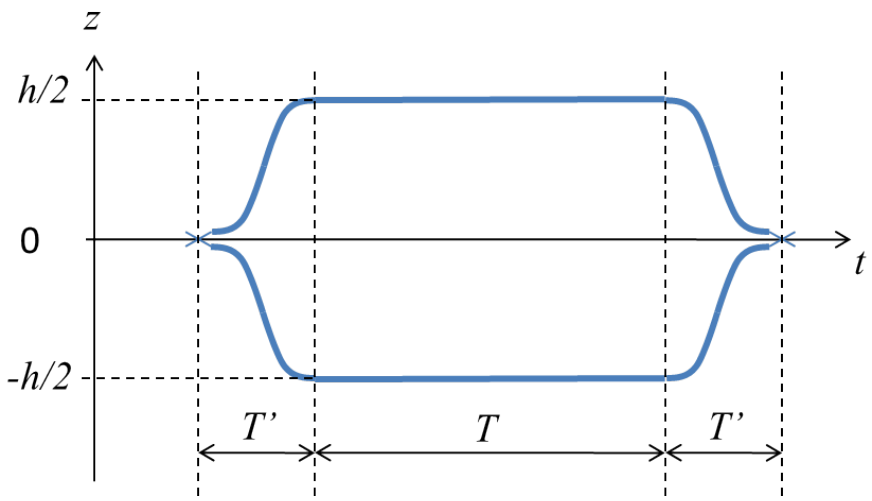

Figure 7.6: Lattice atom interferometer.

where atoms can freely move along (Fig. 7.5). The force between the Earth and an atom is given by

$$F_{\text{Earth-atom}} = -\frac{GM_{\text{E}}m_{\text{a}}}{R_{\text{E}}^2} + 2\frac{GM_{\text{E}}m_{\text{a}}}{R_{\text{E}}^3}z + \cdots, \tag{7.10}$$

where the second term proportional to z is the gravity gradient force. The force between the added sphere and the atom is given by

$$F_{\text{sphere-atom}} = -\frac{4\pi}{3}\rho_{\text{s}}m_{\text{a}}z, \tag{7.11}$$

which has the opposite sign to the gravity gradient force. This suggests that the systematic effect from the gravity gradient can be eliminated by choosing appropriate density ρ_{s} of the sphere object.

A Raman beam interferometer with $2\hbar k$ momentum transfer has a small enclosed space-time area, thus has a lower sensitivity than desired. For example, recalling Eq. 1.4, a lithium atom interferometer with $2\hbar k$ momentum transfer, a pulse separation of $T = 50$ ms, $N = 10^6$ atoms, and 1 day integration time gives a shot-noise limited sensitivity of about $10^{-11}g$ which is quite bigger than our goal (10^{-14}). Bragg beams can be used to achieve a large momentum transfer as large as $n = 100$. Since $\Delta\phi = 2nkgT^2$ in MZI, it is more efficient to increase the separation time in MZ which does not work well for freely expanding lithium atoms.

Much bigger phase difference $\Delta\phi$ can be achieved when an optical lattice holds atoms for a long time after the two interferometer arms split by beam splitters (Fig. 7.6). In this case, the phase difference between the two paths is approximately

$$\Delta\phi \approx \frac{m}{\hbar}gh(T + T'). \tag{7.12}$$

With $T \sim 2$ s, $h = 2$ cm, $N = 10^6$ atoms, and 1 day integration time, the shot-noise limited sensitivity of about $10^{-14}g$ can be achieved.

Chapter 8

Conclusion

An atom interferometer is a great tool for precision measurement. Using an atom interferometer, a precise measurement of the gravitational accelerations experienced by the two falling objects can be done for the test of the Einstein equivalence principle (EEP). A measurement sensitivity better than 10^{-14} has a significant scientific importance since the current best measurement limit is at 10^{-13}, and also the new result can test the validity of various models and theories of fundamental physics. We have identified that choosing the two lithium isotopes (^{7}Li and ^{6}Li) as test masses has an advantage for the test of EEP, according to the standard model extension (SME). We aim to build the world's first lithium atom interferometer and test the Einstein equivalence principle.

To build a high sensitivity lithium atom interferometer, we developed a new cooling method for lithium as well as designed and built a better apparatus. Since the more atoms, the better the signal to noise ratio of an atom interferometer, it is important to get a lower temperature and more atoms in the trap which can coherently contribute in an atom interferometer.

Due to its physical and spectroscopic properties, a lithium atom is more difficult to laser cool compared to other alkali atoms. For this reason an evaporative cooling is typically used to reach a low temperature with lithium atoms. However the evaporative cooling has a low efficiency (0.01 %), thus is not suitable for atom interferometry. We demonstrate a new laser cooling method suitable for building a lithium atom interferometer. We obtained a sub-Doppler cooling of lithium using a simple optical lattice. Our method has a very high cooling efficiency $\sim$ 50 %, which may be improved more, and gives a temperature ($T \approx 7 - 8T_r$) low enough for an atom interferometer. Also our new cooling method is robust in that it works for a broad parameter range, and is very convenient to set up since it does not require complicated magnetic traps or high power lasers as in other cooling methods.

We identified and experimentally confirmed that the cooling works as a combination of Sisyphus cooling and adiabatic cooling. The cooling temperature depends mainly on the potential depth and the frequency detuning, but also is affected by other factors such as the

initial temperature (CMOT temperature), holding time in the lattice, the residual magnetic field, and the lattice alignment. The final temperature by Sisyphus and adiabatic cooling is as low as 40 μK in 1D lattice, and the cooling efficiency is as high as 50 %. When the lattice is switched off faster than the adiabacity condition, only Sisyphus cooling mechanism works and gave 100 μK in 1D. In the 3D lattice, lattice geometry was not a stable 3D lattice, thus adiabatic cooling did not work efficiently yet Sisyphus cooling worked and gave a final temperature of 100 μK. We expect to get a lower cooling temperature in 3D once the 3D optical lattice geometry is improved.

It is beneficial to have more atoms in the trap, not only for a better signal to noise ratio but also for possible use of techniques such as velocity selection which helps to increase the atom interferometer contrast. With our current setup, the number of atoms cooled by the lattice is on the order of $10^7 \sim 10^8$, and is limited by the current MOT system design, which may be improved by better atom source design, increasing the laser power and bigger magnetic field. Among the factors to be improved, the biggest gain on the atom number can be achieved by designing a high-flux atom source. We designed a Zeeman slower-2D MOT hybrid lithium atom source which can perform better than just 2D MOT or Zeeman slower. By Monte Carlo simulation, we identified optimal conditions for a spin-flip type Zeeman slower. The optimal design has a 50 cm length, a magnetic field of 1300 G magnitude and a -300 G bias, the moderate laser intensity $s_0 = 12.4$ (at 20 mW power) and red detuning $\delta_{Laser} = -620$MHz. With those parameters the Zeeman slower can slow down atoms whose mean speed is slowed from 1420 m/s to 180 m/s. The number of atoms that can be captured finally in 3D MOT depends not only on the exit speed but also on the expansion of atoms in the transverse direction. To avoid the heating and expansion in the transverse direction, 2D molasses and 2D MOT are added before and after the Zeeman slower stage. By implementing this design, the number of atoms trapped in the MOT can increase potentially to one or two orders of magnitude.

Currently we are building an atom interferometer using ^{7}Li. For a beam splitter to try initially, we choose to use a $2\hbar k$ Raman beam splitter since it is the simplest and easier to achieve compared to other beam splitters such as Bragg beam splitter. We have set up an RF ring cavity using an EOM to generate Raman beam frequencies. The atom interferometer is Mach-Zehnder type in order to measure gravitational acceleration of ^{7}Li (See section 7.1 for details). With a fountain type MZI using a Raman beam splitter ($p = 2\hbar k$), we expect to get the shot-noise-limited sensitivity of 10^{-11} with a pulse separation time of 50 ms, integrated over a day. In principle, the sensitivity of a fountain type MZI improves quadratically with the pulse separation time T, which suggests that a pulse separation of more than 1 s can lead to a shot-noise-limited sensitivity as good as 10^{-14}. However it is difficult to achieve such a long pulse separation time for a lithium atom interferometer because of the large recoil velocity of the atom. The fast atom cloud expansion due to its large recoil velocity makes a fountain type atom interferometer not suitable for a high sensitivity lithium atom interferometer. To overcome this difficulty, we plan to confine lithium atoms in a moving

optical lattice as they move with a momentum transferred by the beam splitter pulses. We expect that the lattice atom interferometer design will be able to keep the separation time long enough to reach a sensitivity of better than 10^{-14}. For example, a shot-noise-limited sensitivity of $10^{-14}g$ can be obtained when the holding time is 2 s and the height is about 2 cm (Fig. 7.6).

To test the Einstein equivalence principle we plan to build a ^{7}Li-^{6}Li dual atom interferometer. Despite the fact that the D1 transition of ^{7}Li and D2 transition of ^{6}Li overlap, a dual MOT of ^{7}Li and ^{6}Li works well by avoiding or limiting the time in these transitions. For a Raman beam splitter, frequencies close to ^{7}Li D2 and ^{6}Li D1 may be used to avoid the transition overlap problem. As discussed earlier, practically, a simple MZ atom interferometer with $2\hbar k$ momentum transfer cannot reach the goal sensitivity $\sim 10^{-14}g$ thus a different interferometer scheme is needed; the lattice atom interferometer design has a potential to reach this goal. For a ^{7}Li-^{6}Li simultaneous lattice atom interferometer, the gravity gradient ($\sim 10^{-13}g$) due to the different recoil velocities of the two isotopes can be canceled by using a sphere mass as shown in section 7.3. Other systematic effects due to mean-field shift, tides, and missed recoils are below $\sim 10^{-14}$ level.

Appendix A

Matrix elements of ^{7}Li and ^{6}Li

^{7}Li, D_1

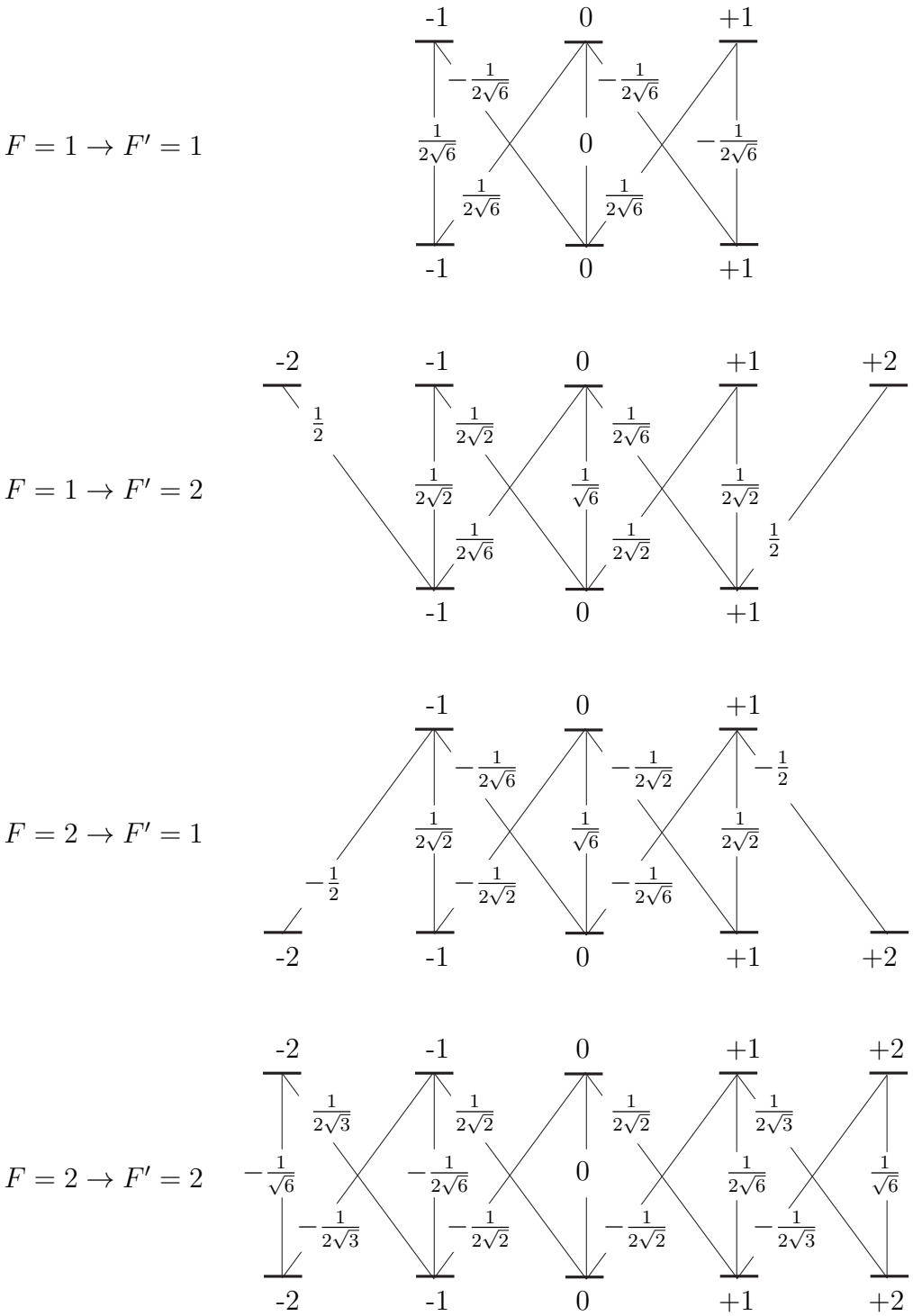

Figure A.1: ^{7}Li D1 transition matrix elements in units of $\langle J' || \boldsymbol{\mu}(D1) || J \rangle = -\sqrt{2}\, e a_\mathrm{o}$

^{7}Li, D_2

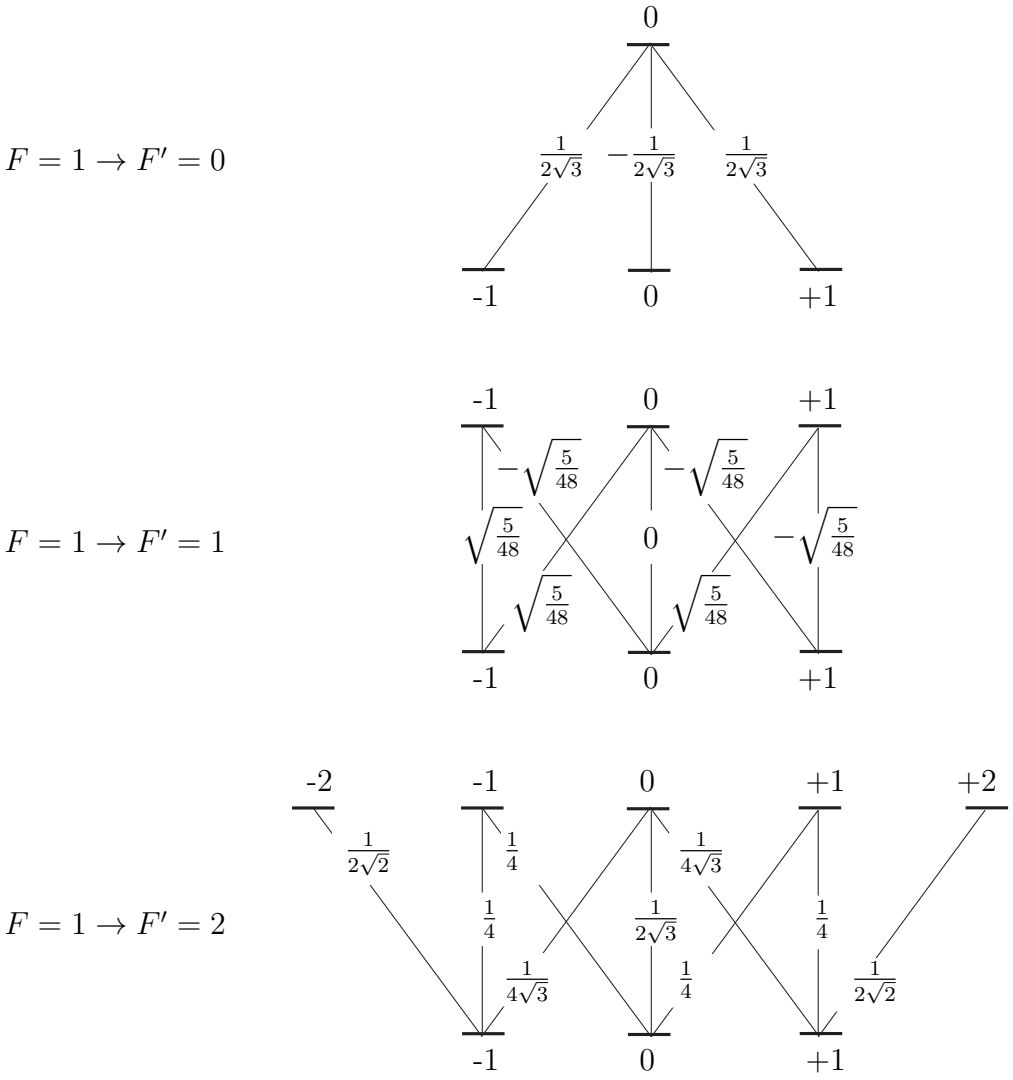

Figure A.2: ^{7}Li D2 transition matrix elements ($F = 1 \rightarrow F'$) in units of $\langle J'||\boldsymbol{\mu}(D2)||J\rangle = 2\, ea_o$

^{7}Li, D_2 - continued

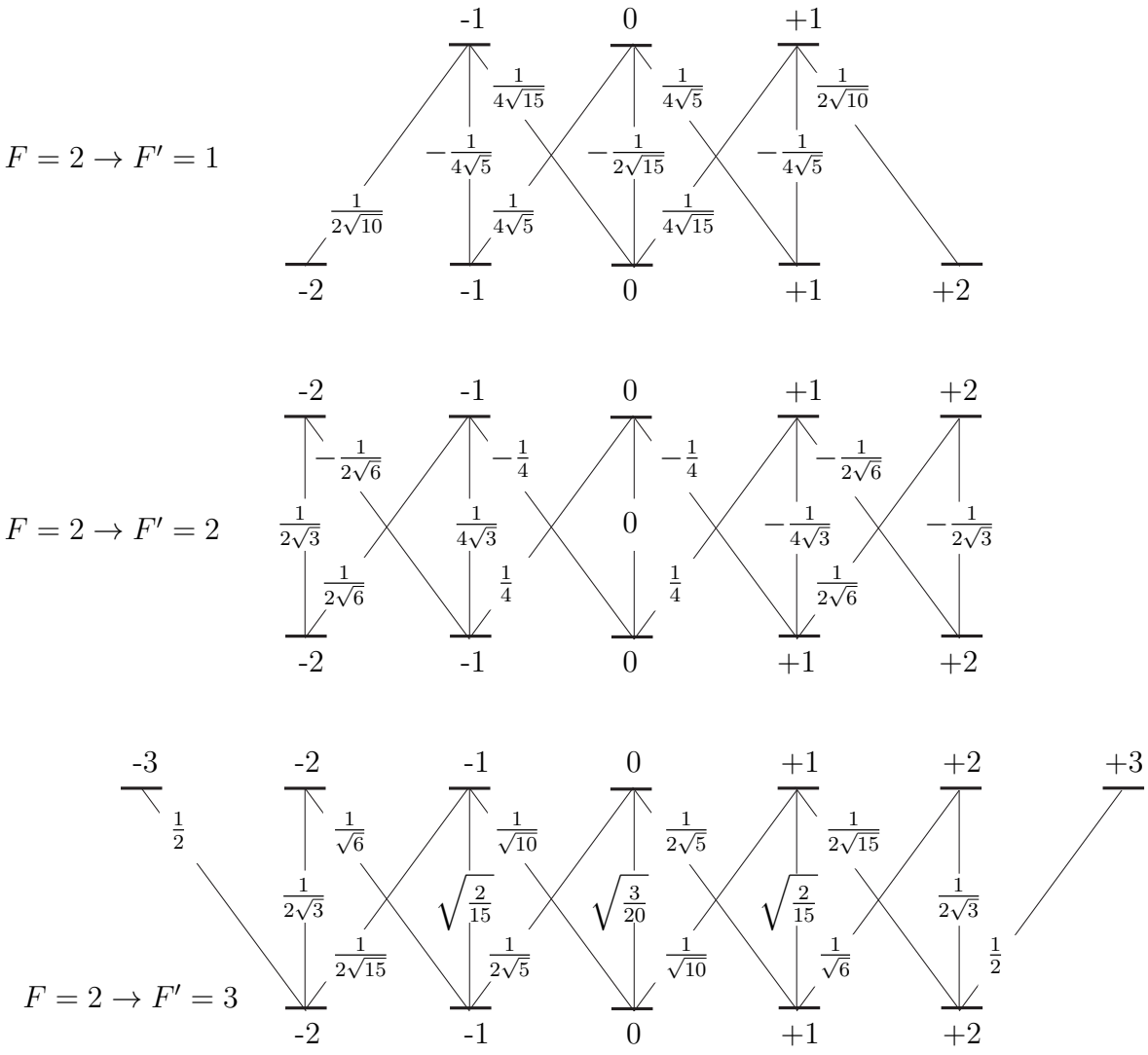

Figure A.3: ^{7}Li D2 transition matrix elements ($F = 2 \to F'$) in units of $\langle J'||\boldsymbol{\mu}(D2)||J\rangle = 2\, ea_o$

^{6}Li, D_1

$F = 1/2 \rightarrow F' = 1/2$

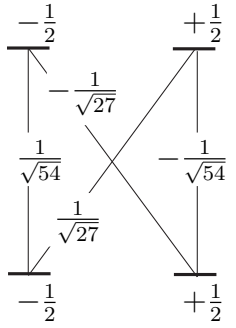

$F = 1/2 \rightarrow F' = 3/2$

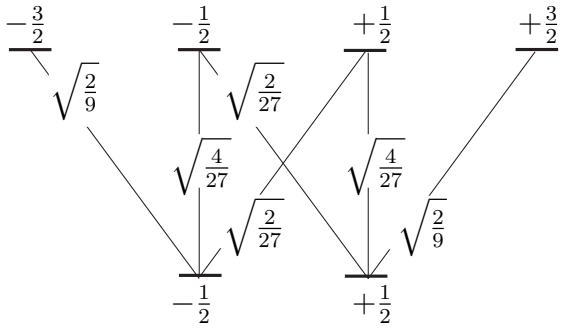

$F = 3/2 \rightarrow F' = 1/2$

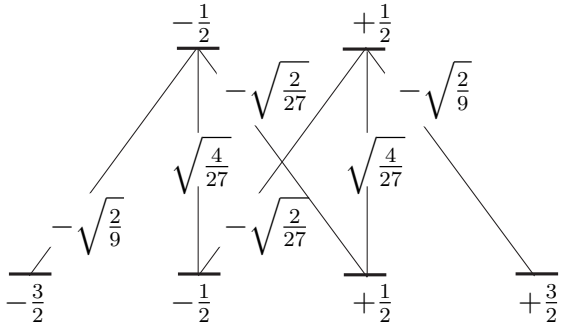

$F = 3/2 \rightarrow F' = 3/2$

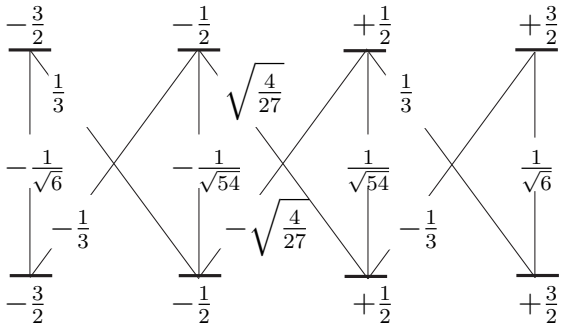

Figure A.4: ^{6}Li D1 transition matrix elements in units of $\langle J' || \boldsymbol{\mu}(D1) || J \rangle = -\sqrt{2}\, e a_\mathrm{o}$

^{6}Li, D_2

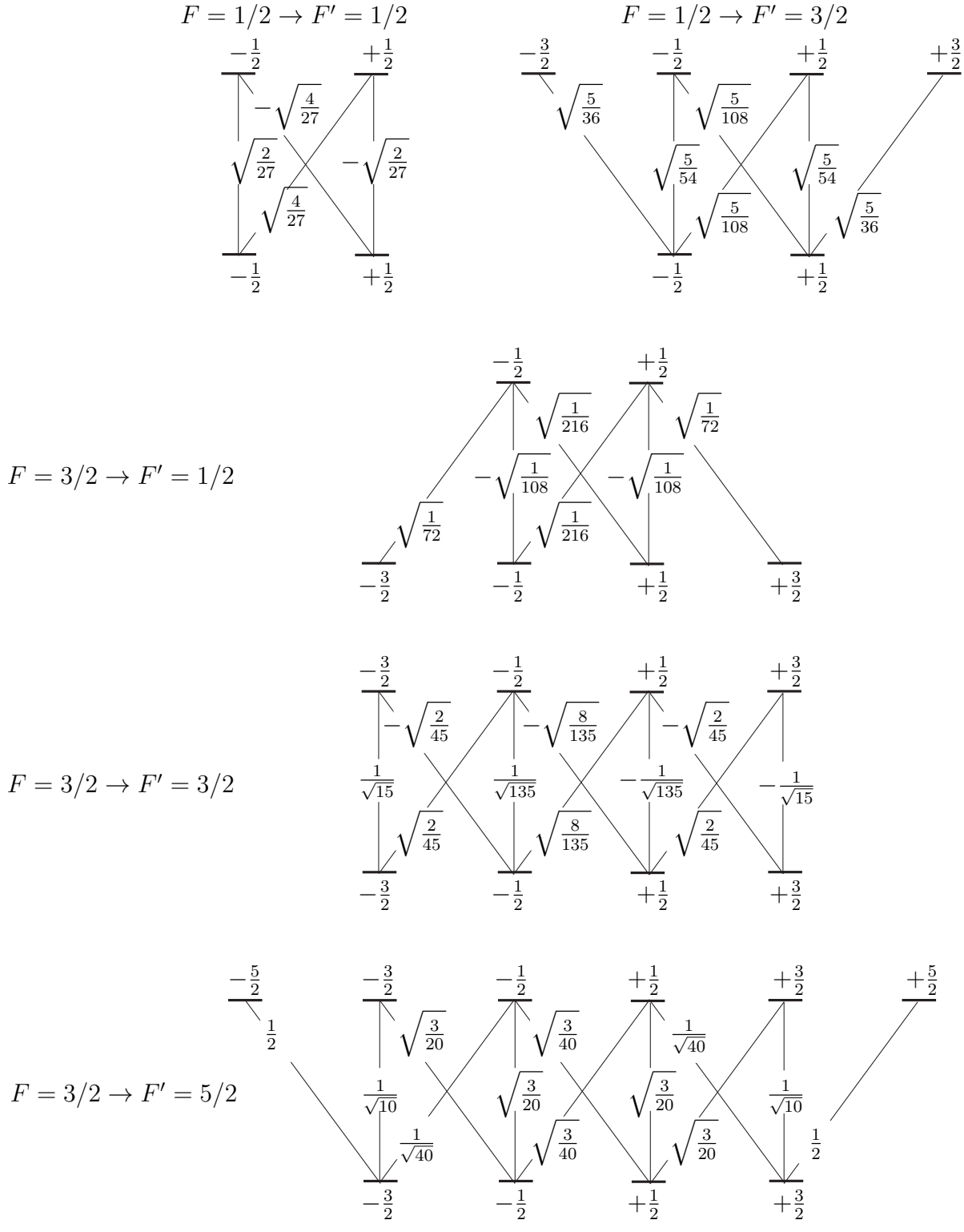

Figure A.5: ^{6}Li D2 transition matrix elements in units of $\langle J' || \boldsymbol{\mu}(D2) || J \rangle = 2\, e a_\mathrm{o}$

Bibliography

[1] C. J. Foot, *Atomic Physics*, Oxford University Press

[2] William D. Phillips and Harold Metcalf *Laser Deceleration of an Atomic Beam* Phys. Rev. Lett **48**, 596 (1982).

[3] G. B. Partridge, *Pairing of Fermionic* ^{6}*Li Throughout the BEC-BCS crossover* Ph.D. thesis, Rice university (2007).

[4] J. Steinmann *Multiphoton Ionization of Laser Cooled Lithium* Ph.D. thesis, University of Heidelberg (2007).

[5] T. A. Delchar, *Vacuum Physics and Techniques*, Chapman & Hall.

[6] D. Griffith, *Introduction to Electrodynamics*, Prentice Hall.

[7] S. D. Saliba and R. E. Scholten, Appl. Opt. **48** 6961 (2009).

[8] H. Nasim and Y. Jamil, Laser Phys. Lett. **10** 043001 (2013).

[9] C. E. Wieman and L. Hollberg, Rev. Sci. Instrum. **62** 1 (1991).

[10] R. K. Raj, D. Bloch, J. J. Snyder, G. Camy, and M. Ducloy, Phys. Rev. Lett **44**, 1251 (1980).

[11] J. Hall, L. Hollberg, T. Baer, and H.G. Robinson, Appl. Phys. Lett **39**, 680 (1981).

[12] D. J. McCarron, S. A. King and S. L. Cornish, Meas. Sci. Technol. **19**, 105601 (2008).

[13] T. G. Tiecke, S. D. Gensemer, A. Ludwig, and J. T. M. Walraven, Phys. Rev. A **80**, 013409 (2009).

[14] M2K Lasers, Nature Photonics **3**, 24 (2009).

[15] M. A. Joffe, Wolfgang Ketterle, Alex Martin, and D. E. Pritchard J. Opt. Soc. Am. B **10**, 2257 (1993).

[16] Amnon Yariv, *Optical Electronics in Modern Communications* Oxford University Press, 5^th ed. (1997).

[17] S. Chu, L. Hollberg, J. Bjorkholm, A. Cable, and A. Ashkin, Phys. Rev. Lett **55**, 48 (1985).

[18] S. Chu, J. Bjorkholm, A. Ashkin, and A. Cable, Phys. Rev. Lett **57**, 314 (1986).

[19] V. S. Letokhov, V. G. Minogin, and B. D. Pavlik, Sov. Phys. JETP **45**, 698 (1977).

[20] D. Wineland and W. Itano, Phys. Rev. A **20**, 1521 (1979).

[21] P. Lett, R. Watts, C. Westbrook, W. D. Phillips, P. Gould, and H. Metcalf, Phys. Rev. Lett. **61**, 169 (1988).

[22] Dalibard, J., and C. Cohen-Tannoudji, J. Opt. Soc. Am. B **6**, 2023 (1989).

[23] P. J. Ungar, D. S. Weiss, E. Riis, and Steven Chu, J. Opt. Soc. Am. B **6**, 2058 (1989).

[24] A. Kastberg, W. D. Phillips, S.L. Rolston, and R. J. C. Spreeuw Phys. Rev. Lett. **74**, 1542 (1995)

[25] Y. Castin, J. Dalibard, and C. Cohen-Tannoudji, *Light Induced Kinetic Effects on Atoms, Ions, and Molecules*, ETS Editrice, Pisa(1991).

[26] William D. Phillips, Rev. Mod. Phys. **70**, 721 (1998).

[27] C. Salomon. J . Dalibard, W. D. Phillips, A. Clairon and S. Guellati, Europhys. Lett. **12** (8), 683 (1990).

[28] D. Lucasa, P. Horakb, and G. Grynberg, Eur. Phys. J. D. **7** 261 (1999).

[29] Paul Hamilton, Geena Kim, Trinity Joshi, Biswaroop Mukherjee, Daniel Tiarks, and Holger Müller, Phys. Rev. A **89**, 023409 (2014).

[30] R. C. Weast, M. J. Astle, and W. H. Beyer, editors. *CRC Handbook of Chemistry and Physics*, CRC Press, Boca Raton, 64th edition (1983)..

[31] I. Mills, T. Cvitas, K. Homann, N. Kallay, and K. Kuchitsu. *Quantities, Units, and Symbols in Physical Chemsitry*, Blackwell Scientific Publishing, Oxford (1988).

[32] J. Emsley, *The Elements*, Oxford Chemistry Guides Oxford. Univ. Press, New York, (1995).

[33] *NIST Chemistry WebBook*, webhttp://webbook.nist.gov/chemistry/.

[34] L. Windholz, *Laser-spectroscopic investigations of the lithium resonance lines*, Appl. Phys. B **60** 573 (1995).

[35] E. Arimondo, M. Inguscio, and P. Violino, *Experimental determinations of the hyperfine structure in the alkali atoms*, Reviews of Modern Physics **49** (1), 31 (1977).

[36] A. Beckmann, K.D. Boklen, D. Elke, Z. Phys. *270*, 173 (1974).

[37] J. Walls, R. Ashby, J. Clarke, B. Lu, W. van Wijngaarden, *Measurement of isotope shifts, fine and hyperfine structure splittings of the lithium D lines*, Eur. Phys. J. D **22**, 159 (2003).

[38] H. Orth, H. Ackermann, E. Otten, *Fine and Hyperfine Structure of the* 2^2P *Term of* ^7Li*; Determination of the Nuclear Quadrupole Moment*, Z. Phys. A **273**, 221 (1975).

[39] Orth, H. , R. Veit, H. Ackermann, and E. W. Otten, *Abstracts of Contributed PaPews to the fourth Intenzational Conference on Atomic Physics*, edited by J. Kowalski and H. G. Weber (Heidelberg), p. 93. (1974).

[40] Ritter, G. J., Can. J; Phys. **43**, 770 (1965).

[41] L. Windholz, *Laser-spectroscopic investigations of the lithium resonance lines*, Appl. Phys. B **60** 573 (1995).

[42] W. I. McAlexander, E. R. I. Abraham, and R. G. Hulet, *Radiative lifetime of the 2P state of lithium.* Phys. Rev. A, **54**(1):R5 (1996).

[43] Michael E. Gehm *Properties of* ^6Li (2003).

[44] G. Audi, O. Bersillon, J. Blachot and A.H. Wapstra, *The NUBASE evaluation of nuclear and decay properties* Nuclear Physics A **729** 3-128 (2003).

[45] A. R. Edmonds *Angular Momentum in Quantum Mechanics*, Princeton University Press.

[46] G. Amelino-Camelia, C. Lämmerzahl, A. Macias, and H. Müller arXiv:gr-qc/0501053.

[47] Ertan Göklü and Claus Lämmerzahl, Class. Quantum Grav. **25**, 105012 (2008).

[48] T. Damour, F. Piazza, and G. Veneziano, Phys. Rev. Lett., **89**, 081601 (2002).

[49] Ertan Göklü, Claus Lämmerzahl, Gen. Rel. Grav. **43**, 2065-2088 (2011).

[50] C. Wetterich, Phys. Lett. B, **561**, 10 (2003).

[51] H. B. Sandvik, J. D. Barrow and J Magueijo, Phys. Rev. Lett., **88**, 031302 (2002).

[52] Gia Dvali and Matias Zaldarriaga, Phys. Rev. Lett., **88**, 091303 (2002).

[53] P. G. Roll, R. Krotkov, and R. H. Dicke Annals of Physics, **26**, 442 (1964).

[54] V. B. Braginsky and V. I. Panov, Sov. Phys. JEPT, **34**, 463 (1972).

[55] S. Schlamminger, K.-Y. Choi, T. A. Wagner, J. H. Gundlach, and E. G. Adelberger Phys. Rev. Lett., **100**, 041101 (2008).

[56] J. G. Williams, S. G. Turyshev, and D. H. Boggs, Phys. Rev. Lett., **93**, 261101 (2004).

[57] J. Hartwig, D. Schlippert, U. Velte, D. Tiarks, N. Winter, M. Zaiser, V. Lebedev, W. Ertmer, E. M. Rasel, 2011 CLEO conference proceedings, doi:10.1109/CLEOE.2011.5942931.

[58] http://www.iqo.uni-hannover.de/atlas.html.

[59] Jason M. Hogan, David M. S. Johnson, Mark A. Kasevich, arXiv:0806.3261.

[60] R. Geiger, V. Menoret, G. Stern, N. Zahzam, P. Cheinet, B. Battelier, A. Villing, F. Moron, M. Lours,Y. Bidel, A. Bresson, A. Landragin, and P. Bouyer, Nat. Comm., **2**, 474 (2011).

[61] J. Rudolph et al., Microgravity Sci. Technol. **23**, 287-292 (2011) doi:10.1007/s12217-010-9247-0.

[62] http://www.exphy.uni-duesseldorf.de/Publikationen/2010/STE-QUEST_final.pdf.

[63] http://www.cnes.fr/web/CNES-en/2847-microscope.php.

[64] Pierre Touboula, Manuel Rodriguesa,Gilles Metrisb,and Bernard Tatry MICROSCOPE, testing the equivalence principle in space (2001), doi:10.1016/S1296-2147(01)01264-1.

[65] http://einstein.stanford.edu/STEP/.

[66] N. Lockerbie, J.C. Mester, R. Torii, S. Vitale, and P.W. Worden., STEP: A status report., doi:10.1007/3-540-40988-2_11.

[67] A.M. Nobili et al., Galileo Galilei (GG): space test of the weak Equivalence Principle to $10^{-}17$ and laboratory demonstrations, Classical and Quantum Gravity (2012), http://eotvos.dm.unipi.it/documents/generalpapers/GGforCQGfocusIssueWEP.pdf.

[68] I. Estermann and Otto Stern, Zeits. F. Physik, **61**, 95 (1930).

[69] A. D. Cronin, J. Schmiedmayer, D. E. Pritchard, Rev. Mod. Phys. **81**, 1051 (2009).

[70] O. Carnal, and J. Mlynek, Phys. Rev. Lett., **66**, 2689 (1991).

[71] D. W. Keith, C. R. Ekstrom, Q. A. Turchette, and D. E. Pritchard, Phys. Rev. Lett., **66**, 2693 (1991).

[72] F. Riehle, Th. Kisters, A. Witte, J. Helmke, and Ch, J. Borde, Phys. Rev. Lett., **67**, 177 (1991).

[73] M. Kasevich, and S. Chu, Appl. Phys. B, **54** 321 (1992).

[74] A. Peters, K. Y. Chung, and S. Chu, Nature **400**, 849 (1999).

[75] S. Fray, and M. Weitz, Space Sci. Rev. **148**, 225 (2009).

[76] A. Bonnin, N. Zahzam, Y. Bidel, and A. Bresson, Phys. Rev. A, **88**, 043615 (2013).

[77] Holger Mueller, Sheng-wey Chiow, Quan Long, Sven Herrmann, and Steven Chu, Phys. Rev. Lett. **100**, 180405 (2008).

[78] Holger Mueller, Sheng-wey Chiow, Sven Herrmann, and Steven Chu, Phys. Rev. Lett. **102**, 240403 (2009).

[79] Sheng-wey Chiow, Tim Kovachy, Hui-Chun Chien, and Mark A. Kasevich, Phys. Rev. Lett. **107**, 130403 (2011).

[80] Susannah M. Dickerson, Jason M. Hogan, Alex Sugarbaker, David M. S. Johnson, and Mark A. Kasevich Phys. Rev. Lett. **111**, 083001 (2013).

[81] L. Zhou, Z. Y. Xiong, W. Yang, B. Tang, W. C. Peng, K. Hao, R. B. Li, M. Liu, J. Wang, M. S. Zhan, Gen. Relativ. Gravit. **43**, 1931 (2011).

[82] Tim Kovachy, Jason M. Hogan, David M. S. Johnson, and Mark A. Kasevich, Phys. Rev. A **82**, 013638 (2010).

[83] Clauser J. F., Physica B, **151**, 262-272 (1988).

[84] Justin Brown, Brian Estey, and Holger Mueller, *A Cavity-based Atom Iterferometer Inertial Sensor*, http://techtransfer.universityofcalifornia.edu/NCD/22388.html.

[85] Pippa Storey and Claude Cohen-Tannoudji, J. Phys. II France **4**, 1999-2027 (1994).

[86] F. Riehle, Th. Kisters, A. Witte, and J. Helmcke Phys. Rev. Lett. **67**, 177 (1991).

[87] D. S. Weiss, B. C. Young, and S. Chu, Appl. Phys. B **59**, 217-256 (1994).

[88] Holger Müller, Sheng-wey Chiow, and Steven Chu, Phys. Rev. A **77**, 023609 (2008).

[89] M. Hohensee and H. Müller, J. Mod. Opt. **58**, 2021 (2011).

[90] M. Hohensee, H. Müller, and R. B. Wiringa Phys. Rev. Lett. **111**, 151102 (2013).

[91] F. Lison, P. Schuh, D. Haubrich, and D. Meschede, Phys. Rev. A **61**, 013405 (1999).

[92] C. Slow, L. Vernac, L.V. Hau, Rev. Sci. Instrum. **76**, 103101 (2005).

[93] K. M. R. van der Stam, E. D. van Ooijen, R. Meppelink, J. M. Vogels, and P. van der Straten. Rev. Sci. Instrum. **78**, 013102, (2007).

[94] C.A. Stan and W. Ketterle, Rev. Sci. Instr., **76**, 63113 (2005).

[95] A. G. Truscott, K. E. Strecker, W. I. McAlexander, G. B. Partridge, and R. G. Hulet Science **271**, 2570 (2001).